Nanoporous Alumina based Hypersonic Phononic Hybrid Structures Studied by Brillouin Spectroscopy

Dissertation zur Erlangung des Grades
’Doktor der Naturwissenschaften’
(Dr. rer. nat.)
im Promotionsfach Physik

am Fachbereich Physik, Mathematik und Informatik
der Johannes Gutenberg–Universität Mainz

vorgelegt von

M.Eng. Akihiro Sato

geboren in Fukushima, Japan

Mainz, 2009

Die vorliegende Arbeit wurde im Zeitraum von Mai 2006 bis August 2009 am Max-Planck-Institut für Polymerforschung in Mainz angefertigt.

Abgabedatum: 24.09.2009
Dekan:
Erster Berichterstatter:
Zweiter Berichterstatter:
Tag der mündlichen Prüfung: 6.11.2009

Zusammenfassung

Phononische Kristalle sind strukturierte Materialien mit sich periodisch ändernden elastischen Moduln auf der Wellenlängenskala. Die Interaktion zwischen Schallwellen und periodischer Struktur erzeugt interessante Interferenzphänomene, und phononische Kristalle erschließen neue Funktionalitäten, die in unstrukturierter Materie unzugänglich sind. Hypersonische phononische Kristalle im Speziellen, die bei GHz Frequenzen arbeiten, haben Periodizitäten in der Größenordnung der Wellenlänge sichtbaren Lichts und zeigen daher die Wege auf, gleichzeitig Licht- und Schallausbreitung und -lokalisation zu kontrollieren, und dadurch die Realisierung neuartiger akusto-optischer Anordnungen. Bisher bekannte hypersonische phononische Kristalle basieren auf thermoplastischen Polymeren oder Epoxiden und haben nur eingeschränkte thermische und mechanische Stabilität und mechanischen Kontrast. Phononische Kristalle, die aus mit Flüssigkeit gefüllten zylindrischen Kanälen in harter Matrix bestehen, zeigen einen sehr hohen elastischen Kontrast und sind bislang noch unerforscht. In dieser Dissertation wird die experimentelle Untersuchung zweidimensionaler hypersonischer phononischer Kristalle mit hexagonaler Anordnung zylindrischer Nanoporen basierend auf der Selbstorganisation anodischen Aluminiumoxids (AAO) beschrieben. Dazu wird die Technik der hochauflösenden inelastischen Brillouin Lichtstreuung (BLS) verwendet. AAO ist ein vielsetiges Modellsystem für die Untersuchung reicher phononischer Phänomene im GHz-Bereich, die eng mit den sich in den Nanoporen befindlichen Flüssigkeiten und deren Interaktion mit der Porenwand verknüpft sind. Gerichteter Fluss elastischer Energie parallel und orthogonal zu der Kanalachse, Lokalisierung von Phononen und Beeinflussung der phononischen Bandstruktur bei gleichzeitig präziser Kontrolle des Volumenbruchs der Kanäle (Porosität) werden erörtert. Außerdem ermöglicht die thermische Stabilität von AAO ein temperaturabhängiges Schalten phononischer Eigenschaften infolge temperaturinduzierter Phasenübergänge in den Nanoporen. In monokristallinen zweidimensionalen phononischen AAO Kristallen unterscheiden sich die Dispersionsrelationen empfindlich entlang zweier hoch symmetrischer Richtungen in der Brillouinzone, abhängig davon, ob die Poren leer oder gefüllt sind. Alle experimentellen Dispersionsrelationen werden unter Zuhilfenahme theoretische Ergebnisse durch finite Elemente Analyse (FDTD) gedeutet. Die Zuordnung der Verschiebungsfelder der elastischen Wellen erklärt die Natur aller phononischen Moden.

Abstract

Phononic crystals are structured materials, which have periodic elastic modulus distributions at wavelength scale, and develop new functions that are never observed in free space since the interaction between sound waves and periodic structures creates interesting interference phenomena. In particular, since hypersonic phononic crystals that operate at gigahertz (GHz) frequencies are composite materials with a period comparable to the wavelength of light, they possess potential for various simultaneous control of light and sound by localizing or propagating them, and applications to novel acousto-optical devices utilizing the enhancement of acousto-optical interactions can be envisioned. Previously-reported hypersonic phononic crystals, which are based on thermoplastic polymers or epoxy, have limited thermal and mechanical instability and elastic contrast. Moreover, despite high elastic contrast, hypersonic phononic crystals based on periodic arrays of cylindrical channels filled with liquids in a rigid matrix have remained essentially unexplored. In this thesis, using high-resolution Brillouin light scattering (BLS), two-dimensional (2D) hypersonic phononic crystals based on self-ordered anodic aluminium oxide (AAO) containing hexagonal arrays of cylindrical nanopores with submicron periodicity are investigated in order to understand the behaviors of elastic wave propagation in these crystals. AAO is a versatile model system for exploration of rich phonon phenomena at GHz frequencies, which are intimately linked to fluids located in the nanopores and their interactions with the pore walls. Consequently, directional flow of elastic energy parallel and perpendicular to the pore axes, phonon localization and tunability of the phononic band structure are realized through the variation of the porosity and change of the physical state of the material residing in the nanopores. In addition, the thermal stability of AAO allows the switching of the hypersonic properties by means of temperature induced phase transitions in the AAO nanopores. For monodomain 2D AAO phononic crystals, the disparity of the dispersion relations along two high symmetry directions in the Brillouin zone sensitively depends whether the nanopores are empty or filled. The nature of the main wave propagation modes in the experimental phononic band diagram is identified via finite differential time domain (FDTD) calculations complemented by the map of the corresponding displacement field.

Contents

1. Introduction 1
- 1.1. Overview . . . 1
- 1.2. Research on phononic crystals to date . . . 3
  - 1.2.1. Sonic crystals . . . 3
  - 1.2.2. Ultrasonic crystals . . . 5
  - 1.2.3. Hypersonic crystals . . . 6
- 1.3. Aim of the study . . . 7

2. Methodology 11
- 2.1. Elastic wave propagation in periodic media . . . 11
- 2.2. Brillouin light scattering . . . 15
  - 2.2.1. The photoelastic effects . . . 15
  - 2.2.2. Interaction with hypersound . . . 18
  - 2.2.3. Optical interferometric techniques . . . 20
    - 2.2.3.1. Single-pass Fabry-Perot interferometer . . . 20
    - 2.2.3.2. Tandem Fabry-Perot interferometer . . . 22
- 2.3. Experimental setup . . . 24
  - 2.3.1. Brillouin light scattering apparatus . . . 24
  - 2.3.2. Scattering geometry . . . 26

3. Anodic aluminium oxide 29
- 3.1. Introduction . . . 29
- 3.2. Pore formation mechanism . . . 30
- 3.3. Self-ordered anodic aluminum oxide . . . 33
  - 3.3.1. anodization setup . . . 33
  - 3.3.2. Two-step anodization . . . 33
  - 3.3.3. Pre-molding anodization . . . 37

4. Anisotropic propagation and confinement of high frequency phonons 41
- 4.1. Introduction . . . 41
- 4.2. Experimental . . . 42
  - 4.2.1. Materials . . . 42

4.2.2. Brillouin spectroscopy 42
4.3. Hypersonic modes in air/AAO phononic crystals 44
4.4. Hypersonic modes in PDMS/AAO phononic crystals 47
4.5. FDTD modeling 50
4.6. Summary 55

5. Tuning and switching hypersonic phononic properties of impedance-contrast nanocomposites 57
5.1. Introduction 57
5.2. Sample preparation 60
5.3. PDMS/AAO as a model system with high elastic contrast 61
5.4. PEG/AAO as a model system with low elastic contrast 62
5.5. Tailoring the degree of dissipation of elastic energy by the soft component . . 64
5.6. Reversible switching of phononic properties by crystallization and melting . . 66
5.7. Summary 74

6. Hypersonic Phononic Crystals based on Highly Ordered anodic Aluminium oxide 77
6.1. Introduction 77
6.2. Experimental 78
6.3. Direct observation of complete phononic dispersion relations 80
6.4. Formation of complete hypersonic phononic bandgap 84
6.5. Summary 86

7. Thesis Conclusion 87

8. Future research 89

A. Appendix 95
A.1. Scattering vector calculation 95
A.1.1. in-plane 95
A.1.2. out-of-plane 96
A.2. Relation between the dispersion relations and lattice constants 97
A.3. Dispersion relations of sapphire 99
A.4. Theoretical band diagram 100
A.5. Structural studies on macroscopic ensembles of tetracosane 101
A.6. Phonon dispersion relations of highly ordered AAO 103

References 105

Acknowledgments 117

List of Figures

1.1. A variety of one- (1D), two- (2D) or three-dimensional (3D) photonic or phononic crystals. While the defining characteristic of a photonic crystal is the periodicity of dielectric medium, one of a phononic crystal is the periodicity of elastic medium. 2

1.2. The kinematic sculpture by Eusebio Sempere, which consists of a periodic cubic array of hollow stainless-steel cylinders with a diameter of 2.9 cm and a unit cell of 10 cm. (Adapted from Ref.[9]) 4

2.1. Two-dimensional cross section of a hexagonal array of pores with a lattice constant of *a* and diameter *d*. 13

2.2. Schematic of light scattering geometry. Polarized light is incident on a sample and scattered in all directions. The scattering vector $\mathbf{q} = \mathbf{k}_i$ - $\mathbf{k}_i$ is defined by the detector position. 15

2.3. Acoustic Bragg reflection. 18

2.4. The optical transmission function of a single-pass Fabry-Perot mirror. 21

2.5. Tandem interferometer with mechanical coupling of the movable plate. 22

2.6. The optical path inside a tandem Fabry-Perot interferometer invented by JRS Scientific Instruments. (Adopted from Ref. [60]) 23

2.7. Schematic of the Brillouin light scattering experiment setup. 25

2.8. The sample holder allowing for BLS measurements under varying degrees of temperature. 25

2.9. Schematics of scattering geometry: (a) transmission geometry and (b) reflection geometry. 26

3.1. Schematic of (a) idealized structure of anodic aluminium oxide and (b) a cross sectional view of the anodized layer. (Adapted from Ref. [131]) 30

3.2. Schematic of (a) time dependence of current density during the anodization process and (b) stages of anodized aluminium oxide layer development. (Adapted from Ref. [131]) 31

3.3. Schematic representations of the top views of porous alumina cell-wall structures prepared in (a) sulfuric, (b) oxalic and (c) phosphoric acid. (Adapted from Ref. [32]) (d)-(f) Corresponding scanning electron microscope (SEM) images. 32

3.4. Schematic of (a) the anodization setup and (b) top view of the anodization cell. There are four circular holes at the bottom of the cell to anodize four aluminum disks simultaneously. 34

3.5. Schematic of the nanopores formation. (a) Electropolishing, (b) first anodization, (c) removal of the formed oxide layer, (d) second anodization, (e) removal of aluminum layer, (f) removal of barrier layer. 35

3.6. Scanning electron microscope (SEM) images of nanoporous anodic aluminum oxide prepared in 0.3 M sulfuric acid at 25 V. (a) the top view and (b) the bottom view of the membrane after removing Al selectively, which are described as (i) and (ii) in Fig. 3.5, respectively. (c) the top view of the membrane after the second anodization. (d) Cross sectional image of the AAO scaffold. . . . 36

3.7. Current-time curves of anodizing at 40 V in 0.3 M oxalic acid at 3 °C. Inset shows a zoomed area of minimum region. 37

3.8. Schematic of the nanopores formation. (a) Electropolishing, (b) first anodization, (c) removal of the formed oxide layer, (d) second anodization, (e) removal of aluminum layer, (f) removal of barrier layer. 38

3.9. Scanning electron microscope (SEM) image of nanoporous anodic aluminum oxide prepared in 0.3 M oxalic acid at 80 V. 39

4.1. Scanning electron microscope (SEM) images of native AAO. (a), (b), (c), Top views. (a) porosity p = 11%, (b) p = 32%, (c) p = 65% for lattice constant a = 100 nm. (d) Cross sectional image of the AAO scaffold seen in (b). 43

4.2. Schematics of scattering geometry: (a) transmission geometry and (b) reflection geometry. 44

4.3. (a) A series of polarized BLS spectra for AAO with a lattice constant of 100 nm and a diameter of 60 nm for the "*in-plane*" ($\mathbf{q}_\perp$) phonon propagation. (b) Both polarized and depolarized spectra at $q_\perp = 0.0118\ \mathrm{nm}^{-1}$. 45

4.4. Dispersion relations of both (a) "*in-plane*" ($\mathbf{q}_\perp$) and (b) "*out-of-plane*" ($\mathbf{q}_\parallel$) longitudinal phononic modes in air-filled AAO. The black, red and blue solid lines in (a) represent the dispersion relations for air-filled AAO with p = 11%, p = 32% and p = 65%, while the corresponding dashed lines represent the effective sound velocities in corresponding AAO scaffolds. 46

4.5. (a) BLS spectra of AAO (p = 65%) infiltrated with PDMS at four different in-plane $\mathbf{q}_\perp$ values. (b) BLS spectra of AAO infiltrated with PDMS (p = 11%, 32% and 65%) measured at a similar out-of-plane $\mathbf{q}_\parallel$ value. The BLS spectra are well reproduced by one or two Lorentzian shapes indicated by the solid lines in (a) and (b). 47

4.6. "*In-plane*" ($\mathbf{q}_\perp$) and "*out-of-plane*" ($\mathbf{q}_{||}$) longitudinal phononic branches (***1-3***, ***5***) in PDMS-filled AAO. The black and red dashed lines represent the dispersion relations for air-filled AAO in both "*in-plane*" and "*out-of-plane*" (data points in the light grey area) direction with 32%, while the corresponding solid lines represent the effective sound velocities in corresponding PDMS-filled AAO scaffolds. 48

4.7. Dispersion relations of both (a) "*in-plane*" ($\mathbf{q}_\perp$) and (b) "*out-of-plane*" ($\mathbf{q}_{||}$) longitudinal phononic modes (***1-3***,***5***) in AAO containing PDMS. The black, red and blue solid lines in e represent the dispersion relations for native AAO with p = 11%, p = 32% and p = 65%, while the corresponding dashed lines represent the effective sound velocities in corresponding AAO scaffolds containing PDMS. The branch (***5***) is shown only for AAO with p = 32%. 49

4.8. Effective sound velocity c in AAO as a function of porosity .The experimental and computed longitudinal sound velocity for empty (open squares) and filled with PDMS holes (open circles) is indicated in black and red symbols respectively. The experimental shear sound velocity in empty (blue triangles) and filled (inverse triangles) is compared to the theoretical values indicated by red triangles. All lines are to guide the eye. 51

4.9. Theoretical band structures of "*in-plane*" (a) and "*out-of-plane*" (b) phononic dispersion curves in AAO (a = 100 nm; d = 60 nm; p = 32%) either with air-filled nanopores (black solid symbols) or containing fluid PDMS (red open symbols). 51

4.10. Map of the distributions of the displacement U of the eigenmodes inside an AAO unit cell belonging to modes **A′**, **A** and **B** located on the branch (***1***) shown in Fig. 4.9(a). 52

4.11. Map of the distributions of the displacement U of the eigenmodes inside an AAO unit cell belonging to modes **A″** and **C** located on branches (***3***) and (***5***) shown in Fig. 4.9(b). 53

4.12. Theoretical band structures of "*in-plane*" (a) and "*out-of-plane*" (b) phononic dispersion curves in AAO (a = 100 nm; d = 60 nm; p = 32%) either with air-filled nanopores (black solid symbols) or containing fluid PDMS (red open symbols). A new branch appears in the calculations only in the presence of a thin (5 nm) rigid PDMS interphase in the nanopores schematically shown in (c). 54

5.1. Scanning electron microscopy (SEM) images of AAO. (a) top view and (b) cross sectional image. 60

5.2. "*In-plane*" ($q_\perp$) and "*out-of-plane*" ($q_{||}$) longitudinal phononic branches (***1-3***, ***5***) in PDMS-filled AAO scaffolds (d = 60 nm; a = 100 nm). The black and red solid lines represent the effective sound velocities along the "*in-plane*" (data points in the unshaded area) and "*out-of-plane*" (data points in the light grey area) directions. 61

5.3. "*In-plane*" BLS spectrum of (a) PEG- and (b) PDMS-filled AAO (d = 60 nm; a = 100 nm) at $\mathbf{q}_{\perp} = 0.0167$ nm^{-1}. The red solid line shows the representation of the spectra by a sum of up to three lorentzian lines. (c) The dispersion relations for the two longitudinal acoustic (***1***) and the flat (***2***) branches. The black solid line represents the effective sound velocities for "*in-plane*" propagation in the PEG-filled AAO nanohybrids. 63

5.4. Full width at half maximum (Γ) of BLS spectra plotted as a function of q^2 for branch (***1***). The solid lines are best fits to the data. 65

5.5. DSC scans of (a) PVDF nanostructures in AAO and (b) bulk PVDF. Dotted curves are heating runs, while solid curves are cooling runs. Heating and cooling rates are 10 K/min. 67

5.6. Schematic of the WAXS setup. The AAO was mounted in such a way that the long axse of pores were oriented parpendicular to the plane defined by incident beam and detector. 67

5.7. XRD analysis of PVDF inside AAO. PDVF-filled AAO prepared (a) without a thick PDVF film on the surface of AAO and (b) with a thick PDVF film on the surface of AAO. 68

5.8. BLS spectra of PVDF-filled AAO (d = 60 nm; a = 100 nm) measured at 293 K (PVDF is crystalline) and at 493 K (PVDF is liquid) (a) for $q_{\perp} = 0.0167$ nm^{-1} perpendicular to the nanopores and (b) for $q_{||} = 0.0368$ nm^{-1} parallel to the nanopores. 69

5.9. Dispersion relations for "*in-plane*" ($q_{\perp}$) and "*out-of-plane*" ($q_{||}$) longitudinal acoustic modes in crystalline PVDF-filled AAO at 293 K and liquid PVDF-filled AAO at 453 K. 69

5.10. DSC scans of (a) bulk $C_{24}H_{50}$ and (b) $C_{24}H_{50}$ nanostructures in AAO. Dotted curves are heating runs, while solid curves are cooling runs. Heating and cooling rates are 10 K/min. 70

5.11. BLS spectra of $C_{24}H_{50}$-filled AAO (d = 60 nm; a = 100 nm) measured at 20 °C ($C_{24}H_{50}$ is crystalline) and at 90 °C ($C_{24}H_{50}$ is liquid) (a) for $q_{\perp} = 0.0118$ nm^{-1} perpendicular to the nanopores and (b) for $q_{||} = 0.0368$ nm^{-1} parallel to the nanopores. 71

5.12. Dispersion relations for "*in-plane*" ($q_{\perp}$) and "*out-of-plane*" ($q_{||}$) longitudinal acoustic modes in crystalline $C_{24}H_{50}$-filled AAO at 20 °C and liquid $C_{24}H_{50}$-filled AAO at 90 °C. 72

5.13. Theoretical band structure of both "*in-plane*" (a) and "*out-of-plane*" (b) phononic modes for AAO with 30% porosity containing liquid $C_{24}H_{50}$ (red points) or a solid tetracosane (blue points). 73

6.1. Scanning electron microscope (SEM) images of native AAO. (a), (b), Top views. (a) porosity p = 23%, (b) p = 50% for lattice constant a = 200 nm. The scale bar in both images is 500 nm. 79

6.2. Schematics of scattering geometry: (a) transmission geometry and (b) reflection geometry. 79

6.3. BLS spectrum of (a) sapphire recorded at $q_\perp$ = 0.0118 nm^{-1}, (b) AAO with a lattice constant of 200 nm and a diameter of 100 nm at $q_\perp$ = 0.0181 nm^{-1} and solid PEO-filled AAO at $q_\perp$ = 0.0167 nm^{-1} in ΓX direction, and (c) AAO with a lattice constant of 200 nm and a diameter of 150 nm at $q_\perp$ = 0.0193 nm^{-1} and solid PEO-filled AAO at $q_\perp$ = 0.0167 nm^{-1} in ΓJ direction (c). Here only anti-stokes sides are represented. 80

6.4. Phonon dispersion relations. Superposed experimental and theoretical phonon dispersion relations along ΓX and ΓJ directions, respectively, for air-filled AAO with (a) 23% and (b) 50% porosity, liquid-filled AAO with (c) 23% and (b) 50% porosity and solid PEO-filled AAO with (e) 23% and (f) 50% porosity. Black dots represent theoretical dispersion relations in all cases, while open black squares, red circles and blue triangles represent experimental dispersion relations. 82

6.5. (a) Theoretical band structures of in-plane phonon dispersion curves in AAO (a = 100 nm; d = 60 nm). (b), (c) Map of the distributions of the displacement U of the eigenmodes inside an AAO unit cell belonging to mode **E** located on the second propagation band in (a). 83

6.6. BLS spectra recorded at $q_\perp$ = 0.0181 nm^{-1} and $q_\perp$ = 0.021 nm^{-1} along ΓX and ΓJ directions correspond to the edge of the first Brillouin zone. 85

6.7. Dispersion relations of PDMS-filled AAO with a lattice constant of 200 nm and pore diameter of 100 nm along both ΓX and ΓJ directions. 85

8.1. (a) BLS spectra of AAO infiltrated with PI at five different “*in-plane*” $q_\perp$ values for both PI-0 (black) and PI-14 (red). Black and red dashed lines represent the corresponding frequency of the flat mode ***2***. (b) BLS spectra of AAO infiltrated with PI at the same “*out-of-plane*” $q_\parallel$ value for both PI-0 (black) and PI-14 (red). 90

8.2. Phonon dispersion relations of (a) “*in-plane*” ($q_\perp$) and (b) “*out-of-plane*” ($q_\parallel$) phonon propagation. Black and red symbols represent dispersion relations for PI-0 and PI-14, respectively. 90

8.3. (a) Polarized and depolarized Brillouin spectrum of P[VDF-TrFE] recorded at $q_\perp$ = 0.0167 nm^{-1}. The phonon dispersion relations of (a) the “*in-plane*” and the “*out-of-plane*” phonon propagation in P[VDF-TrFE]-filled AAO. The phonon dispersion relations (b) for the “*in-plane*” and (c) for the “*out-of-plane*” phonon propagation. The black and dark yellow lines represent the dispersion relations for longitudinal mode in air- and P[VDF-TrFE]-filled AAO, while corresponding dashed line represents the dispersion relation for transverse mode in P[VDF-TrFE]-filled AAO. 92

A.1. Schematics of the scattering geometry: (a) transmission geometry and (b) reflection geometry. 95
A.2. Dispersion relations for “*in-plane*” ($\mathbf{q}_\perp$) and “*out-of-plane*” ($\mathbf{q}_\parallel$) longitudinal phononic modes (***1 - 3***) in AAO containing PDMS with a = 65 nm and p = 30% (green symbols) as well as a = 100 nm and p = 11% (black symbols). The solid lines represent the dispersion relations for the corresponding air-filled AAO. . 98
A.3. Polarized (VV) and depolarized (VH) BLS spectrum of sapphire recorded at q = 0.0118 nm^{-1}. 99
A.4. Dispersion relations of both longitudinal and transverse modes in sapphire. The black squires, circles and triangles represent the longitudinal and two transverse dispersion relations, respectively, while the corresponding solid, short dotted and short dashed lines represent effective sound velocities. 100
A.5. Theoretical band structures of both “*in-plane*” (a) and “*out-of-plane*” (b) phononic modes for AAO with porosity 65 %. 101
A.6. XRD analysis of $C_{24}H_{50}$ nanostructure inside AAO. (a) $\Theta/2\Theta$ scan. (b) $\Theta/2\Theta$ scan of bulk $C_{24}H_{50}$. (c) $\Theta/2\Theta$ scan of both bulk $C_{24}H_{50}$ and $C_{24}H_{50}$ nanostructure inside AAO. (d) Ψ scan representing orientation distributions with respect to the AAO surface recorded at 2Θ = 29.7° and 35.9°. 102
A.7. (a) Dispersion relations in air- and PEO-filled anodic porous alumina in both ΓX and ΓJ directions for p = 23% porosity. (b) Dispersion relations in air- and PEO-filled anodic porous alumina in both ΓX and ΓJ directions for p = 50% porosity. 103

List of Tables

3.1. Possible alumina minerals with the different refractive indices and densities. . 33
3.2. Anodization conditions for each acid electrolyte 34
3.3. Anodization conditions for each acid electrolyte 39

4.1. Experimental effective medium velocities in air-filled AAO. 46
4.2. Experimental effective medium velocities in PDMS-filled AAO. 49
4.3. Comparison between the experimental and theoretical effective medium velocities c_{eff} for the "*in-plane*" phonon propagation. 53

5.1. Sound velocities and densities of materials 59
5.2. Comparison of dissipation coefficients 65

6.1. Experimental effective medium velocities c_{eff} for the "*in-plane*" longitudinal phonon propagation along both ΓX and ΓJ. 83

8.1. Effective medium velocities in air- and P[VDF-TrFE]-filled AAO. 92

1. Introduction

1.1. Overview

Scientific technology has been making various impacts and spillover effects on our daily life in the course of its development. The invention of the transistor[1] is often considered as being one of the greatest inventions of the 20th century. Nonlinear solid-state devices such as transistors, diodes and rectifiers that control electrical conduction are key active components in practically all modern electronics. In the late 1980s, a new class of materials, so-called *photonic* crystals, has been introduced.[2, 3] *Photonic* crystals are periodic dielectric media with a large difference in their refractive indices (Fig. 1.1) and have the potential to control the optical properties of materials. The fundamental property of photonic crystals is the formation of photonic bandgaps, through which specific wavelengths of light cannot propagate. This is the optical analogue of bandgaps for electron waves in semiconductors (electronic crystals). Therefore, photonic crystals could develop new functions which are never observed in free space, such as localization and guiding of light, slow light and negative refraction, thus leading to many applications in telecommunications, high-speed computers, large-area coherent laser action and optical imaging.

Since the introduction of photonic crystals, another new class of materials controlling over phonons, sound and other mechanical waves, which are referred to as *phononic* crystals, has drawn a great deal of attention. *Phononic* crystals have periodical elastic modulus distribution, and are the acoustic analogue of *photonic* crystals. Although the physical nature of phononic crystals is different from one of photonic crystals as well as semiconductors, the physical origin of the bandgap formation is essentially the same in these materials. However, from the scientific point of view, physics of phononic crystals grow increasingly complex compared to photonic and electronic crystals. Mechanical waves can have both longitudinal and transverse components, in contrast to electromagnetic waves, which only have the transverse component, and electron waves, which are scalar. Moreover, as for mechanical waves, while both longitudinal and transverse displacement waves can propagate in solids, only longitudinal displacement waves are allowed to propagate in fluids. As a result, the formation of complete phononic bandgaps depends on a number of parameters and is significantly harder than that of actively investigated photonic bandgaps since phononic structures having bandgaps for both longitudinal and transverse waves in the same frequency region must be designed.

The research on phononic crystals with complete bandgaps initiated in 1992 with theoretical work by Sigalas and Economou.[4] They reported that phononic structures consisting of three-dimensional (3D), periodic, identical high-density spheres which are placed in a low-

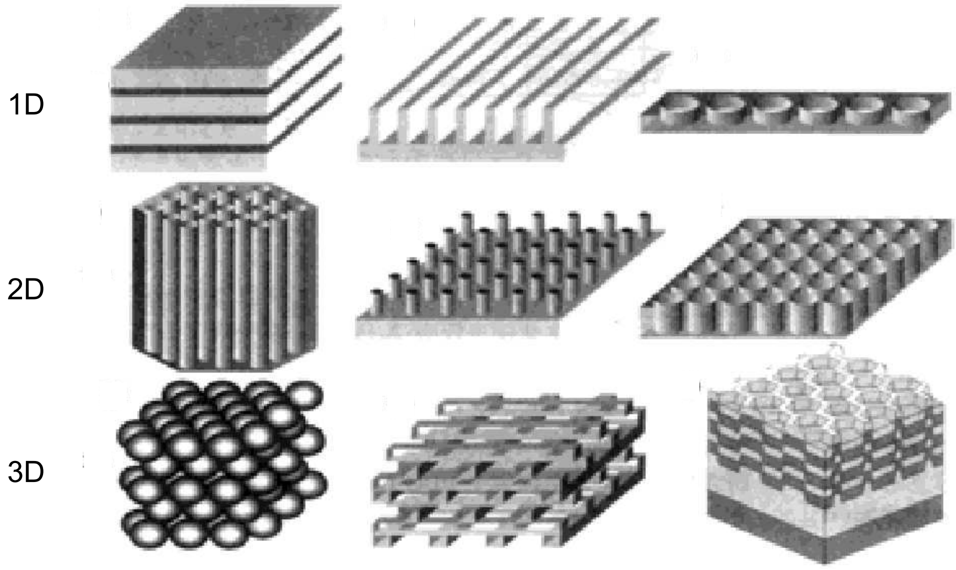

Figure 1.1.: A variety of one- (1D), two- (2D) or three-dimensional (3D) photonic or phononic crystals. While the defining characteristic of a photonic crystal is the periodicity of dielectric medium, one of a phononic crystal is the periodicity of elastic medium.

density host homogeneous material possess complete phononic bandgaps. These phononic structures can be either solid/solid or fluid/fluid. Subsequently, they also reported that an infinite two-dimensional (2D) square array of high-density cylinders embedded periodically in a low-density host material could possess a complete phononic bandgap for both solid/solid and fluid/fluid structures in 2D.[5] Although Sigalas and Economou showed that both 2D and 3D periodic fluid/fluid or solid/solid phononic structures show complete phononic bandgaps, they predicted that complete phononic bandgaps should also exist in solid/fluid phononic structures despite the fact that both longitudinal and transverse elastic waves propagate at two different speeds in solids while acoustic waves propagate at a single speed in fluids. During much of the same period, Kushwaha *et al.* reported the existence of complete phononic bandgaps for transverse displacement of the elastic waves in 2D phononic structures.[6]

In spite of a number of theoretical investigations reported after the two theoretical works described above, an ideal phononic structure has not been found. In the past, a lot of studies have focused on sonic and ultrasonic phononic crystals since they are promising for applications in acoustics, sensing, and medical diagnostic, but also because of experimental convenience. As a result, relatively large phononic bandgaps have been theoretically and experimentally realized. However, a detailed understanding and control of sound wave propagation behavior in hypersonic phononic crystals haven't been done since fabrication of hypersonic phononic crystals and determination of their phonon dispersion are significant experimental challenges.

The importance of investigations on hypersonic phononic properties have long been recognized both from fundamental and practical points of view. Experimental techniques that can characterize these properties are of great value in understanding the elastic wave propagation behavior and designing hypersonic phononic crystals. Until now, there have been only two techniques employed to investigate the phonon dispersion relation of periodic composite media, which are Brillouin light scattering (BLS)[7] and the optical pulse-pump probe technique[8]. We have employed BLS spectroscopy to investigate the phononic properties of hypersonic hybrid nanostructures based on anodic aluminium oxide (AAO). BLS is a powerful and non-destructive technique that allows for the direct measurement of the phonon dispersion relations along any direction in the Brillouin zone, thus leading to a further understanding of detailed features of the propagation bands. It employs scattering of a laser beam by random thermal phonons in the samples. In this thesis, phononic properties of hypersonic phononic hybrid nanostructures consisting of AAO infiltrated with polymers and paraffin have been investigated using BLS. It was found that each of the AAO-based hypersonic phononic hybrids shows very interesting elastic wave propagation behaviors. Furthermore, the phononic dispersion relation in AAO along high symmetry directions of the two-dimensional lattice constituted by the nanopores and the liquids located in the nanopores was simulated by means of the numerical band structure calculations using the finite difference time domain (FDTD) method.

1.2. Research on phononic crystals to date

Researchers who were inspired by exciting developments of photonic bandgap structures leading to a variety of phenomena of both fundamental physics and practical device applications began structural studies on phononic crystals. The theoretical research on phononic crystals of complete bandgaps[5, 6] has been generally considered as the catalyst. Thereafter, recent improvement of analytical method and of the measuring device sensitivity has led to understanding of mechanical wave propagation phenomena.

An important and beneficial properties of phononic crystals in general is the scalability of the frequency characteristics from the low audio frequency to the terahertz (THz) range, i.e. from seismic waves to phonon waves. It is useful to divide phononic crystals into three classes - sonic, ultrasonic and hypersonic phononic crystals - based on their frequency operation. Each of these classes leads to entirely different applications and requires completely different technical approaches. Sonic crystals (1 Hz - 20 kHz) are important for sound manipulation and communications; ultrasonic crystals (20 kHz - 1 GHz) play a role in imaging and non-destructive testing; while hypersonic crystals ($\geq$ 1 GHz) may lead to new applications in acousto-optics, signal processing and thermo-electricity. Each of these classes of phononic crystals is treated in more detail later in this section.

1.2.1. Sonic crystals

The major prospect of sonic crystals is their ability to control sound. This is of great interest for applications such as acoustic filters, noise control and improvements in the design of

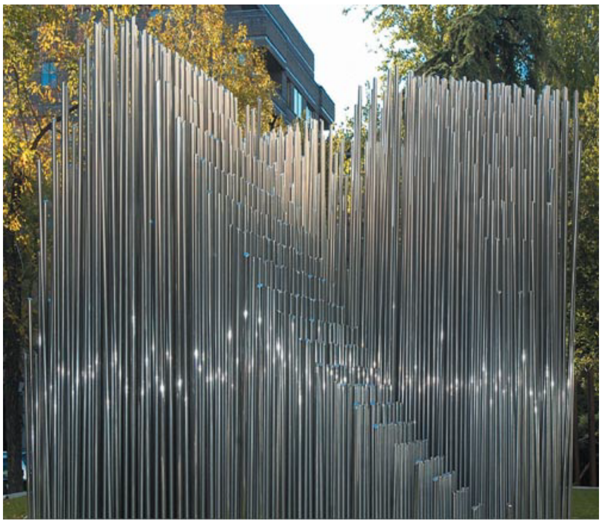

Figure 1.2.: The kinematic sculpture by Eusebio Sempere, which consists of a periodic cubic array of hollow stainless-steel cylinders with a diameter of 2.9 cm and a unit cell of 10 cm. (Adapted from Ref.[9])

transducers. A number of reports have appeared on 2D sonic crystals because they have large lattice constants in the range of millimeter to centimeter and can be fabricated more simply.

A good representation of sonic properties of a periodic structure was provided by Martínez-Sala as shown in Fig. 1.2.[9] The kinematic sculpture contains cubic arrays of aligned hollow stainless-steel cylinders with a diameter of 2.9 cm and a lattice constant of 10 cm. Martínez-Sala *et al*. recognized that the sculpture would have a sonic bandgap, and performed sound attenuation experiments on the sculpture shown in Fig. 1.2. They measured the acoustic transmission of the sculpture as a function of sound frequency. They observed strong sound attenuation at a frequency of 1670 Hz, which could be ascribed to the formation of the first gap when sound travels along the $[100]$ direction in a square lattice.

The first observations of experimental bandgap structures for a sonic crystal were reported by Sánchez-Pérez *et al*.[10], and by Robertson and Rudy[11]. Both works used a 2D periodic array of stainless cylinders in air. In other experiments the formation of bandgaps was reported on 2D periodic arrays of hollow copper cylinders[12], wood cylinders[13] and water-filled elastically-soft polymer tubes[14], respectively, in air. On the other hand, sonic transmission was measured on a 3D sonic crystal composed of a cubic array of rubber coated with lead spheres in an epoxy matrix.[15] Due to effective negative elastic constants caused by localized resonances, such a 3D sonic crystal shows bandgaps with a lattice constant two orders of magnitude smaller than the relevant wavelength.

The accomplishments of the phononic bandgap formation is of great benefit to developing new material function. One of the current hot topics in optics is, for example, the fabrication of superlenses. The negative refraction and superlensing effects in photonic crystals have been experimentally demonstrated recently[16–20]. These studies stimulated research on the negative refraction for acoustic waves in phononic crystals. In practice, the negative refraction and superlensing effects of a surface wave have been experimentally and theoretically demonstrated,[21] while the acoustic negative birefraction has been demonstrated in a 2D sonic crystal composed of a hexagonal array of steel cylinders embedded in air[22]. Furthermore, acoustic negative refraction with backward-wave effects have also been demonstrated both theoretically and experimentally in a 2D sonic crystal consisting of a hexagonal array of air cylinders embedded in aluminium.[23]

Since sonic crystals show many new effects and novel phenomena such as negative birefraction and backward-wave negative refraction, they will open a new path to the design of new acoustic devices. However, a structure needs to be several tens of centimeters wide to create a phononic bandgap in the sonic regime. While this might not be a problem for architectural acoustics including the attenuation of traffic noise along highways, Earthquake and coastal protection, it is impractical for many devices such as headphones and speakers.

1.2.2. Ultrasonic crystals

Since the properties of photonic crystals are scalable, the constituents of ultrasonic crystals and their lattice constants must be reduced to $\approx$ 1 mm - 10 μm with frequencies of $\approx$ 20 kHz - 500 MHz. Although ultrasonic crystals have a variety of potential applications as well as sonic crystals, the technological application mostly lies in their ability to improve device performance and resolution of conventional ultrasonic imaging and diagnostic imaging technique by utilizing acoustic superlensing effects based on negative refraction. The ultrasonic acoustic technology has already been used for medical ultrasonography. However, conventional ultrasonographers have drawbacks including limited penetration depth depending on the frequency and limited ability to focus and reflect, thus causing difficulties in imaging structures. Ultrasonic crystals could be integrated into current imaging systems and overcome the drawbacks mentioned.

The first experimental observation of a complete ultrasonic bandgap in a 2D phononic crystal for the longitudinal mode has been realized[24]. This structure consists of a periodic square array of mercury cylinders in an aluminium alloy plate. Thereafter, Vasseur *et al*. have demonstrated complete ultrasonic bandgaps in a solid/solid 2D crystal consisting of a hexagonal array of circular steel cylinders in epoxy matrix.[25] As is the case for sonic crystals, the formation of phononic bandgaps leads to ultrasound tunneling through 1D[26] and 3D[27] phononic crystal and negative refraction imaging[28–30]. According to Yang *et al*.[28] and Ke *et al*.[29], negative refraction of ultrasound waves was observed at frequencies at the second band of the first complete bandgap or above. Due to the anisotropy of the equifrequency surfaces or the circular equifrequency contours, negative refraction of ultrasound occurs, thus resulting in focusing diverging sound beams. Moreover, when it comes to a 2D phononic crystal[29], the achieved resolution is above the diffraction limit and is much better than the resolution of conventional focusing transducers.

In addition, dynamic imaging of surface waves in the ultrasound regime has also been investigated on minute gold pyramid[31] or 2D phononic crystals[32]. Direct dynamic visualization of ultrasound waves provides insights into the underlying mechanism of ultrasound focusing, refraction and scattering. Therefore, it is believed that ultrasonic crystals could lead to a further development of ultrasonic imaging.

1.2.3. Hypersonic crystals

Hypersonic phononic crystals that operate at gigahertz (GHz) frequency regions are extremely interesting. Since hypersonic phononic crystals are nanocomposite materials with a period comparable to the wavelength of visible light, they possess potential for various simultaneous controls of light and sound by localizing or propagating them and for applications to novel acousto-optical devices utilizing the enhancement of acousto-optical interactions. Recently, the existence of simultaneous photonic and phononic bandgaps in composite materials with 2D periodic square or triangular cylinder arrays have been theoretically demonstrated.[33] It has been known that the introduction of point defects into photonic crystals causes strong localization of photons and enhances nonlinear optical phenomena.[34] In the same manner, the simultaneous localization of light and sound in the same spatial region by introducing point defects in photonic-phononic dual bandgap materials has been theoretically demonstrated.[35] This particular feature of photonic-phononic dual bandgap materials leads to drastic enhancement of acousto-optical interactions. In fact, Dainese *et al*. observed stimulated Brillouin scattering due to guided multi-GHz acoustic phonons confined in the core of the silica-air photonic crystal fiber (PCF).[36, 37] Such micro/nanostructuring of small-core PCFs alter both the optical and the acoustic properties of materials due to strong acoustic confinement in the core and changes in the acoustic dispersion relation. The ability to enhance acousto-optical interactions at GHz frequencies could lead to the development of a great variety of applications such as all-fiber acousto-optic devices[38], optical delay lines[39], high-efficiency light emission from silicon via phonon-confinement effects[40] and THz emission in semiconductor nanostructure due to the acoustoluminescence mechanism[41].

Hypersonic phononic crystals could also make a large impact on thermal management. The thermal energy transport of materials consists of contributions from both electrons and phonons. Regarding thermal transport, in some cases it is important to maximize this to cool nanodevices efficiently, while it should be minimized for thermoelectric devices, in which nanoscale structure is introduced to optimize acoustic wave scattering at high vectors. The ultimate efficiency of thermoelectric power generation systems is determined by the nondimensional figure of merit (ZT) of the materials, given by

$$\begin{aligned} ZT &= \frac{S^2\sigma T}{\kappa_T} \\ &= \frac{S^2\sigma T}{\kappa_p + \kappa_e} \end{aligned} \tag{1.1}$$

where S is the Seebeck coefficient, T is absolute temperature, σ is the electrical conductivity, κ_T is the total thermal conductivity, κ_p is the phonon thermal conductivity and κ_e is the electron thermal conductivity. The phonon contribution should be minimized to reach high *ZT*. The existence of a hypersonic phononic bandgap would reduce the flow of phonons and therefore the thermal conductivity of a material. Consequently, hypersonic phononic crystals are useful building blocks to reduce the phonon thermal conductivity, κ_p, in order to improve the performance of thermoelectric devices.

Self-assembly and lithography techniques make it possible to control periodic structures at nanoscales comparable to the wavelength of light and lead to the fabrication of hypersonic phononic crystals that have a phononic bandgap at GHz frequency. In most cases, BLS has been employed to investigate the phonon dispersion relations of hypersonic phononic crystals. Cheng *et al*. have demonstrated the first experimental observation of a hypersonic phononic bandgap in 3D colloidal composite materials.[42] They reported that a bandgap can be tuned by both the infiltrate material and particle size. Thereafter, Gorishnyy *et al*. have investigated the dispersion relations of single crystalline 2D phononic crystals based on epoxy, which consist of square arrays of air cylinders.[43] They observed a partial bandgap along the $[10]$ direction. In fact, measurements of the dispersion relations of single crystalline phononic structures were also done by Gorishnny *et al*. on 2D phononic crystals consisting of hexagonal arrays of air cylinders in the same epoxy matrix.[44] However, a phononic bandgap was unobservable since the bandgap position was at frequencies below the BLS detection limit due to the large lattice constant of the crystals (1.36 μm). In addition, Still *et al*. have discovered two hypersonic phononic bandgaps of different nature coexisting in 3D colloidal films.[45] One is a Bragg gap occurring at the edge of the first Brillouin zone and the other is a hybridization gap of crystalline and amorphous films, which originates from interaction of the band of quadropole particle eigenmodes with the acoustic effective-medium band. As just described, this gives rise to the possibility to create a structure with a negative modulus[46, 47], thus leading to the development of new functionalities such as acoustic superlenses[21, 48, 49] and acoustic cloaking[50, 51].

1.3. Aim of the study

Phononics is an extremely important field to develop functional materials based on hypersonic phononic crystals. The introduction of defects and waveguides makes it possible to localize and propagate the elastic waves and various controls of phonons are expected. Moreover, it is possible to dramatically slow down the sound velocity according to the peculiar phonon dispersibility. The acoustic technology in kHz region such as devices for medical diagnosis has been widely used. However, acoustic technology in both MHz and GHz regions remains many unknown applications. For example, in such a high frequency region, acoustic imaging with high spatial resolution on the nanoscale is expected and this might make it possible to visualize acoustically the structure and anisotropy in materials, which are impossible for the conventional optical microscope. Furthermore, in the energy field, converting waste heat into electricity reduces manufacturing cost while preserving the environment. Thermoelectric technology also provides an alternative to converting solar energy into electricity via solar thermoelectric energy conversion. Consequently, there have been research into improving the efficiency of thermoelectric power generation elements by controlling thermal transport of thermoelectric materials. Hypersonic crystals based on periodically arranged composite semiconductors[52] and superlattices[53] are promising materials for controlling thermal conduction.

As introduced in subsection 1.2.3, there have been relatively few investigations of hypersonic phononic crystals. Reasons for this includes difficulties in fabrication and characterization of hypersonic phononic crystals due to their inherent small lattice constants. BLS is a powerful and non-destructive technique that allows for the direct measurement of phonon dispersion relations along any direction in the Brillouin zone, thus leading to a further understanding of the detailed features of propagation bands. Until recently, the search of a hypersonic bandgap has been performed on hypersonic phononic crystlas based on thermoplastic polymers and epoxy, of which mechanical and thermal stability and elastic contrast are limited. On the other hand, although hypersonic phononic crystals based on a rigid material exhibit a large elastic contrast for bandgap formation, they have not been explored. AAO can be considered as a useful building block for hypersonic phononic crystals since it contains hexagonal arrays of aligned nanopores, and it is possible to change phonon density of states due to its lattice topology, lattice constant and pores diameter. In this thesis, hypersonic phononic crystals based on AAO, which is considered a rigid matrix, have been fabricated and their phonon dispersion relations have been investigated to verify how lattice constants, pore diameters or local properties and phase change of infiltrate materials affect the elastic wave propagation behavior at GHz frequencies.

In this thesis, the BLS apparatus and FDTD method, which were employed to study the properties of hypersonic phononic crystals, are described in chapter 2. In chapter 3, fabrication of AAO is described. Here, two widely used methods of fabricating AAO, i.e. two-step anodization and pre-molding anodization, are described. The former method leads to a polydomain structure, while the latter method results in an ideally ordered pore lattice. Furthermore, basic properties of AAO is described. Chapter 4 deals with AAO with a lattice constant of 100 nm and a pore diameter varying from 35 to 85 nm as hypersonic phononic crystals. The hypersonic phononic properties of air- and poly(dimethylsiloxane) (PDMS)-infiltrated AAO were examined using BLS. In addition, the FDTD method was used to calculate the theoretical phononic dispersion relations, and the details of the displacement fields were considered for various modes in these structures. Tailor-made phononic properties embracing anisotropic elastic properties parallel and perpendicular to the pore axes and phonon localization are explored. The effect of the elastic contrast between AAO matrix and inclusions on the phonon dispersion relations was investigated in chapter 5. It was found out that a bending of the first propagation band occurs for high elastic contrast hybrid system due to the phonon localization in the pores, while it does not occur for low elastic contrast hybrid system. In addition, reversible switching of phononic properties can be achievable in the response to temperature. Monodomain AAO-based hypersonic phononic crystals were treated in chapter 6. High rotational symmetries promote the ability to obtain complete phonon dispersion relations. Here, the underlying physical origin of complete phonon dispersion relations for two different porosities were considered.

On the basis of these results, the main conclusions of this study are summarized in chapter 7 and many promising directions for future investigations are described in chapter 8.

2. Methodology

This chapter provides a brief description of experimental techniques and phonon dispersion calculation methods used in this thesis. It includes three sections: section 2.1 describes the mathematics of elastic wave propagation in periodic structures, in particular in hexagonal structures; section 2.2 treats the physics of Brillouin light scattering and describes optical interferometric techniques; and section 2.3 describes Brillouin light scattering experimental apparatus, which is used as the main characterization tool to measure phonon dispersion relations in nanocomposites and two different scattering geometries, which reveal the anisotropic phonon propagation in two-dimensional hypersonic phononic crystals. A sufficient amount of detail is provided for a solid understanding of these techniques and their use in phononic, while additional information is available in the references mentioned in the text and listed at the end of this thesis.

2.1. Elastic wave propagation in periodic media

The field equations for elastic waves in a medium can be derived from the laws of conservation of mass, momentum, energy and angular momentum. The conservation of mass leads to the equation of continuity

$$\frac{d\rho}{dt} + \rho\nabla \cdot v = 0 \tag{2.1}$$

From the conservation of momentum the Cauchy equation of motion is deduced, which is

$$\nabla \cdot \sigma - \rho\frac{\partial v}{\partial t} = 0 \tag{2.2}$$

in linear approximation for non-polar materials in the absence of external forces and damping. The density of mass $\rho = \rho(\mathbf{r}, t)$ depends on time t and position $\mathbf{r}$. $v(\mathbf{r}, t)$ is the velocity of the particles calculated by partially differentiating the displacement field $u(\mathbf{r},t)$ with respect to time. The equation of motion for an elastic medium derived from Equation 2.1 and 2.2 is

$$\rho(\mathbf{r})\frac{\partial^2\mathbf{u}}{\partial t^2} = \nabla \cdot \sigma \tag{2.3}$$

where ρ is the density, $u_i(\mathbf{r}, t)$ is the *i*-th component of the displacement vector at point **r** and time *t*, and $\sigma_{ij} = \sigma_{ij}(\mathbf{r}, t)$ is the component of the stress tensor.

$$\sigma_{ij} = c_{ijmn}u_{mn} \tag{2.4}$$

where c_{ijmn} is the stiffness tensor of the medium, $\sigma_{ij} = \lambda(\mathbf{r})u_{ll}\delta_{ij} + 2\mu(\mathbf{r})u_{ij}$ and $u_{mn} = \frac{1}{2}\left(\frac{\partial u_i}{\partial x_j} + \frac{\partial u_j}{\partial x_i}\right)$ is the strain tensor in the medium. $\lambda(\mathbf{r})$ and $\mu(\mathbf{r})$ are the so-called Lam$\acute{e}$ coefficients of the medium.[54] The λ, μ and ρ are related to the velocities in a medium through the relations $\lambda = \rho c_l^2 - 2\rho c_t^2$ and $\mu = \rho c_t^2$, where c_l and c_t are the longitudinal and transverse velocity, respectively. Therefore, the longitudinal and transverse velocity can be expressed as $c_l = \sqrt{\lambda + 2\mu/\rho}$ and $c_t = \sqrt{\mu/\rho}$. The number of independent components in the stiffness tensor is determined by the material symmetry. Although there are 21 independent elastic constants for general anisotropic materials, the number of independent constants in transverse isotropic materials are reduced to 5 from a total of 21. In the case of hexagonal symmetry, the elastic stiffness tensor has the form

$$c_{hexagonal} = \begin{pmatrix} c_{11} & c_{12} & c_{13} & 0 & 0 & 0 \\ c_{12} & c_{11} & c_{13} & 0 & 0 & 0 \\ c_{13} & c_{13} & c_{33} & 0 & 0 & 0 \\ 0 & 0 & 0 & c_{44} & 0 & 0 \\ 0 & 0 & 0 & 0 & c_{44} & 0 \\ 0 & 0 & 0 & 0 & 0 & c_{66} \end{pmatrix} \tag{2.5}$$

where the tensor component c_{66} is given by

$$c_{66} = \frac{1}{2}\left(c_{11} - c_{12}\right) \tag{2.6}$$

Figure 2.1 is a schematic of periodic media which is investigated as phononic crystals in this thesis. The structure is made up of hexagonally arranged long air, solid or liquid cylinders parallel in an alumina matrix. The *z* axis is assumed to be perpendicular to the plane and parallel to the cylinders. The lattice constant is *a* and the diameter of the cylinder is *d*. The row matrix is assumed to be hexagonal symmetry with its crystallographic axes oriented along the coordinate axes *x*, *y* and *z* as shown in Fig. 2.1. The elastic waves are assumed to propagate in the *x*-*y* plane and the *z* direction. The elastic wave equation in such a system is expressed as:

$$\frac{\partial^2 u_x}{\partial t^2} = \frac{1}{\rho}\left(\frac{\partial \sigma_{xx}}{\partial x} + \frac{\partial \sigma_{xy}}{\partial y}\right) \tag{2.7}$$

$$\frac{\partial^2 u_y}{\partial t^2} = \frac{1}{\rho}\left(\frac{\partial \sigma_{xy}}{\partial x} + \frac{\partial \sigma_{yy}}{\partial y}\right) \tag{2.8}$$

$$\frac{\partial^2 u_z}{\partial t^2} = \frac{1}{\rho}\left(\frac{\partial \sigma_{zx}}{\partial x} + \frac{\partial \sigma_{zy}}{\partial y} + \frac{\partial \sigma_{zz}}{\partial z}\right) \tag{2.9}$$

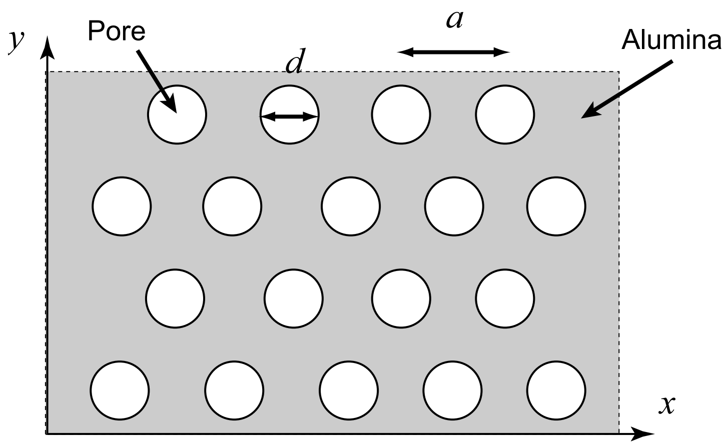

Figure 2.1.: Two-dimensional cross section of a hexagonal array of pores with a lattice constant of *a* and diameter *d*.

where u_x and u_y are the *x*- and *y*-component of the displacement field. For simplicity, the displacement field **u** is taken independent on *z*, and all materials are supposed to obey the isotropic Hook's law. In these conditions,

$$\sigma_{xx} = c_{11}\frac{\partial u_x}{\partial x} + c_{12}\frac{\partial u_y}{\partial y} \tag{2.10}$$

$$\sigma_{yy} = c_{11}\frac{\partial u_y}{\partial y} + c_{12}\frac{\partial u_x}{\partial x} \tag{2.11}$$

$$\sigma_{zz} = c_{13}\frac{\partial u_x}{\partial x} + c_{13}\frac{\partial u_y}{\partial y} + c_{33}\frac{\partial u_z}{\partial z} \tag{2.12}$$

$$\sigma_{xy} = \frac{c_{66}}{2}\left(\frac{\partial u_y}{\partial x} + \frac{\partial u_x}{\partial y}\right) \tag{2.13}$$

$$\sigma_{yz} = \frac{c_{44}}{2}\left(\frac{\partial u_z}{\partial y} + \frac{\partial u_y}{\partial z}\right) \tag{2.14}$$

$$\sigma_{xz} = \frac{c_{44}}{2}\left(\frac{\partial u_z}{\partial x} + \frac{\partial u_x}{\partial z}\right) \tag{2.15}$$

where c_{11}, c_{12}, c_{13}, c_{44} and c_{66} are the position-independent elastic constants, which are related to the longitudinal and transverse sound velocities c_l and c_t: $c_{11} = \rho c_l^2$ and $c_{66} = \rho c_t^2$.

The second-order time-differential equation 2.3 can conveniently be written in a set of canonical, first-order equations[14]:

$$-\rho\frac{\partial v_i}{\partial t} = \frac{\partial \sigma_{ij}}{\partial x_j} \tag{2.16}$$

$$v_i = \frac{\partial u_i}{\partial t} \tag{2.17}$$

where v_i is the velocity field. These equations are solved by the finite difference time domain (FDTD) method[25, 55], using central difference. The FDTD method is a useful numerical analysis method for the solution of a number of problems in electromagnetics. It has recently been applied to the study of the transmission spectra[14, 25], dispersion relations[55] and mapping of the displacement field[56, 57] in phononic crystals. Owing to a periodic system, the relational equation, which satisfies the Bloch theorem, for the displacement and the stress tensor can be expressed as[55]

$$u_i\left(\mathbf{r},t\right) = \exp\left(\mathbf{k}\cdot\mathbf{r}\right) U_i\left(\mathbf{r},t\right) \tag{2.18}$$

$$\sigma_{ij}\left(\mathbf{r},t\right) = \exp\left(\mathbf{k}\cdot\mathbf{r}\right) S_{ij}\left(\mathbf{r},t\right) \tag{2.19}$$

where $\mathbf{r}$ is a position in x-y plane, $\mathbf{k} = (k_x, k_y)$ is a Bloch wavevector, $U_i(\mathbf{r}, t)$ and $S_{ij}(\mathbf{r}, t)$ are Bloch's boundary conditions satisfying $U_i(\mathbf{r} + \mathbf{R}, t) = U_i(\mathbf{r}, t)$ and $S_{ij}(\mathbf{r} + \mathbf{R}, t) = S_{ij}(\mathbf{r}, t)$ with $\mathbf{R}$ being a lattice translational vector.

The FDTD algorithm is based on discretization of the equation in spatial and time domain. The FDTD method solves the elastic wave equations by discretizing time and space and replacing derivatives by finite differences. Discritization of the equations is expressed as

$$-\rho\frac{v_i(t+\Delta t/2)-v_i(t-\Delta t/2)}{\Delta t} = \frac{\sigma_{ij}(x+\Delta x/2)-\sigma_{ij}(x-\Delta x/2)}{\Delta x_j} \tag{2.20}$$

The dispersion curves are calculated using (i) a two-dimensional unit cell, which is repeated in the two spatial directions, (ii) the Bloch theorem, which introduces the wave vector **k**. In the *z* direction, the length of the unit cell *c* is chosen so that the plane and cylinders as well as a thin layer of vacuum on both sides are embedded in order to decouple the interaction between neighboring cells. For each component of the wavevector (k_x, k_y) parallel to the plane, an initial random displacement is applied inside the unit cell at the origin of time. Then, the displacement field is recorded at many positions in the unit cell as a function of time and, finally, Fourier transformed to obtain the eigenfrequencies of the structure for the chosen wavevector. Therefore, the band structures are computed in terms of frequency as a function of the wavevector and plotted along the principal directions of the 2D irreducible Brillouin zone (ΓJX).

The displacement field calculation is similar to the dispersion curves computation except that the initial randomly excitation of the displacement is replaced by a periodic wave source during a determined time at two specific points of the unit cell. The source generates a quasi monochromatic wave at the same frequency than the eigenfrequency of the chosen wave vector. Because both the wave vector and the frequency are assigned, the specific eigenmode is excited and the displacement field is recorded to highlight the properties of the mode. In those 3D graph representations, the color and the size of the points symbolize the local displacement while the white color corresponds to a displacement equal to zero.

2.2. Brillouin light scattering

2.2.1. The photoelastic effects

Brillouin light scattering (BLS) arises as a result of acousto-optical interactions in a scattering medium. We consider a nonmagnetic, nonconducting and nonabsorbing medium with the dielectric constant ε_0. In complex notation, an electromagnetic wave of a plane incident wave is expressed as

$$\mathbf{E}_i = \mathbf{n}_i E_0 \exp i(\mathbf{k}_i \cdot \mathbf{r} - \omega_i t) \tag{2.21}$$

where a unit vector in the direction of the incident electromagnetic field is $\mathbf{n}_i$, the amplitude of the electromagnetic field is E_0, the wavevector is $\mathbf{k}_i$ and the angular frequency is ω_i. The scattered electric field at a large distance *R* from the scattering volume with polarization $\mathbf{n}_s$, propagation vector $\mathbf{n}_i$ and frequency ω_s is[58]

$$E_s(R,t) = \frac{E_0}{4\pi R\varepsilon_0} \exp ik_s R \int_V d^3r \exp i(\mathbf{q}\cdot\mathbf{r}-\omega_i t)\,[\mathbf{n}_s \cdot [\mathbf{k}_s \times (\mathbf{k}_s \times (\delta\boldsymbol{\epsilon}(\mathbf{r},t)\cdot\mathbf{n}_i)]] \tag{2.22}$$

where $\mathbf{q}$ is the scattering wavevector and $\delta\varepsilon(\mathbf{r},t)$ is the dielectric constant fluctuation. The scattering wavevector $\mathbf{q}$ is defined as the vector difference between the wavevectors of the incident light ($\mathbf{k}_i$) and the scattered light ($\mathbf{k}_s$), i.e. $\mathbf{q}$ = $\mathbf{k}_s$ - $\mathbf{k}_i$. It is usually the case that the wavelength of the incident light and scattered light is changed very little in the scattering process so that $|\mathbf{k}_i| \cong |\mathbf{k}_s|$. Consequently, the magnitude of $\mathbf{q}$ can be expressed in terms of the

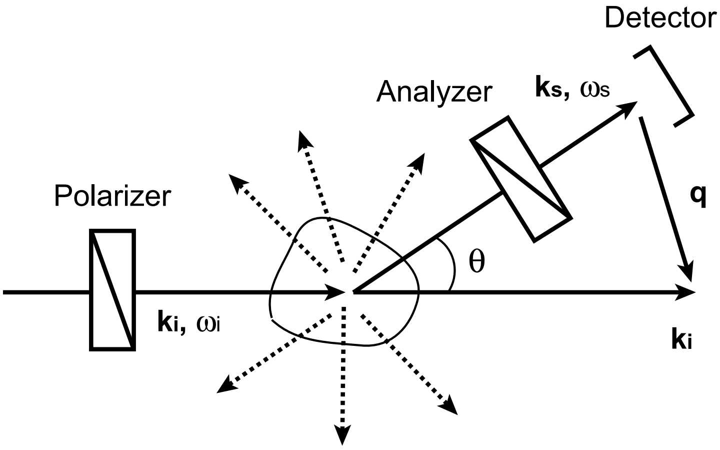

Figure 2.2.: Schematic of light scattering geometry. Polarized light is incident on a sample and scattered in all directions. The scattering vector $\mathbf{q}$ = $\mathbf{k}_i$ - $\mathbf{k}_i$ is defined by the detector position.

scattering geometry shown in Fig. 2.2 as

$$q^2 = |\mathbf{k}_s - \mathbf{k}_i|^2 = k_s^2 + k_i^2 - 2\mathbf{k}_i \cdot \mathbf{k}_s = 4k_i^2 \sin^2\frac{\theta}{2} \tag{2.23}$$

$$q = 2k_i \sin\frac{\theta}{2} = \frac{4\pi n}{\lambda}\sin\frac{\theta}{2} \tag{2.24}$$

The intensity of photon-phonon scattering depends strongly on the dielectric fluctuation related to elastic deformations on the optical properties of media. Following treatment by Landau for an isotropic medium[59], the electric field of the scattered light $\mathbf{E}_s$ is proportional to the vector product ($\mathbf{n}\times(\mathbf{n}\times\mathbf{G})$), where **n** is a unit vector in the scattering direction, and the components of the vector **G** are given by the integral

$$\mathbf{G} = \int \delta\epsilon_{ik} \exp(-i\mathbf{q}_s \cdot \mathbf{r}) dV \cdot e_k \tag{2.25}$$

Here **e** is a unit vector parallel to the incident electric field vector $\mathbf{E}_i = \mathbf{e}E_0 \exp(i\mathbf{q}\cdot\mathbf{r})$; $\delta\epsilon$ is the change in the electrical permittivity due to the elastic deformation - $\delta\epsilon_{ik} = a_1 u_{ik} + a_2 u_{ll}\delta_{ik}$, where $u_{ik} = \frac{1}{2}\left(\frac{\partial u_i}{\partial x_k} + \frac{\partial u_k}{\partial x_i}\right)$ is a strain tensor and a_1 and a_2 are the photo-elastic constants of the medium.

When an acoustic wave propagates through the medium, it creates modulations of in the dielectric constant ε, which, in turn, scatter light. The dielectric constant of the medium is then

$$\epsilon = \epsilon_0 + \delta\epsilon_{ij} \tag{2.26}$$

where ε_0 is the dielectric constant of the unmodulated medium and

$$\delta\epsilon_{ij} = \sum_{jk} p_{ijkl} u_{kl} \tag{2.27}$$

Here u_{kl} is the strain tensor and p_{ijkl} is the forth rank tensor known as a photo-elastic tensor. This tensor describes the response of the medium to the propagating acoustic wave. The number of its independent coefficients depends on the symmetry of the medium. In particular, for hexagonal crystals the matrix of photo-elastic tensor has the form

$$p_{hexagonal} = \begin{pmatrix} p_{11} & p_{12} & p_{13} & 0 & 0 & 0 \\ p_{12} & p_{11} & p_{13} & 0 & 0 & 0 \\ P_{13} & p_{13} & p_{33} & 0 & 0 & 0 \\ 0 & 0 & 0 & p_{44} & 0 & 0 \\ 0 & 0 & 0 & 0 & p_{44} & 0 \\ 0 & 0 & 0 & 0 & 0 & p_{66} \end{pmatrix} \tag{2.28}$$

where the tensor component p_{66} is given by

$$p_{66} = \frac{1}{2}(p_{11} - p_{12}) \tag{2.29}$$

The integral **G** is also referred to as the spatial Fourier transform of the dielectric fluctuation $\delta\boldsymbol{\varepsilon}(\mathbf{q}, t)$, such that

$$\delta\boldsymbol{\epsilon}(\mathbf{q}, t) = \int_V d^3r \exp i\mathbf{q} \cdot \mathbf{r}\ \delta\boldsymbol{\epsilon}(\mathbf{r}, t) \tag{2.30}$$

Then, Equation 2.22 is written as

$$E_s(R, t) = \frac{E_0}{4\pi R\epsilon_0} \exp i(k_s R - \omega_i t) \left\{\mathbf{n}_s \cdot [\mathbf{k}_s \times \mathbf{k}_s \times (\delta\boldsymbol{\epsilon}(\mathbf{q}, t) \cdot \mathbf{n}_i)]\right\} \tag{2.31}$$

The use of the vector products leads to the simplification of Equation 2.31 as

$$E_s(R, t) = \frac{E_0}{4\pi R\varepsilon_0} \exp i(k_s R - \omega_i t)\delta\boldsymbol{\epsilon}_{is}(\mathbf{q}, t) \tag{2.32}$$

where $\delta\epsilon_{is}(\mathbf{q}, t) \equiv \mathbf{n}_s \cdot \delta\boldsymbol{\epsilon}(\mathbf{q}, t) \cdot \mathbf{n}_i$ is the component of the dielectric constant fluctuation tensor along the initial and final polarization directions. Considering the time-averaged intensity of the scattered light, the time-correlation function of E_s can be expressed as

$$\langle E_s^*(R, 0)E_s(R, t)\rangle = \frac{k_s^4 \left|E_0\right|^2}{16\pi^2 R^2 \epsilon_0^2} \langle \delta\epsilon_{is}(\mathbf{q}, 0)\delta\epsilon_{is}(\mathbf{q}, t)\rangle\ \exp(-i\omega_i t) \tag{2.33}$$

The intensity of the scattered light I_{is} is therefore given by

$$\begin{aligned} I_{is}(\mathbf{q}, \omega_s, R) &= \int dt\, \langle E_s^*(R, 0)E_s(R, t)\rangle \exp i\omega_s t \\ &= \left[\frac{I_0 k_s^4}{16\pi^2 R^2 \epsilon_0^2}\right] \int dt\, \langle \delta\epsilon_{is}(\mathbf{q}, 0)\delta\epsilon_{is}(\mathbf{q}, t)\rangle \exp(i(\omega_s - \omega_i)t) \end{aligned} \tag{2.34}$$

The features of Equation 2.34 are as follows: (i) I_{is} is inversely proportional to the forth power of the wavelength λ; (ii) I_{is} is attenuated inversely with the square of a distance *R* for a spherical wave; and (iii) I_{is} depends on the frequency change $\omega \equiv \omega_i - \omega_s$ in the scattering process. The frequency change is accompanied by a variation with time of the dielectric constant fluctuation $\delta\boldsymbol{\varepsilon}(\mathbf{q}, t)$. Equation 2.34 can thus be rewritten by the spectral density of the dielectric fluctuations such that

$$I_{is}^{\epsilon}(\mathbf{q}, \omega) = \left[\frac{I_0 k_s^4}{16\pi^2 R^2 \epsilon_0^2}\right] \int dt\, \langle \delta\epsilon_{is}^*(\mathbf{q}, 0)\delta\epsilon_{is}(\mathbf{q}, t)\rangle \exp(i\omega t) \tag{2.35}$$

What is measured in BLS spectroscopy is $I_{is}^{\varepsilon}(\mathbf{q}, \omega)$ induced by the local dielectric constant fluctuations, which is in turn thermal fluctuations at a given scattering angle as a function of ω. Therefore, BLS can provide insight into diverse dynamic processes in a medium.

2.2.2. Interaction with hypersound

When light travels through a medium, light is scattered by hypersound propagating in a medium, and this scattered light is accompanied with the frequency shifts. Since the refractive index of a liquid or solid medium is changed by thermal vibration, i.e. phonon, which functions as a kind of diffraction grating for light, the incident light is scattered in a certain direction as shown in Fig. 2.3.

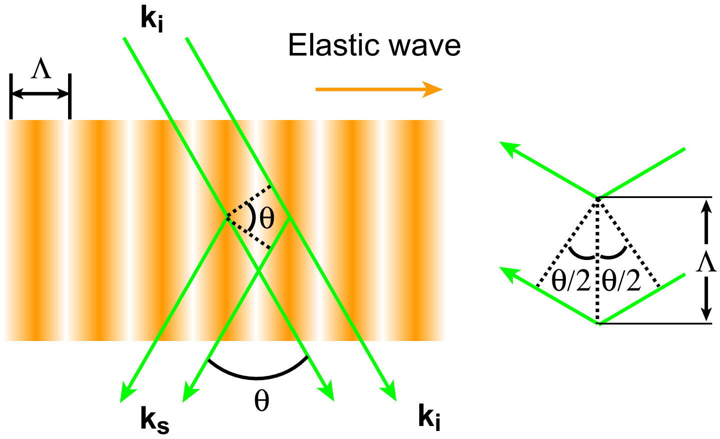

Figure 2.3.: Acoustic Bragg reflection.

Consider the interaction of a light wave with wavelength λ and an elastic wave with the wavelength Λ. When the wave-front of the elastic wave and light with the incident angle of $\theta/2$ satisfies the following equation

$$2\Lambda n \sin\frac{\theta}{2} = \lambda \tag{2.36}$$

the scattered light in each wave-front undergoes constructive interference and is reinforced. Since this phenomenon is the same as the Bragg reflection of X-ray observed in the crystal lattice plane with a lattice constant Λ, it is also called acoustic Bragg reflection. This Bragg condition, Equation 2.36, can also be expressed as

$$\frac{2\pi}{\Lambda} = \frac{4\pi n}{\lambda}\sin\frac{\theta}{2} \tag{2.37}$$

where $\mathbf{K} = 2\pi/\Lambda$ is the wavevector of the elastic wave. Therefore, from Equation 2.24 and 2.37, the relationship between the scattering wavevector and the wavevector of the elastic wave yields

$$q = \frac{2\pi}{\Lambda} \tag{2.38}$$

Equation 2.38 indicates that the wavevector of the elastic wave **K** is equivalent to the scattering wavevector **q**. As a result, a different **q** is selected by the change of the scattering angle θ, thus resulting in probing the elastic waves of different wavelengths.

When the wavelength (Λ) of the elastic wave and the wavelength of light (λ) satisfy the Equation 2.36, the relationship between the wavevector of the elastic wave **K** and the wavevector of the incident and scattered light ($\mathbf{k}_i$ and $\mathbf{k}_s$) can be expressed as

$$\mathbf{k}_s = \mathbf{k}_i \pm \mathbf{K} \tag{2.39}$$

Multiplying both sides by $\hbar$ = h/2, Equation 2.39 can be expressed as

$$\hbar\mathbf{k}_s = \hbar\mathbf{k}_i \pm \hbar\mathbf{K} \tag{2.40}$$

This corresponds to the law of crystal momentum conservation. Here the upper sign refers to processes in which a phonon is absorbed (known as the *anti-Stokes* component of the scattered radiation) and the lower sign refers to processes in which a phonon is emitted (the *Stokes* component).

In addition, when light is scattered by hypersound, the frequency of the scattered light is shifted since the incident light undergoes the Doppler effect. A shift in frequency Δf of the scattered light is expressed as

$$\Delta f = \pm\frac{2nf_iV}{c}\sin\frac{\theta}{2} \tag{2.41}$$

where Δf (= f_s - f_i) is a frequency shift, n is a refractive index of a medium, V is a phonon phase velocity and c is the speed of light. Consequently, Equation 2.41 leads to

$$\begin{aligned} f_s &= f_i \pm \frac{2nf_iV}{c}\sin\frac{\theta}{2} = f_i \pm \frac{V}{2\pi}\cdot\frac{4\pi n}{\lambda_i}\sin\frac{\theta}{2} \\ &= f_i \pm \frac{V}{2\pi}q \end{aligned} \tag{2.42}$$

Equation 2.42 relates the phonon phase velocity, which has the form $\Omega(\mathbf{q}) = V(\mathbf{q})q$, to shift in photon energy by

$$\omega_s = \omega_i \pm \Omega \tag{2.43}$$

where ω_s, ω_i and Ω are the angular frequencies of the scattered light, the incident light and the elastic wave, respectively. Multiplying both sides by $\hbar$, Equation 2.43 can be expressed as

$$\hbar\omega_s = \hbar\omega_i \pm \hbar\Omega \tag{2.44}$$

This corresponds to the law of energy conservation.

Since Equations 2.40 and 2.44 describe the light scattering process, this phenomenon can be regarded as the collision between phonons and photons. Therefore, the phonon dispersion relation $\Omega(\mathbf{q}) = V(\mathbf{q})q$ can be observed by probing the angular frequency shift ω_s - ω_i of the scattered light as a function of $\mathbf{k}_s$ - $\mathbf{k}_i$. This technique is an effective way to obtain information on thermal phonons. The Brillouin shift is commonly measured by the use of a Brillouin spectrometer based on a Fabry-Perot interferometer.

2.2.3. Optical interferometric techniques

2.2.3.1. Single-pass Fabry-Perot interferometer

Brillouin light scattering arises from the third-order nonlinear effect, which is related to acoustic phonons. In a typical Brillouin scattering experiment one reveals acoustic or spin waves with frequencies between 1 and 100 GHz. In order to extract the weak inelastic component of light from the elastically scattered contribution, a high-resolution spectrometer is required. To this aim, the best combination of high resolution and good throughput is achieved using a Fabry-Perot interferometer as a scanning spectrometer.

First of all, we consider a single-pass Fabry-Perot interferometer. The Fabry-Perot interferometer is based on multiple beam interference and was first built by Charles Fabry and Alfred Perot in the late 1800s. In principle, the Fabry-Perot interferometer consists of two parallel highly reflecting mirrors designed to induce multiple reflections of light between the mirror surfaces separated by some distance. The single-pass transmission function of a planar mirror Fabry-Perot interferometer can be expressed as

$$T = \frac{T_0}{1 + (4F^2/\pi^2)\sin^2(2\pi L/\lambda)} \tag{2.45}$$

where T_0 is the overall single-pass transmission, F is the effective single-pass finesse, L is the mirror spacing and λ is the wavelength of light. Equation 2.45 indicates that the Fabry-Perot interferometer only transmits light with wavelengths λ, satisfying the relation

$$L = \frac{1}{2}m\lambda \tag{2.46}$$

for integers m. The optical transmission function is illustrated in Fig. 2.4. Provided that the mirror spacing L is varied in order to scan the transmitted light at different wavelengths satisfying Equation 2.46, the Fabry-Perot interferometer functions as an extremely high resolving power spectrometer. Consequently, one can increase the free spectral range by decreasing the

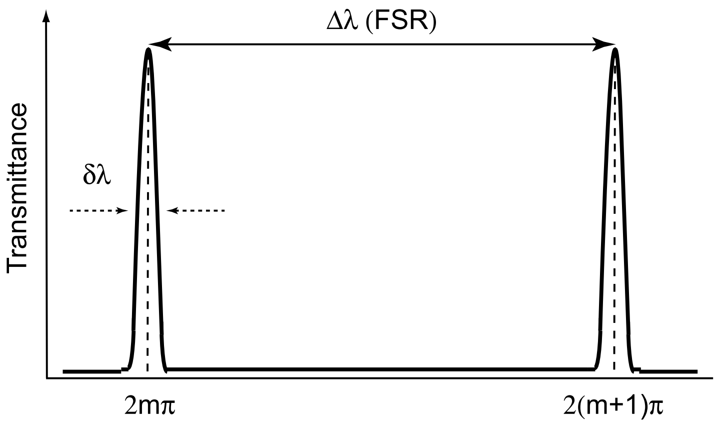

Figure 2.4.: The optical transmission function of a single-pass Fabry-Perot mirror.

mirror spacing *L* as

$$\Delta\lambda = \frac{\lambda^2}{2L} \tag{2.47}$$

The performance of a Fabry-Perot interferometer is determined by several parameters such as finesse, contrast defined as the ratio of peak height to the minimum intensity, resolution, and free spectral range (FSR), which is the largest wavelength range ($\Delta\lambda$ in Fig. 2.4) for a given order that does not overlap the same range in an adjacent order. In practice, it is the convention to express FSR in units of frequency (Hz) or wavenumber (cm^{-1}). The measurement precision of frequency or wavelength, which is represented by the finesse *F*, is determined by the sharpness of interference fringes. The finesse is a quality factor which characterizes the width or the sharpness of the peak maxima. This finesse is limited by the mirror reflectivity and flatness and related to the spacing between transmitted wavelengths $\Delta\lambda$ and the full width at half maximum (FWHM) $\delta\lambda$ of a given transmission peak given by

$$F = \frac{\Delta\lambda}{\delta\lambda} \tag{2.48}$$

However, this will also increase $\delta\lambda$ and reduce the resolution. Moreover, the finesse is practically less than 100 due to the limited quality of mirror substrates and coatings.[60] Therefore, it is necessary to optimize the mirror spacing *L* for each experiment according to the lowest and the highest frequencies to be recorded. One must sometimes use several mirror spacings for each sample to complete whole phonon dispersion relations. Consequently, the FSR is a very important parameter to be fixed prior to conducting BLS experiments.

2.2.3.2. Tandem Fabry-Perot interferometer

Since its invention, a Fabry-Perot interferometer has been a well-established spectroscopic instrument. However, it was realized that a single-pass Fabry-Perot has some difficulties in observing spectroscopic signals due to low contrast and the overlapping of orders. Therefore, there have been numerous efforts to improve contrast and the overlapping issue. Houston[61] have introduced the use of two interferometers of different spacings in series. In this method, the advantages of the high resolving power and the large FSR for the large and small spacing interferometers are combined. The purpose of the small spacing interferometer is the suppression of the overlapping orders of the large spacing interferometer. Bradley and Kuhn[62, 63] have demonstrated the use of two identical Fabry-Perot interferometers in series to increase contrast. An alternative to increasing contrast and resolution using double-passed Fabry-Perot interferometer was suggested by Hariharan and Sen[64]. The contrast and finesse of the Fabry-Perot interferometer are also increased by routing light sequentially through two different optical paths.

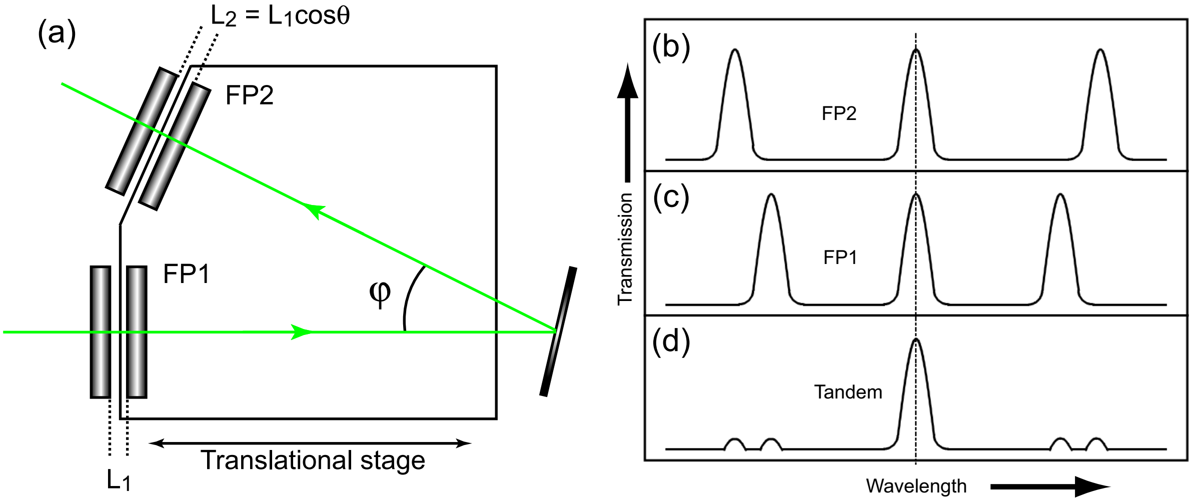

Figure 2.5.: Tandem interferometer with mechanical coupling of the movable plate.

Increased contrast, resolution and FSR can be achieved by using two Fabry-Perot interferometer. Yet multipass Fabry-Perot interferometers mentioned above lack sufficient contrast to observe weak Brillouin signal components in the presence of intense elastically scattered light. In order to overcome this issue, Sandercock[65] introduced an elegant design for a piezoelectrically scanned tandem multipass Fabry-Perot interferometer. Two interferometers of unequal mirror spacing are arranged in a series with their axes inclined at φ, and with their scanning mirrors mounted on a common stage as shown in Fig. 2.5(a).

When two interferometers, of which spacings are L_1 and L_2, are arranged in series and adjusted to transmit simultaneously, the change in optical length ΔL satisfies the following condition:

$$\frac{\Delta L_1}{\Delta L_2} = \frac{L_1}{L_2} \tag{2.49}$$

In the case of a tandem Fabry-Perot interferometer shown in Fig. 2.5(a) the two interferometers are arranged in series with their axes inclined at an angle θ. Thus,

$$\frac{L_1}{L_2} = \frac{\Delta L_1}{\Delta L_2} = \frac{1}{\cos\varphi} \tag{2.50}$$

Therefore, provided the mirror spacings are in a ratio of $1/\cos\varphi$, condition 2.49 is satisfied.

Considering the condition of two interferometers arranged in series, the wavelengths transmitted by the combination must simultaneously satisfy

$$L_1 = \frac{1}{2}m_1\lambda \tag{2.51}$$

$$L_2 = \frac{1}{2}m_2\lambda \tag{2.52}$$

for integral values of m_1 and m_2. Since FP1 and FP2 show different FSR due to the slight difference in their spacings as shown in Fig. 2.5(b) and (c), the neighboring order transmission peaks do not coincide. Consequently, the combined transmission of light passing through both FP1 and FP2 is illustrated in Fig. 2.5(d). In this thesis, a six-pass tandem Fabry-Perot (TPF)

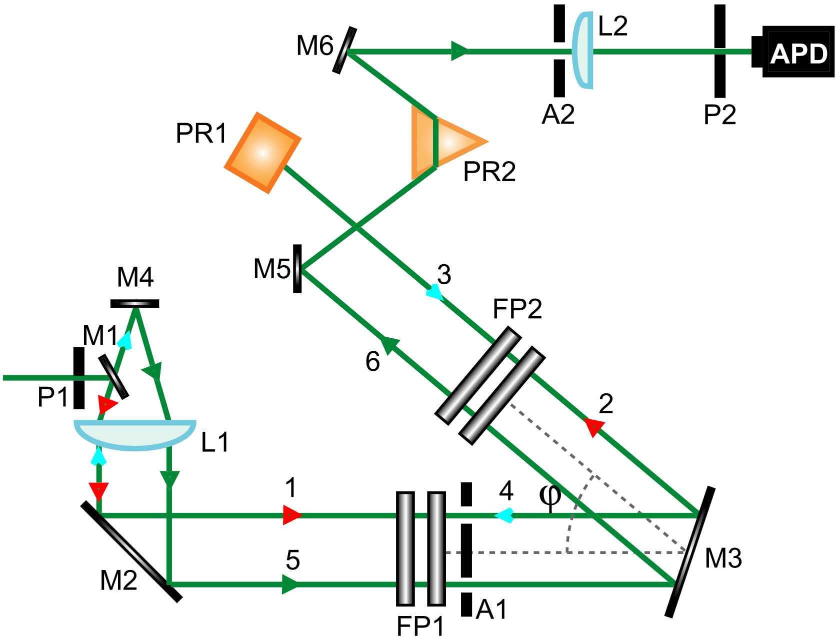

Figure 2.6.: The optical path inside a tandem Fabry-Perot interferometer invented by JRS Scientific Instruments. (Adopted from Ref. [60])

interferometer designed by JRS Scientific instruments was used. The optical path passing through a six-pass TPF interferometer is schematically shown in Fig. 2.6.[60] The scattered light enters through a pinhole P1 and is reflected from a mirror M1 towards the lens L1 which collimates the scattered light. Then the collimated scattered light is reflected from mirrors M2 and M3 to pass through both sets of Fabry-Perot mirrors FP1 and FP2, as indicated by red arrows 1 and 2 in Fig. 2.6. After passing through FP2, a 90 ° prism PR1 reflects light back parallel to its original trajectory to pass through FP1 and FP2 again and light reaches a mirror M4 upon the reflection by M3 and M2, as indicated with cyan arrows 3 and 4 in Fig. 2.6. Upon the reflection by M4 light passes once more through FP1 and FP2 and then is directed by mirrors M5, M6 and a prism PR2 to reach an Avalanche photodiode (APD), as indicated with green arrows 5 and 6 in Fig. 2.6.

2.3. Experimental setup

2.3.1. Brillouin light scattering apparatus

All BLS measurements were conducted on a six-pass Tandem Fabry-Perot interferometer (JRS Scientific Instruments). Figure 2.7 shows the experimental setup for the BLS measurements. The Nd:YAG laser (COHERENT, 100 mW, λ = 532 nm) was used as the light source. The laser beam, which is vertical (V or s-polarization) relative to the scattering plane adjusted by a polarizer, was focused with a lens to a spot size of about 200 μm on the sample. The scattered light was collected and focused by two lens into the pinhole (P1) of the Tandem Fabry-Perot interferometer. The plane of polarization of the scattered light, which is either vertical (V or *s*-polarization) or horizontal (H or *p*-polarization) relative to the scattering plane, is adjusted with an analyzer. A single-photon Avalanche photodiode (APD) detected the scattered light passing through the Tandem Fabry-Perot interferometer. The scattering angle θ is changed by rotating the goniometer on which the light source is mounted. Scattering angles from 25 ° to 150 ° could be measured.

Figure 2.8 shows a customized sample holder used in the present study[66]. It consists of a cylindrical metallic body and a quartz optical cell which allows for BLS measurements at temperature up to 473 K. The system is resistively heated with a 100 Ω platinum RTD temperature sensor embedded in the metallic body to provide feedback for the heater. Another RTD temperature sensor is mounted close to the sample to obtain the sample temperature. The temperature of the system is stabilized within $\pm$0.2 K.

In this thesis, the polarizations of light are all vertical (V) or horizontal (H) relative to the scattering plane. We denote the polarization of excitation field and probe field in that order, i.e., VH denotes V excitation and H probe, while VV denotes all V polarizations. VV is called the *polarized* component, while VH is called the *depolarized* component. All the measurements described herein were conducted with one of these two polarization combinations. The specific components of the dielectric fluctuations are related to each of these spectral components. It follows that the relation between the dielectric fluctuations and polarization

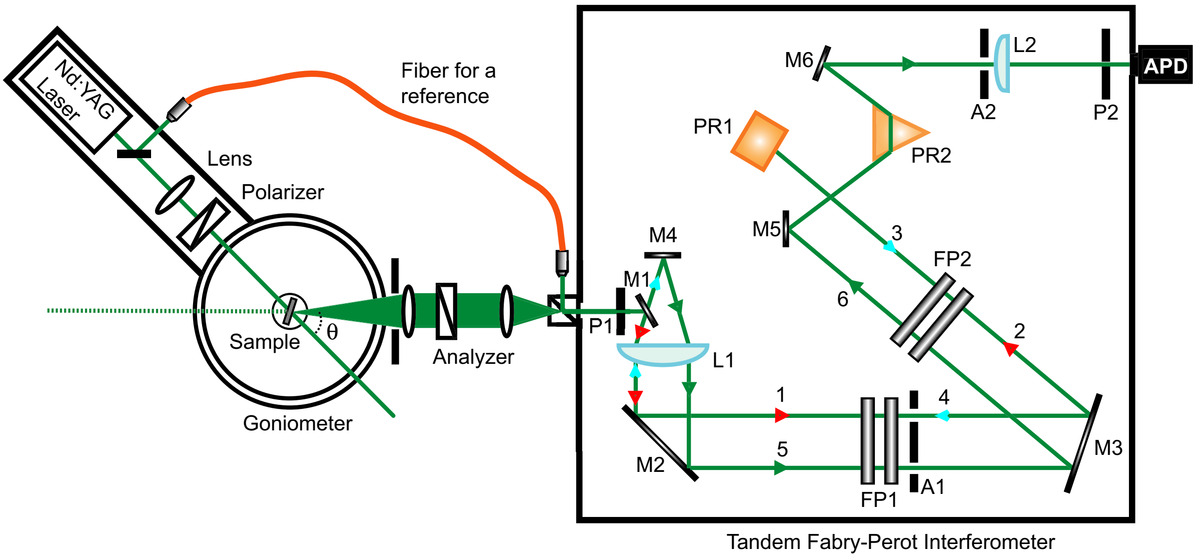
Nd:YAG
Laser
Fiber for a
reference
Lens
Polarizer
Sample
θ
Goniometer
Analyzer
P1
M1
M4
L1
M2
M5
M6
PR1
PR2
L2
A2
P2
APD
3
FP2
6
2
1
4
5
FP1
A1
M3
Tandem Fabry-Perot Interferometer

Figure 2.7.: Schematic of the Brillouin light scattering experiment setup.

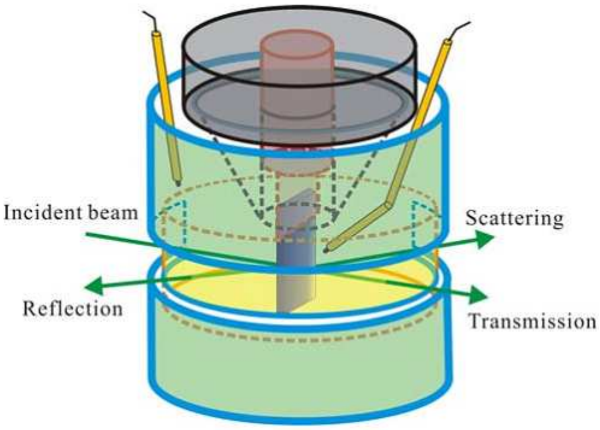
Incident beam
Scattering
Reflection
Transmission

Figure 2.8.: The sample holder allowing for BLS measurements under varying degrees of temperature.

combinations is expressed as

$$\delta\epsilon_{VV}(\mathbf{q},t) = \delta\epsilon_{yy}(\mathbf{q},t) \tag{2.53}$$

$$\delta\epsilon_{VH}(\mathbf{q},t) = \delta\epsilon_{xy}(\mathbf{q},t)\sin\frac{\theta}{2} - \delta\epsilon_{yz}(\mathbf{q},t)\cos\frac{\theta}{2} \tag{2.54}$$

Since the plane of polarization of the incident light is not rotatory upon a scattering event, polarized (VV) Brillouin scattering reveals the longitudinal acoustic (LA) mode. On the other hand, the plane of polarization of incident light is rotatory upon a scattering event so that depolarized (VH) Brillouin scattering reveals the transverse acoustic (TA) mode.

2.3.2. Scattering geometry

Selection of the scattering geometry determines the direction of elastic wave propagation. This is also a very important parameter for BLS measurements as well as the polarization of incident and scattered light. The scattering geometry can be divided into two categories defined by the direction of the incident and the scattered light as shown in Fig. 2.9. The *in-plane* phononic properties can be measured in the transmission geometry (Fig. 2.9(a)), while the *out-of-plane* phononic properties can be measured in the reflection geometry (Fig. 2.9(b)). Since two dimensional nanocomposite materials are investigated in this thesis, using both geometries is very useful to obtain information on phononic anisotropies. Therefore, most experiments described in this thesis were done in both transmission and reflection geometry.

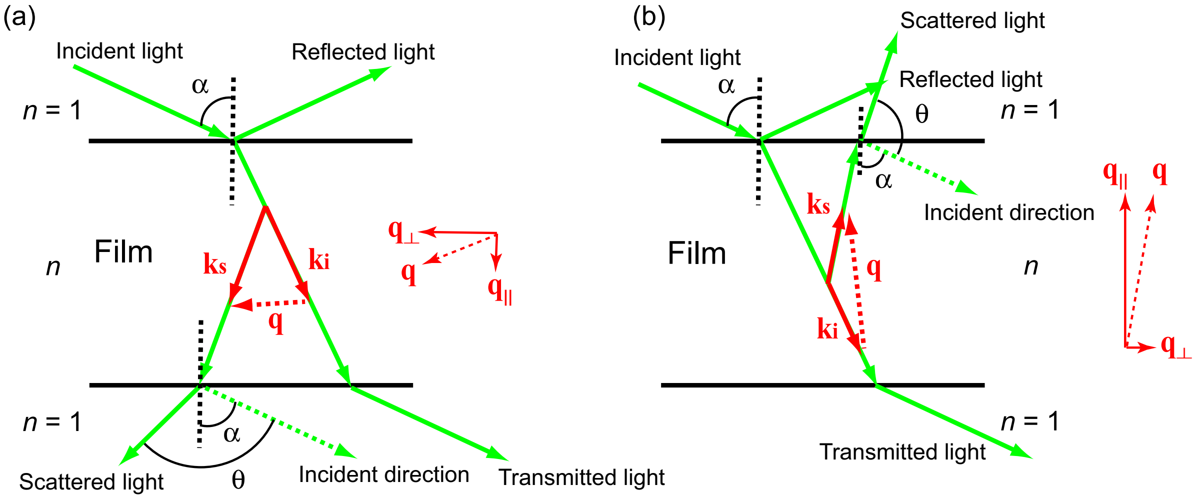
(a)
Incident light
Reflected light
α
n = 1
Film
n
ks
ki
q
q⊥
q
q||
n = 1
α
θ
Scattered light
Incident direction
Transmitted light
(b)
Scattered light
Incident light
Reflected light
α
θ
n = 1
α
Incident direction
q||
q
ks
q
ki
Film
n
q⊥
Transmitted light
n = 1

Figure 2.9.: Schematics of scattering geometry: (a) transmission geometry and (b) reflection geometry.

Figure 2.9(a) shows the transmission geometry. The scattering wavevector $\mathbf{q}$ is inclined relative to the *in-plane* direction of the film. As described in subsection 2.2.1, the scattering wavevector $\mathbf{q}$ is determined by the incident and scattered light in the film. By performing trigonometric operations and applying Snell's law, the scattering wavevector can be expressed as

$$q = \frac{4\pi n}{\lambda} \sin \left[\frac{1}{2} \left\{ \sin^{-1} \left(\frac{1}{n} \sin \alpha \right) - \sin^{-1} \left\{ \frac{1}{n} \sin(\theta - \alpha) \right\} \right\} \right] \tag{2.55}$$

$$\begin{aligned} q_\perp = \frac{4\pi n}{\lambda} \sin & \left[\frac{1}{2} \left\{ \sin^{-1} \left(\frac{1}{n} \sin \alpha \right) + \sin^{-1} \left\{ \frac{1}{n} \sin(\theta - \alpha) \right\} \right\} \right] \\ \times \cos & \left[\frac{1}{2} \left\{ \sin^{-1} \left(\frac{1}{n} \sin \alpha \right) - \sin^{-1} \left\{ \frac{1}{n} \sin(\theta - \alpha) \right\} \right\} \right] \end{aligned} \tag{2.56}$$

where $q_\perp$ denotes the parallel component of the scattering wavevector relative to the film.[1] The unique advantage of this transmission geometry is that the scattering wave vector does not depend on the refractive index of the sample due to mutual cancellation of the refraction effects at the top and bottom interfaces of the sample. Since the ratio $q_\perp/q$ in most cases is more than 0.9, assuming that the incident angle is half of the scattering angle, i.e. $\alpha = \theta/2$, it can be shown that Equation 2.56 can be simplified as

$$q = \frac{4\pi}{\lambda} \sin \frac{\theta}{2} \tag{2.57}$$

The reflection geometry is shown in Fig. 2.9(b). Applying the same trigonometric operations and Snell's law, we can obtain

$$q = \frac{4\pi n}{\lambda} \cos \left[\frac{1}{2} \sin^{-1} \left(\frac{1}{n} \sin \alpha \right) + \frac{1}{2} \sin^{-1} \left\{ \frac{1}{n} \sin(\theta + \alpha) \right\} \right] \tag{2.58}$$

$$\begin{aligned} q_\parallel = \frac{4\pi n}{\lambda} \cos & \left[\frac{1}{2} \sin^{-1} \left(\frac{1}{n} \sin \alpha \right) + \frac{1}{2} \sin^{-1} \left\{ \frac{1}{n} \sin(\theta + \alpha) \right\} \right] \\ \times \cos & \left[\frac{1}{2} \sin^{-1} \left(\frac{1}{n} \sin \alpha \right) - \frac{1}{2} \sin^{-1} \left\{ \frac{1}{n} \sin(\theta + \alpha) \right\} \right] \end{aligned} \tag{2.59}$$

where $q_\parallel$ denotes the perpendicular component of the scattering wavevector relative to the film.[2] The detailed calculations of each scattering wavevector are described in appendix A.1.

---

[1] Although the scattering wavevector **q** is parallel to the film, the $\perp$ subscript is used for the *in-plane* phonon propagation in the sense that the scattering wavevector is perpendicular to the pores.

[2] As is the case for the transmission geometry, the $\|$ subscript is used for the *out-of-plane* phonon propagation in the sense that the scattering wavevector is parallel to the pores.

3. Anodic aluminium oxide

3.1. Introduction

Nanostructured materials play an important role for the miniaturization and the development of functional devices in the various fields such as microelectronics, optoelectronics, magnetics and sensor since they show novel and unique physical, chemical, optical and mechanical properties. Currently, much effort have been undertaken to fabricate highly ordered nanostructures over a macroscopic surface area. Highly ordered nanomaterials have the potential for tremendous impact on photonic, microfluidic and sensing devices as well as magnetic recording media. Among highly ordered nanomaterials, porous materials have attracted considerable attention, and have become a subject of intense scientific interest. Especially, the research attention has been focused on the electrochemical formation of self-ordered nanoporous structures produced by the anodic oxidization. The anodization of aluminium describes one of the most widespread techniques for the fabrication of ordered nanostructures.

It is known that electrochemical oxidization of aluminium forms a passivation oxide film on the surface. This is so-called anodic aluminium oxide (AAO). AAO has been widely used to increase corrosion resistance and wear resistance. The early experimentations on the formation and structural feature of anodic coatings on aluminium have been performed by Keller *et al.*[67, 68] They have revealed that AAO consists of close-packed hexagonal arrays of cylindrical pores using optical and electron microscopes (Fig. 3.1). Moreover, they demonstrated the relationship between an applied voltage and the geometric features of AAO structures such as the pore size and the interpore distance. Subsequently, Wood *et al.*[69–72] conducted further detailed research on the AAO film morphology, composition and structure on the basis of transmission electron microscopy (TEM) and magic angle spinning-nuclear magnetic resonance (MAS-NMR) studies.

Although the reformation of porous structures such as pore diameter and pore shape was reported, an in-depth study on the regularity of nanopore array had been unexplored until Masuda *et al.*[73, 74] reported that notable regularity of nanopore arrangement can be achievable with a two-step anodization procedure. They succeeded in the fabrication of long-ranged-ordered monodomain porous structure by introducing the hexagonally ordered array of concave aluminium surface features of the oxidation front after a long first anodization step, which guides the development of nanopores at the initial stage of a second anodization step.[75, 76] This allows for the self-ordered formation of quasi-monodomain porous structures with a narrow size pore distribution.

AAO has a much broader range of applications including template synthesis, nanopattern-

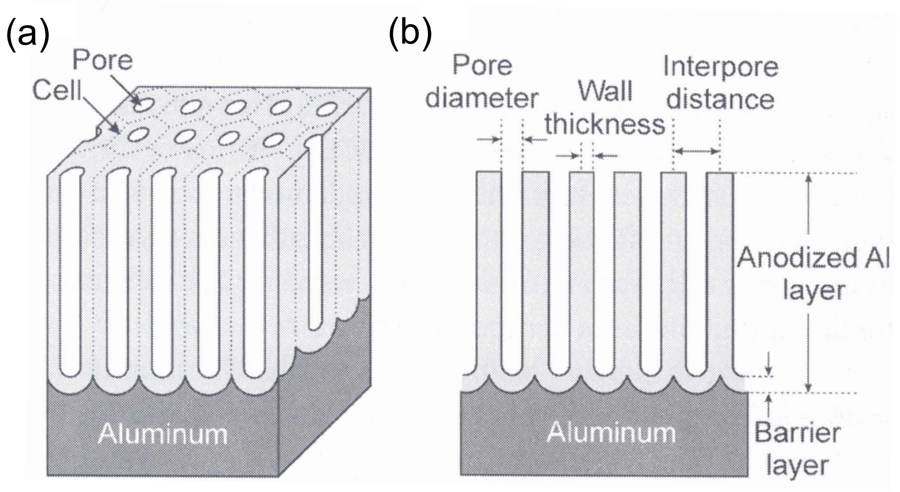

Figure 3.1.: Schematic of (a) idealized structure of anodic aluminium oxide and (b) a cross sectional view of the anodized layer. (Adapted from Ref. [131])

ing methods and sensing devices. Especially, AAO has been widely used as shape-defining molds for the synthesis of one-dimensional nanostructures.[77–79] On the other hand, templating methods employing AAO have been also commonly used for the fabrication of high-density, ordered array of nanodots, nanotubes and nanowires on a very broad material platform such as semiconductors, metals, metal oxides, and carbon nanotubes.[80] Recently, the fabrication of regular nanopatterns has extended to a high-density patterning of DNA using a Au disk array formed from AAO.[81, 82] In addition, a flow-through-type DNA array, fabricated by immobilizing a single-stranded probe DNA to the side walls of AAO, has been demonstrated.[83] Such materials offer promising prospects to develop highly functional biodevices for DNA sequences, clinical applications and diagnostics. Moreover, the potential of a monodomain AAO lies in the filed of nanophotonics. For instance, a monodomain AAO can be employed as a two-dimensional photonic crystal, which prohibits the propagation of specific wavelengths of light due to a photonic band gap. Several reports appeared in the literature describing 2D photonic crystals based on AAO.[84–90]

3.2. Pore formation mechanism

A typical current-density time transient recorded during the anodization of aluminium is shown in Fig. 3.2. When a constant voltage is applied for porous alumina growth, the current density decreases with time until the local minimum is reached, and then increases gradually to the steady-state-forming current density. During the initial period of anodization (Fig. 3.2, regime (i)), the decrease in current density is associated with a growth of high-resistance oxide film (barrier layer) on aluminium. Further anodizing (regime (ii)) results in the propagation of individual paths (pore precursors) through the barrier layer. At the minimum of current

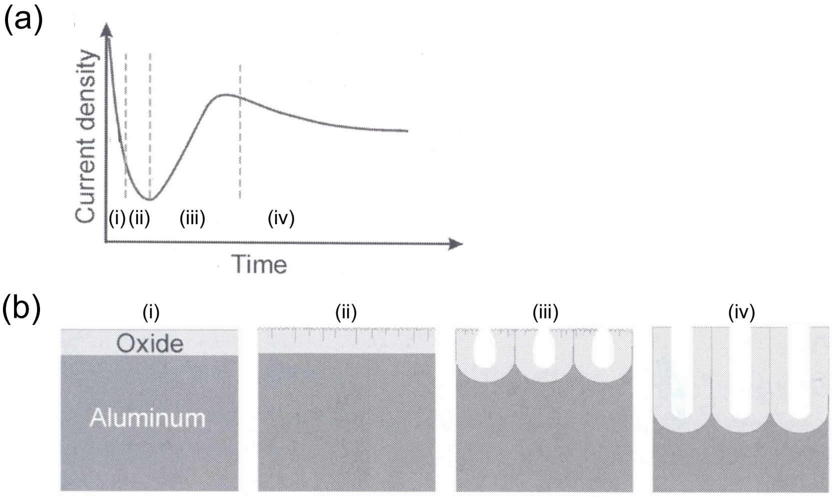

Figure 3.2.: Schematic of (a) time dependence of current density during the anodization process and (b) stages of anodized aluminium oxide layer development. (Adapted from Ref. [131])

density (regime (iii)), the breakdown of the barrier layer occurs and the porous structure begins to be build. Finally, the steady-state growth of porous alumina proceeds (regime (iv)) and a forming current density is almost unchanged. The rate of current decrease, the time at which the minimum current is observed, and the steady-state-forming current density depends directly on the anodizing conditions, such as applied anodizing potential, temperature, type of electrolyte and electrolyte concentration.

AAO is described as an amorphous structure with significant incorporations of water, which occurs in the form of hydroxide or hydrate[67, 70, 91], and the conjugate base anions dissociated from acid electrolytes[70, 71, 91–93], which can replace O^{2-} in the oxide[93]. For steady-state anodic porous film formation, the transport and reaction processes contributing to the formation of the anodic film take place at the metal-oxide interface.[70, 94, 95] The O^{2-} ions formed at the oxide-solution interface through dissociation of water migrate toward the metal surface, while the Al^{3+} ions formed at the metal-oxide interface are dissolved into solution, which are not involved in the formation of the anodic film since Al^{3+} ions are mobile in the oxide layer under the electric field[96]. The transport processes can be related to stress gradients and the electric field. Li *et al.*[97] reported that the volume expansion factor of the aluminium during anodization, which is the ratio of the grown alumina layer thickness to the consumed aluminium layer thickness, is about 1.4 that is independent of the electrolyte. Since the oxidation takes place at the entire metal-oxide interface, the materials can only be expanded in the vertical direction, and consequently the existing pore walls are moved upwards[96]. In addition, the volume expansion of the aluminium has an intimate involvement in the mechanical stress which causes the repulsive forces between neighboring pores. Therefore, the volume expansion plays an important roll to promote the formation of large domain of hexagonally ordered pores during the anodization process.

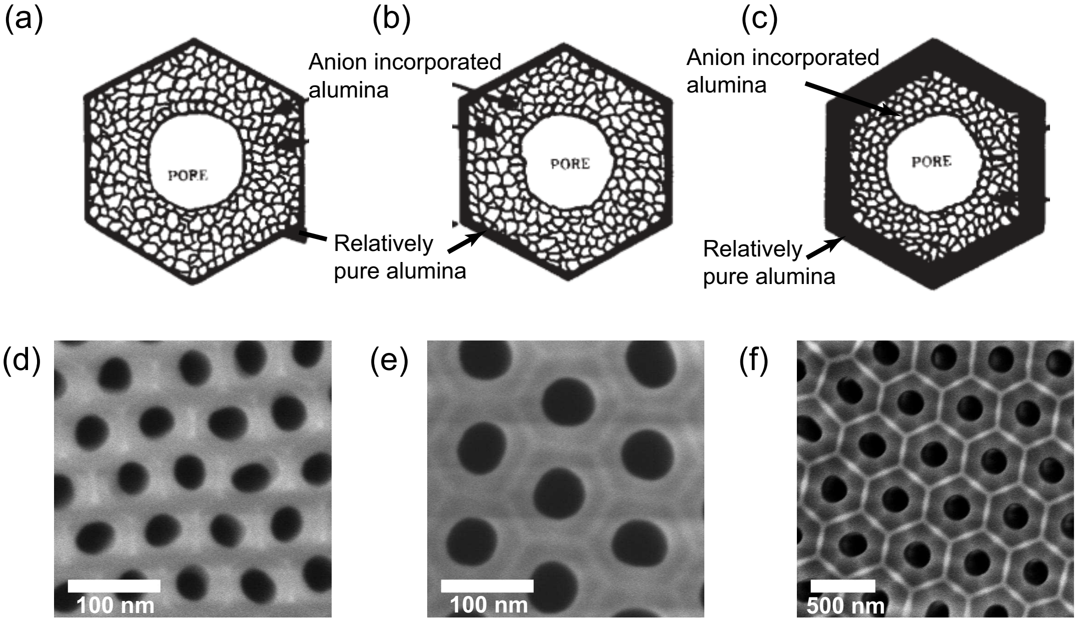

Figure 3.3.: Schematic representations of the top views of porous alumina cell-wall structures prepared in (a) sulfuric, (b) oxalic and (c) phosphoric acid. (Adapted from Ref. [32]) (d)-(f) Corresponding scanning electron microscope (SEM) images.

Recently, a mechanism of anodic porous alumina layer growth has been investigated using tungsten tracers to visualize details of the flow of anodic oxide within pore walls.[98–100] The aluminium layer, with incorporated 5 nm tungsten layer, was sputtered onto electropolished aluminium substrates. The entry tungsten layer to the anodic oxide and its consequent motion was observed by transmission electron microscopy (TEM). The measurements revealed that the anodic oxide layer is moved upward in the pore walls indicated by a mechanical stress model. Furthermore, Houser and Hebert presented a model for steady-state growth mechanism of anodic porous alumina, incorporating metal and oxygen ion transport and viscous flow.[101, 102] They confirmed that the hypothesis of the viscous flow model through comparison to detailed observations of the movement of tungsten tracers in the pore walls. Also, they suggest that the self-ordering of porous alumina could be explained by metal-oxide interface motion regulated by the combination of ionic migration in the anodic oxide and stress-driven interface diffusion of metal atoms.

The properties of AAO formed by anodization are connected to the nature of the acid electrolyte. The amount of anion incorporation as well as the wall thickness depend on the anodization conditions such as anodization potential and temperature. Figure 3.3 shows both schematic representations of cell walls and actual AAO prepared in each acid electrolyte. As seen in Fig. 3.3(d)-(f), the wall thickness increases in the order: $H_2SO_4 \leq H_2C_2O_4 \leq H_3PO_4$. This is in good agreement with the previous work[92]. Furthermore, inhomogeneities of the dielectric constant and density within the film are expected due to the nonuniform distribution

Table 3.1.: Possible alumina minerals with the different refractive indices and densities.

Name	Composition	Refractive index	Density (kg/m^3)
Wavelite	$Al_3(OH)_3(PO_4)_2 \cdot 5H_2O$	n_α=1.527, $n_\beta = 1.535$, n_γ=1.553	2360
Augelite	$Al_2(PO_4)(OH)_3$	n_α=1.574, n_β=1.576, n_γ=1.588	2700
Gibbsite	α-$Al(OH)_3$	n_α=1.57, n_β=1.57, n_γ=1.59	2420
Diaspore	β-AlO(OH)	n_α=1.694, n_β=1.715, n_γ=1.741	3400
Boehmite	α-AlO(OH)	n_α=1.64, n_β=1.65, n_γ=1.66	3440
Corundum	α-Al_2O_3	n_α=1.761, n_β=1.769	3970

of anions in the anodic oxide layer. Several possible alumina minerals with different refractive indices and densities are shown in Table 3.1[103].

3.3. Self-ordered anodic aluminum oxide

3.3.1. anodization setup

Figure 3.4 shows the anodization setup. The customized electrochemical cell consists of a two-electrode system, i.e., the Platinum mesh (Goodfellow, 99.9%, wire diameter = 60 μm, mesh aperture = 250 μm, size = 50$\times$50 mm^2) acting as a counter electrode and aluminum disks (Goodfellow, 99.999%, diameter = 20 mm, thickness = 500 μm) acting as a working electrode. To stir acid electrolytes vigorously, a mechanical stirrer (IKA) was used. The apparatus was operated by a computer, using a customized program. A thermostat (Haake Thermostat F6-C25), which was connected to a cooling stage and which circulated ethylene glycol, was used to control the temperature of the acid electrolyte. The high-voltage DC power supply (Agilent N5771A) has a working range of 0 to 300 V. The current was measured with a multimeter (Keithley).

3.3.2. Two-step anodization

Self-ordered AAO films were prepared in accordance with the precedent.[73, 74] The formation of nanopores by self-ordered anodized aluminium is a multistep process that includes pre-treatment, anodizing and post-treatment steps as shown in Fig. 3.5. Firstly, ultrapure aluminium disks (99.999%, Goodfellow) were cleaned with acetone, isopropanol and ethanol in an ultrasonic bath for 5 min each. Then, they were electrochemically polished in a 1:4 mixture solution of perchloric acid ($HClO_4$, 60%, Fluka) and absolute ethanol at 25 V for 5 min below 10 $^\circ$C solution temperature (Fig. 3.5(a)).

After the pre-treatment, aluminium disks were anodized in an appropriate electrolyte acid solution under the conditions described in Table 3.2 for more than 20 hours (Fig. 3.5(b)). The initial pore arrangement was disordered since nanopores were randomly formed on the surface (Fig. 3.6(a)). However, self-ordered hexagonal arrangement of nanopores is formed at

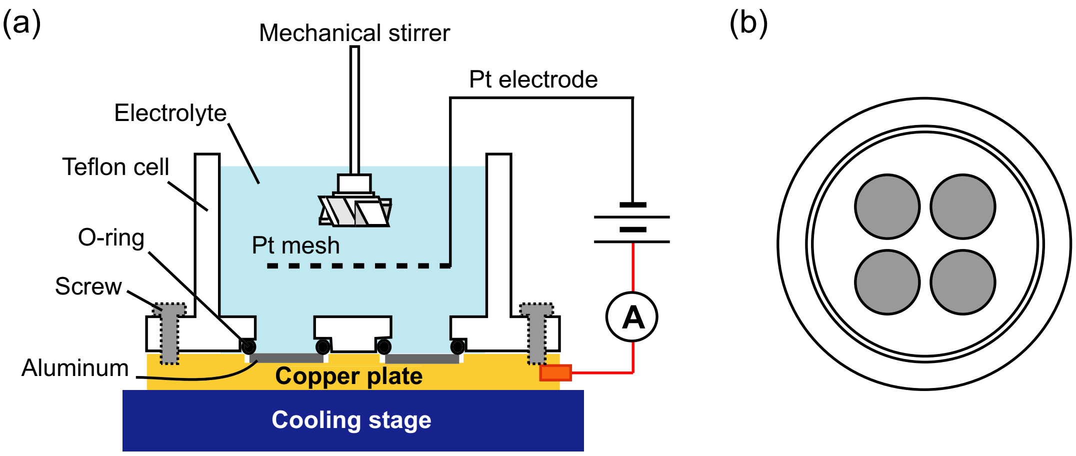

Figure 3.4.: Schematic of (a) the anodization setup and (b) top view of the anodization cell. There are four circular holes at the bottom of the cell to anodize four aluminum disks simultaneously.

Table 3.2.: Anodization conditions for each acid electrolyte

Electrolyte	Concentration (M)	Voltage (V)	Temperature (°C)	Initial diameter (nm)	Lattice constant (nm)
Sulfuric	0.3	25	1	25	65
Oxalic	0.3	40	3	35	100
Phosphoric	0.3	195	1	170	500

the bottom of the layer due to repulsion forces between neighboring pores during the anodization process (Fig. 3.6(b)). After the first anodization, chemical etching of the oxide layer was carried out in a mixed solution of 6 wt% phosphoric acid (H_3PO_4, 99%, Fulka) and 1.8 wt% chromium (VI) oxide (CrO_3, Merck) at 30 °C for 12 hours (Fig. 3.5(c)). The hexagonal pattern of concave maintained on the aluminium surface then acted as a self-assembled mask for a second anodization. The second anodization was conducted under the same condition as the first anodization step (Fig. 3.5(d)). The underlying aluminium substrate was etched with a mixture of 1.7 g copper (II) chloride ($CuCl_2{\cdot}H_2O$, 99%, ACROS), 50 mL concentrated hydrochloric acid (HCl, 37%, VWR) and 50 mL deionized water (Fig. 3.5(e)). The bottoms of the nanopores in the remaining AAO were opened by etching with 10 wt.% H_3PO_4 (Fig. 3.5(f)). To tailor the porosity, the initial diameters were widened by isotropic etching in 0.3 M oxalic acid at 30 °C.

Figure 3.6(c) shows a scanning electron microscope (SEM) image of the top view of the AAO after the second anodization. The hexagonal nanopore arrangement was observed over relatively large domains, which were separated from neighboring domains with a different lattice orientation by domain boundaries. Figure 3.6(d) shows a cross sectional view SEM

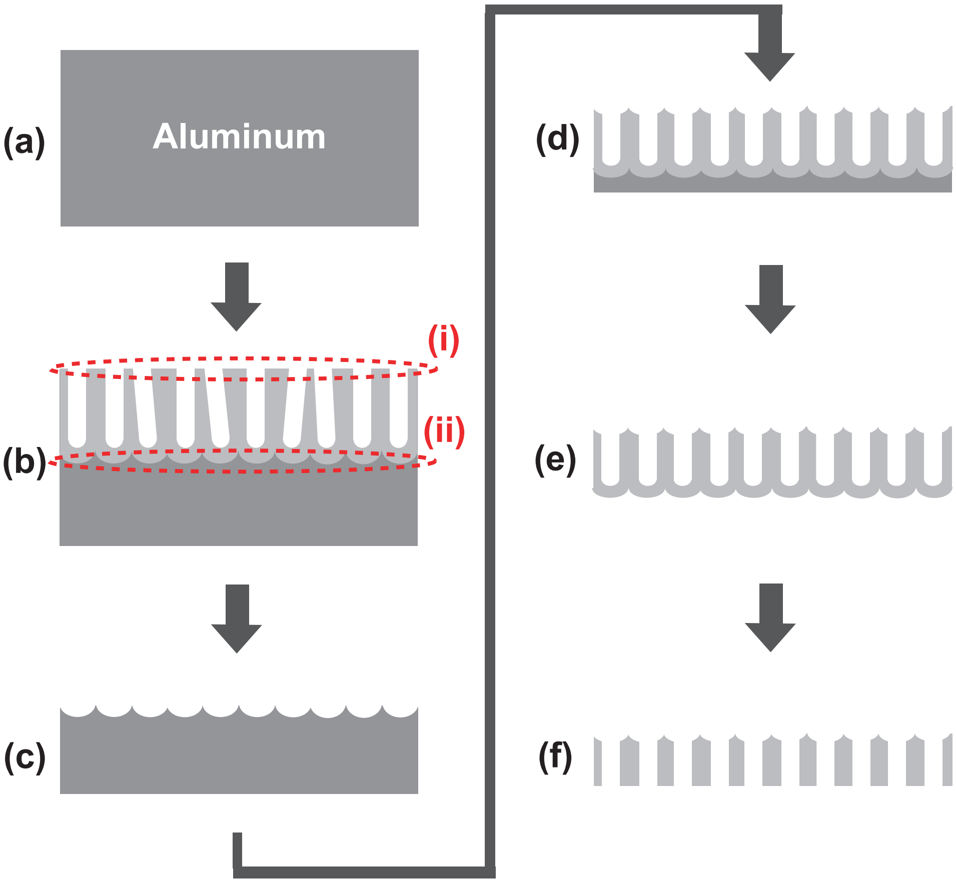

Figure 3.5.: Schematic of the nanopores formation. (a) Electropolishing, (b) first anodization, (c) removal of the formed oxide layer, (d) second anodization, (e) removal of aluminum layer, (f) removal of barrier layer.

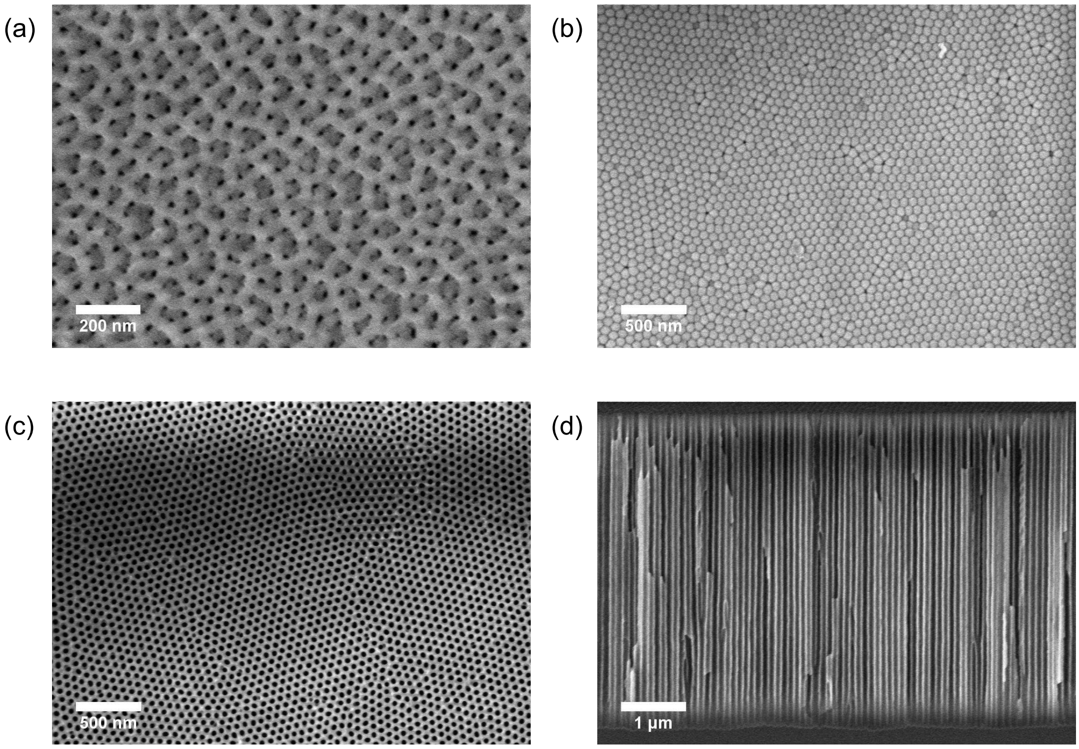

Figure 3.6.: Scanning electron microscope (SEM) images of nanoporous anodic aluminum oxide prepared in 0.3 M sulfuric acid at 25 V. (a) the top view and (b) the bottom view of the membrane after removing Al selectively, which are described as (i) and (ii) in Fig. 3.5, respectively. (c) the top view of the membrane after the second anodization. (d) Cross sectional image of the AAO scaffold.

image of the hole array.[1] The growth of straight parallel channels perpendicular to the substrate is confirmed by Fig. 3.6(d).

Figure 3.7 shows an exemplary experimental current-time transient recorded during both the first and second anodization at a constant voltage of 40 V in 0.3 M oxalic acid at 3 °C solution temperature. The black solid line and red dashed line represent the fist and second anodization curve, respectively. The current minimum is higher for the second anodization than for the first anodization. Since a constant voltage was applied for the preparation of anodized nanoporous aluminium oxide, the resistance for the second anodization is lower than that for the first anodization. This can be attributed to the fact that a thinner alumina oxide layer was probably formed at the pore bottoms of each concave feature (Fig. 3.5(c)) than at a flat aluminium surface (Fig. 3.5(a)). Therefore, pore nucleation was easier on the hexagonally molded surface, leading to a lower barrier layer growth rate. In addition to a constant voltage regime, Li *et al.*[93] demonstrated anodic porous alumina formation at a constant current

---

[1] This sample was prepared at 40 V in 0.3 M oxalic acid at 3 °C. The acid electrolyte used for the preparation is different from the ones described in Fig. 3.6(a), (b) and (c).

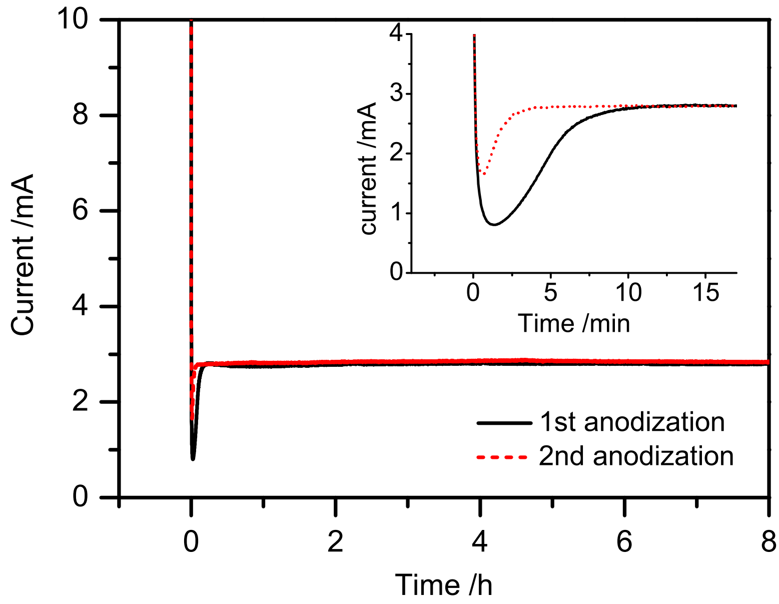

Figure 3.7.: Current-time curves of anodizing at 40 V in 0.3 M oxalic acid at 3 °C. Inset shows a zoomed area of minimum region.

regime, and observed a slightly slower voltage increment for the molded aluminium surface than that for the flat aluminium surface. They concluded that the thinnest oxide layer might be formed on the molded surface, where the resistance is lowest and electric field is the highest, thus promoting the formation of the pores.

3.3.3. Pre-molding anodization

Since its introduction[75], molding-guided anodizations based on pre-texturing of aluminium have been used for the fabrication of AAO with an ideally ordered channel arrangement. Among pre-molding anodization methods, a direct nanoindentation on the aluminium surface with an atomic force microscope (AFM) tip[104], focused-ion beam lithography[105–107] and holographic lithography[108] have been employed to form the hexagonal pattern on the aluminium surface. In direct patterning, despite of the capability of individual indentation of each sample, the technique is consequently time-consuming and limited applications at the laboratory scale. Therefore, the imprinting lithography with a master stamp (mold) is the most widespread method used for prepatterning of aluminium.[75, 76, 109–120] Stamps with an arranged array of convex features are usually prepared lithographically, and can be used several times for the pre-texturing of aluminium. The mold used for nanoindentation of aluminium can be made from SiC[75, 76, 109–114], Si_3N_4[115–117], Ni[118, 119] and poly(dimethylsiloxane)[120]. The imprinting of aluminium using a master stamp and fabrication of anodic porous alumina from

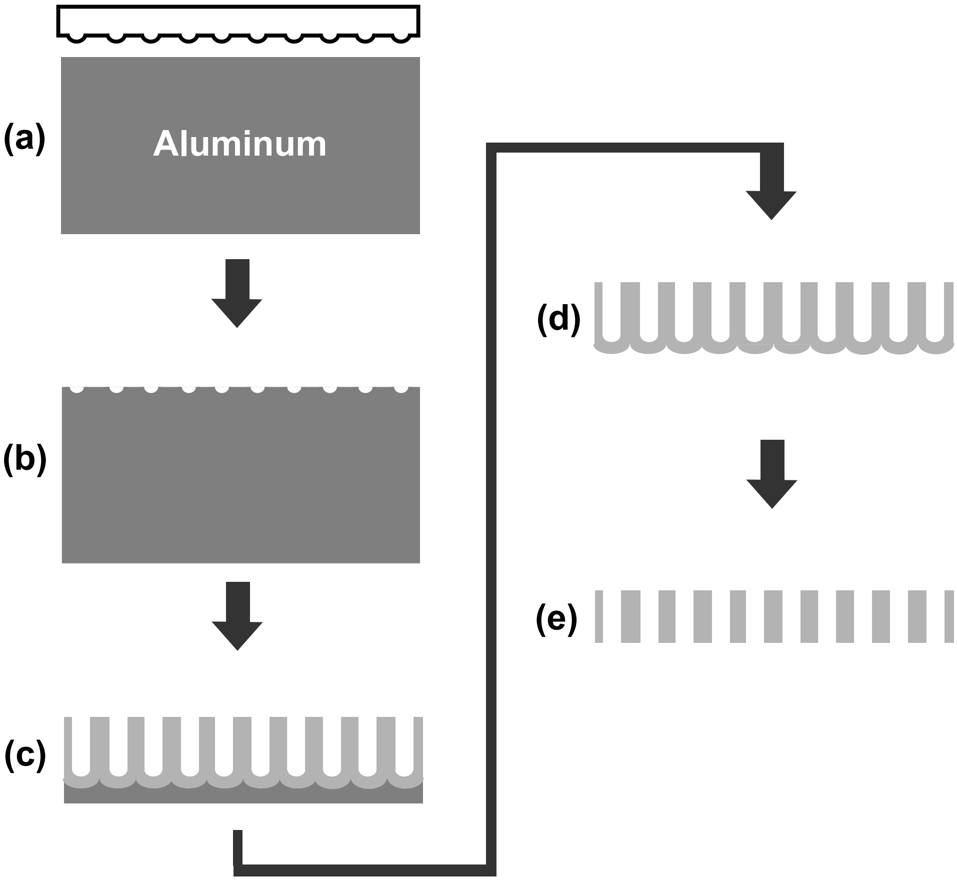

Figure 3.8.: Schematic of the nanopores formation. (a) Electropolishing, (b) first anodization, (c) removal of the formed oxide layer, (d) second anodization, (e) removal of aluminum layer, (f) removal of barrier layer.

prepatterned aluminium is illustrated in Fig. 3.8.

Ideally ordered AAO was prepared in accordance with the precedent[84, 85, 90]. Firstly, ultra-pure aluminium sheets were cleaned with acetone in an ultrasonic bath for 1 min. Then, they were electrochemically polished in a 1:4 mixture solution of ethanol and $HClO_4$ at a constant current density of 2 mA/cm^2 for 4 min at 0 °C solution temperature. Then, a master mold was placed on an aluminium sheet and pressed with an oil press (Fig. 3.8(a)). This process generated an array of concave features on the surface of the aluminium (Fig. 3.8(b)).

After the pre-treatment, aluminium sheets were anodized in either oxalic acid or phosphoric acid under the conditions described in Table 3.3 for 5 hours (Fig. 3.8(c)). After the anodization, the underlying aluminium substrate was etched with a mixture of 1.7 g $CuCl_2 \cdot H_2O$, 50 mL concentrated HCl and 50 mL deionized water (Fig. 3.8(d)). The bottoms of the nanopores in the remaining AAO were opened by etching with 10wt% phosphoric acid at 30 °C (Fig. 3.8(e)). To tailor the porosity, the initial diameters were widened by isotropic etching in 10wt% phosphoric acid at 30 °C.

Table 3.3.: Anodization conditions for each acid electrolyte

Electrolyte	Concentration (M)	Voltage (V)	Temperature (°C)	Lattice constant (nm)
Oxalic	0.05	80	0	200
Phosphoric	0.1	200	0	500

Figure 3.9 shows a SEM image of the top view of anodized porous alumina after widening the nanopores in 10wt% at 30 °C for 60 min. It reveals that the well-ordered hexagonal arrangement has a monodomain periodicity of 200 nm over a large area.

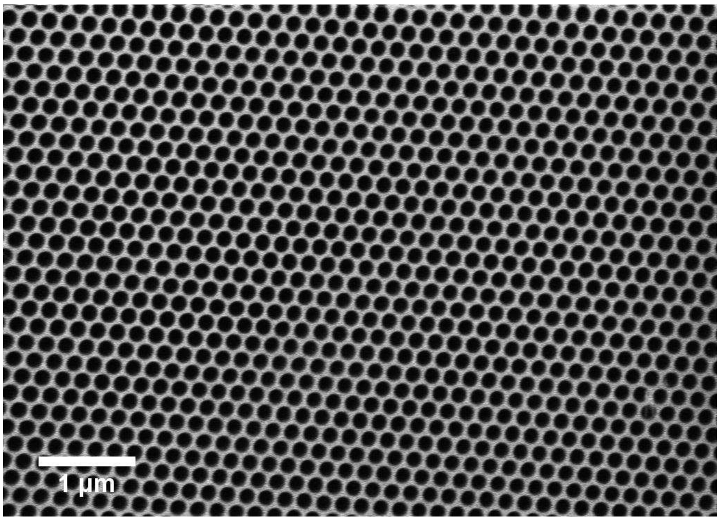

Figure 3.9.: Scanning electron microscope (SEM) image of nanoporous anodic aluminum oxide prepared in 0.3 M oxalic acid at 80 V.

4. Anisotropic propagation and confinement of high frequency phonons

4.1. Introduction

Phononic materials exhibiting periodic variations in their density and elastic properties can modify the propagation of sound waves[27, 28, 121–125], and band gaps prohibiting sound propagation for specific Bragg frequencies or wavelengths commensurate with their lattice constant may occur[9, 15, 24, 25, 42, 43, 45, 126]. Their design involves engineering of both the band gap region and the directional flow of elastic energy outside the band gap[28, 122–124]. We show that self-ordered anodic aluminium oxide (AAO)[73, 74] containing aligned cylindrical nanopores with pore diameters of a few tens of nm and pore depths up to several 100 μm is a promising material platform for the still-challenging manipulation of sound propagation in the hypersonic (GHz frequency) range. AAO, which is widely used as a shape-defining mould in the synthesis of 1D nanostructures[78, 79, 127], can be infiltrated with a broad range of fluids, thus yielding customized composite systems with high elastic contrast. Their tailor-made acoustic properties embracing their anisotropic elastic properties parallel and perpendicular to the pore axes and phonon localization were explored by high resolution Brillouin spectroscopy. The rational manipulation of the phononic density of states in the hypersonic range may yield customized membrane configurations for tunable filters, heat management systems and sensors and could pave the way for the application of concepts for phononic metamaterials[128] and acoustic cloaking systems[51] to the hypersonic range.

The phononic band diagram of periodic composite media can be engineered by the solid or liquid nature of the components, the contrast between their densities and elastic constants, their volume fractions, as well as by the symmetry and morphology of the lattice they constitute. Up to now, research has predominantly been focused on the search of absolute band gaps in solid/solid, solid/fluid and drilled holes structures with lattice constants in the millimeter range. Typical examples of this are steel, lead or carbon cylinders in epoxy matrix[25], steel cylinders in water[129] as well as solid materials containing cylindrical air holes[12], whereas configurations based on arrays of aligned cylindrical channels filled with liquids in a rigid matrix have remained essentially unexplored[130].Only few attempts to adapt concepts for functional phononic bandgap structures to the GHz frequency range have been reported[42, 43, 45, 126], despite the potential of such systems for a plethora of applications[121, 128]. A peculiar advantage of hypersonic phononic systems is the possibility to engineer interactions between phonons and visible wavelength photons, thus enabling the design of miniaturized acousto-optical devices.

AAO prepared by anodization of aluminium with oxalic acid[73] as an electrolyte is a readily available, nanostructured scaffold containing hexagonal arrays of aligned nanopores with pore diameters *d* ranging from 35 nm to 85 nm, a lattice constant of 100 nm and porosities $p = \pi d^2/(2\sqrt{3}a^2)$ ranging from 10% to 65% which can be varied independently within certain limitations. It is astounding that AAO has, up to now, not been explored as a material platform for the engineering of sound propagation in the GHz frequency range, despite its advantages: i) the well-defined geometry of AAO is likely associated with pronounced anisotropic behavior; ii) its pore depths can be adjusted to any value from about 1 μm up to several 100 μm; iii) its lattice parameters perfectly match the requirements for the engineering of sound propagation in the hypersonic range; iv) its exceptionally high longitudinal (c_l = 7300 m/s) and transverse (c_t = 3750 m/s) sound velocities (see below) as compared to air (c_l = 340 m/s) or soft materials deposited into the nanopores ($c_l \sim$1500 m/s), result in composites with a large elastic contrast between their constituents. It is reasonable to assume that the proper selection of the materials deposited into the nanopores and control over mesoscopic structure formation processes they may undergo under the 2D- confinement thus imposed[79, 127] allow engineering the phononic density of states and consequently of the high-frequency acoustic properties in AAO-based hypersonic systems.

4.2. Experimental

4.2.1. Materials

As described in Chapter 3, self-ordered AAO was prepared following Masuda's two-step anodization process[73, 74]. Ultrapure aluminum substrates (99.999%, *d* = 20 mm, thickness = 500 μm, Goodfellow GmbH) were anodized in 0.3 M oxalic acid at 40 V. Anodization in oxalic acid yielded AAO with a lattice constant of about 100 nm. To tailor the porosity, the pores with initial diameter of 35 nm were widened by isotropic etching in 0.3 M oxalic acid at 30°C. The resulting pore diameters were 35, 60 and 85 nm, respectively, which were revealed with SEM images of the top view of the AAO as shown in Fig. 4.1. Then, poly(dimethylsiloxane) (PDMS, M_w = 1350 g/mol, M_n = 980) was infiltrated into the AAO at room temperature.

4.2.2. Brillouin spectroscopy

Brillouin light scattering (BLS) is based on inelastic scattering of the incident laser beam by thermally excited phonons propagating through a medium along specific directions determined by the scattering geometry.[131] Figure 4.2 shows two different scattering geometries. In these two configurations the phonon propagation is probed perpendicular ("*in-plane*") and parallel ("*out-of-plane*") to the nanopores of the native AAO. In the transmission geometry

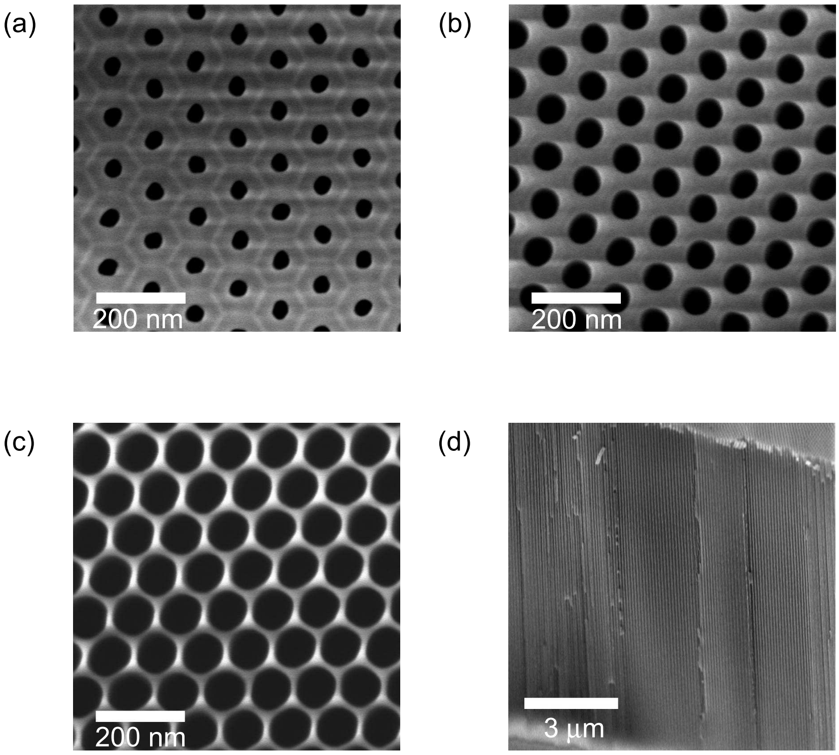

Figure 4.1.: Scanning electron microscope (SEM) images of native AAO. (a), (b), (c), Top views. (a) porosity p = 11%, (b) p = 32%, (c) p = 65% for lattice constant a = 100 nm. (d) Cross sectional image of the AAO scaffold seen in (b).

(Fig. 4.2(a)), the external scattering angle θ is twice the incident angle α and the scattering wave vector $\mathbf{q} = \mathbf{k}_s - \mathbf{k}_i$ defined by the wave vector of the scattered ($\mathbf{k}_s$) and incident ($\mathbf{k}_i$) photons has the same amplitude $q_\perp = (4\pi/\lambda)\sin(\theta/2)$, which depends only on θ and the wavelength λ of the incident laser beam but not on the refractive index of the medium. In the reflection geometry (Fig 4.2(b)), $\mathbf{q}$ lies parallel to the nanopores for $\theta = 2\alpha$ and its magnitude $q_\parallel = (4\pi n/\lambda)\sin(\alpha)$ depends now on the refractive index n. Because of the optical contrast between native AAO and air, the lowest accessible $\mathbf{q}_\perp$ is limited to about 0.03 nm^{-1}. The elastic (acoustic) properties of the native AAO are distinct along these two directions in overall agreement with the theoretical predictions.

Since AAO is a porous material, it is necessary to consider the effective refractive index n_{eff}. The Maxwell-Garnett theory[132] was used to calculate effective refractive indices for "*in-plane*" and "*out-of-plane*". Assuming $\epsilon = n^2$, the effective dielectric constant can be expressed as

$$\frac{\epsilon_{eff} - \epsilon_{alumina}}{\epsilon_{eff} + 2\epsilon_{alumina}} = f \times \frac{\epsilon_{pore} - \epsilon_{alumina}}{\epsilon_{pore} + 2\epsilon_{alumina}} \tag{4.1}$$

$$\epsilon_{eff} = (1 - f) \cdot \epsilon_{alumina} + f \cdot \epsilon_{pore} \tag{4.2}$$

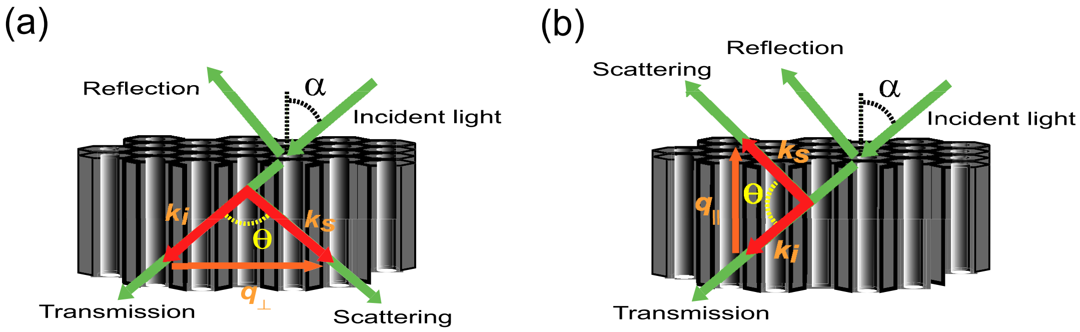

Figure 4.2.: Schematics of scattering geometry: (a) transmission geometry and (b) reflection geometry.

where ϵ_{eff}, $\epsilon_{alumina}$ and ϵ_{pore} denote the dielectric constants of the effective medium, alumina and the material contained in the nanopores, respectively. f denotes the porosity of AAO. Equation 4.1 gives the effective dielectric constant for "*in-plane*", while Equation 4.2 for "*out-of-plane*". As described above, only the scattering wave vector parallel to the pores $q_\parallel$ depends on the refractive index n. Consequently, only the effective refractive index for "*out-of-plane*" is required. As described in section 3.2, several possible alumina with different refractive indices could be considered. However, the refractive index of 1.65[133] for pure alumina was used here for simplicity. A refractive index of 1.41[134] was used for PDMS. According to SEM measurements, three sets of self-ordered AAO with porosity f = 0.11, 0.32 and 0.65 were used for this study, which yielded the effective refractive indices of 1.62, 1.57 and 1.49, respectively.

4.3. Hypersonic modes in air/AAO phononic crystals

Phonon dispersion relations can be tuned by the selection of lattice constant, lattice topology and porosity of infiltrate materials. AAO with a lattice constant of 100 nm was fabricated to investigate how porosity affects elastic wave propagations in AAO. First of all, three air-filled AAO films with different porosities of p = 11%, 32% and 65% were examined by BLS spectroscopy.

Figure 4.3(a) shows polarized BLS spectra of AAO with a lattice constant of 100 nm and a diameter of 60 nm for the "*in-plane*" ($\mathbf{q}_\perp$) phonon propagation at six different $q_\perp$ values. Each spectrum shows a single doublet, and a peak shifted linearly as the scattering vector increased. This indicates that there existed only one longitudinal mode in air-filled AAO with a lattice constant of 100 nm and a diameter of 60 nm. Figure4.3(b) shows both polarized and depolarized BLS spectra of the same porosity AAO at $q_\perp = 0.0118\ \mathrm{nm}^{-1}$.

A more complete knowledge of the phonon propagation can be obtained by referring to the measured dispersion relation $\omega(\mathbf{q})$ as shown in Fig. 4.4 in the case of the "*in-plane*" phonon propagation with longitudinal and transverse polarization and the "*out-of-plane*" phonon prop-

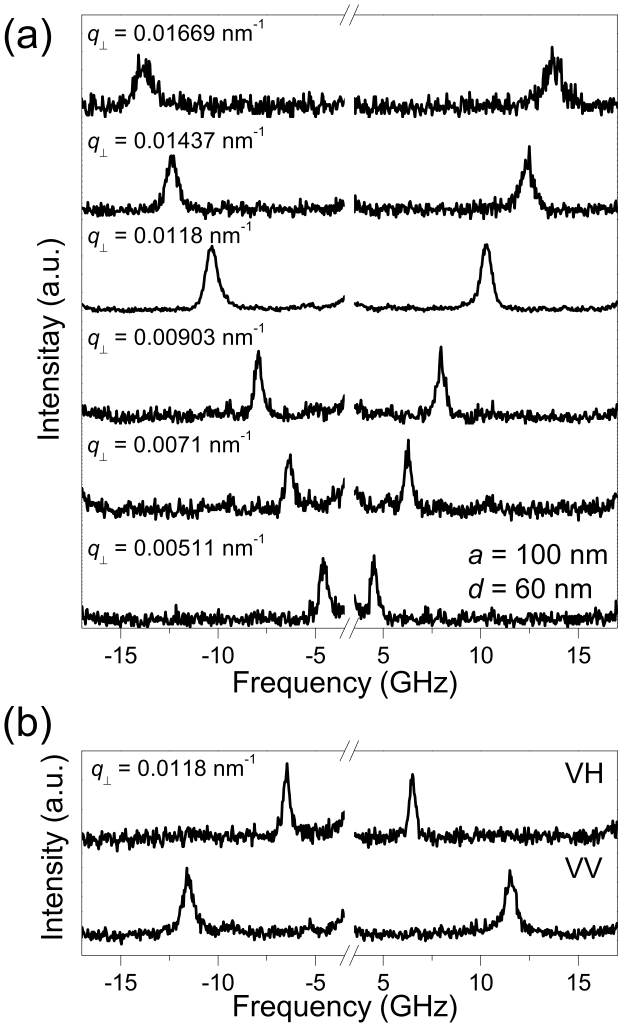

Figure 4.3.: (a) A series of polarized BLS spectra for AAO with a lattice constant of 100 nm and a diameter of 60 nm for the "*in-plane*" ($\mathbf{q}_\perp$) phonon propagation. (b) Both polarized and depolarized spectra at $q_\perp$ = 0.0118 nm^{-1}.

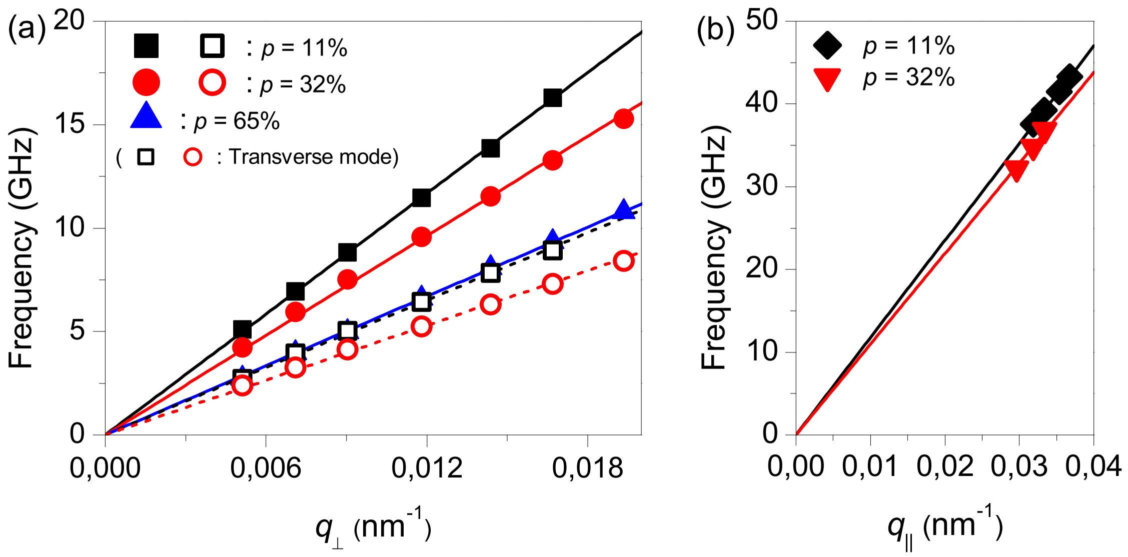

Figure 4.4.: Dispersion relations of both (a) "*in-plane*" ($\mathbf{q}_\perp$) and (b) "*out-of-plane*" ($\mathbf{q}_{||}$) longitudinal phononic modes in air-filled AAO. The black, red and blue solid lines in (a) represent the dispersion relations for air-filled AAO with p = 11%, p = 32% and p = 65%, while the corresponding dashed lines represent the effective sound velocities in corresponding AAO scaffolds.

Table 4.1.: Experimental effective medium velocities in air-filled AAO.

	in-plane (m/s)		*out-of-plane* (m/s)
air-filled AAO	Longitudinal	Transverse	Longitudinal
$p = 11\%$	6120	3410	7380
$p = 32\%$	5040	2770	6880
$p = 65\%$	3510		

agation with longitudinal polarization in air-filled AAO. In Figure 4.4(a), the solid lines indicate the longitudinal acoustic phonon propagation in air-filled AAO with three different porosities, while the dashed lines indicate the transverse acoustic phonon propagation. The slope of solid lines yields the longitudinal sound velocity ($c_l = \omega/q_\perp$) in the effective composite medium; c_l within 1% amounted to 6120 m/s, 5040 m/s and 3510 m/s respectively for 11%, 32% and 65% porosities. The slope of dashed lines yields the transverse sound velocity, which amounted to 3410 m/s and 2770 m/s, respectively for 11% and 32% porosities. These values lie between the sound velocities in pure alumina and bulk PDMS (c_{lPDMS} = 1050±20 m/s) (Table 4.1). In Figure 4.4(b), the solid lines indicate the longitudinal acoustic phonon propagation parallel to the nanopores. The sound velocity for each porosity was found to be 7380 m/s and 6880 m/s, respectively. These effective sound velocities are summarized in Table 4.1.The effective sound velocity decreases as the porosity increases. Moreover, the "*in-plane*" transverse mode and "*out-of-plane*" longitudinal mode for 65% porosity were not observed. This might be due to a low scattering intensity.

4.4. Hypersonic modes in PDMS/AAO phononic crystals

Figure 4.5(a) shows typical BLS spectra for the "*in-plane*" wave propagation in AAO (p = 65%) containing PDMS for $q_\perp$ and Fig. 4.5(b) presents BLS spectra for the "*out-of-plane*" phonon propagation in AAO with three different porosities at a similar $q_{||}$ value. At low $q_\perp$, the spectra seen in Fig. 4.5(a) display an effective medium behavior with a doublet at $\pm c_l q_\perp / 2\pi$, and the sound velocity c_l of the acoustic branch (***1***) is found to increase with decreasing porosity in agreement with the FDTD calculations (Table 4.3). At $q_\perp \geq 0.013\text{nm}^{-1}$, the spectra belonging to the two highest $q_\perp$'s reveal bending of branch (***1***) and remarkably, indicate the presence of a second lower-frequency branch (***2***) apparently corresponding to the interphase-sensitive branch (***2***) seen in Fig. 4.12(a). Notably, for air-filled AAO of all porosities, we observed only one longitudinal and one transverse phonon with effective medium sound velocities (Fig. 4.4) in agreement with the theoretical phonon dispersion relations in Fig. 4.12.

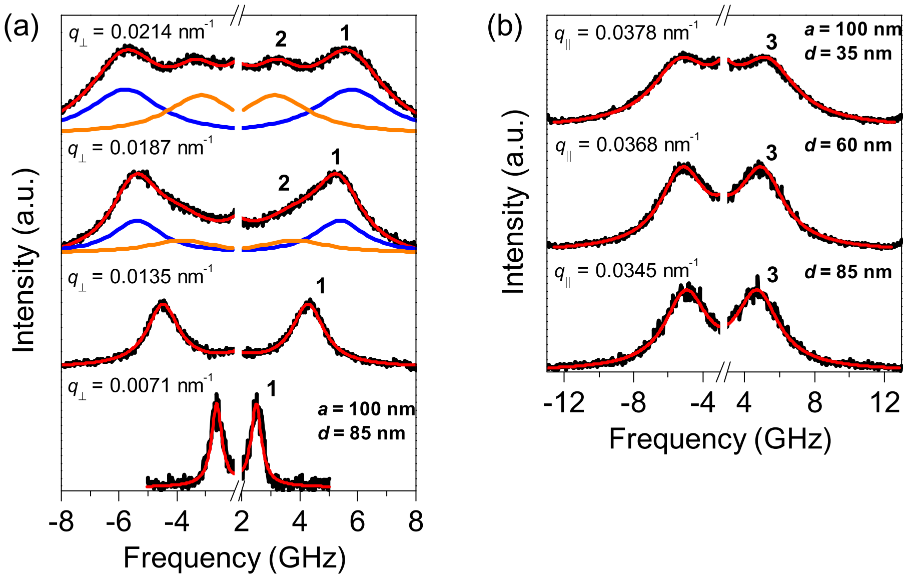

Figure 4.5.: (a) BLS spectra of AAO (p = 65%) infiltrated with PDMS at four different in-plane $\mathbf{q}_\perp$ values. (b) BLS spectra of AAO infiltrated with PDMS (p = 11%, 32% and 65%) measured at a similar out-of-plane $\mathbf{q}_{||}$ value. The BLS spectra are well reproduced by one or two Lorentzian shapes indicated by the solid lines in (a) and (b).

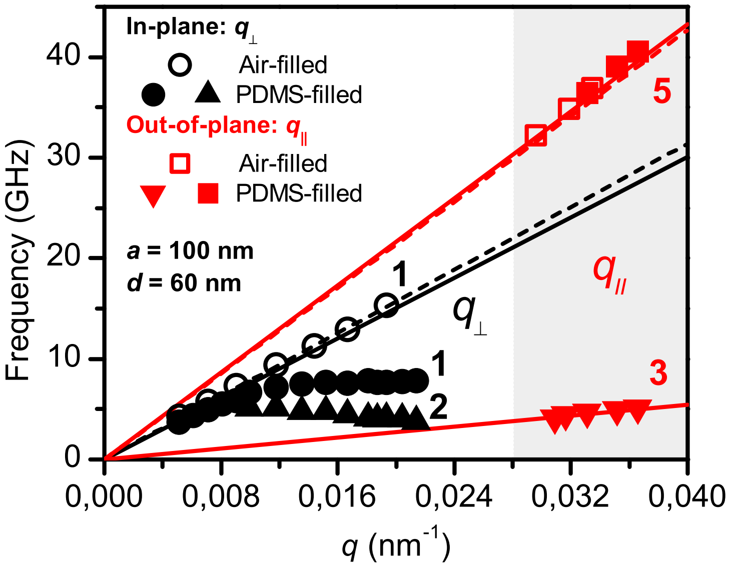

Figure 4.6.: "*In-plane*" ($\mathbf{q}_\perp$) and "*out-of-plane*" ($\mathbf{q}_\parallel$) longitudinal phononic branches (***1-3***, ***5***) in PDMS-filled AAO. The black and red dashed lines represent the dispersion relations for air-filled AAO in both "*in-plane*" and "*out-of-plane*" (data points in the light grey area) direction with 32%, while the corresponding solid lines represent the effective sound velocities in corresponding PDMS-filled AAO scaffolds.

Figure 4.6 presents exemplary dispersion curves ωw($\mathbf{q}_\perp$) in air-filled AAO (branch (***1***), solid lines) and in AAO containing PDMS (branches (***1***) and (***2***), symbols) with a porosity of 32%. In the AAO containing PDMS, c_l obtained from the linear dispersion of phonon (***1***) at low $\mathbf{q}_\perp$ values (dashed lines) is systematically lower than in air-filled AAO (Fig. 4.7, Table 4.2). The softening of mode (***1***) is the first unexpected finding since $c_{lPDMS} \approx 3c_{air}$. The bending of the acoustic mode (***1***) was only observed when the nanopores contained PDMS, and its frequency decreased with porosity. An additional "*in-plane*" branch (***2***) with clearly non-acoustic behavior was also observed in AAO containing PDMS. For the "*out-of-plane*" wave propagation, the BLS spectra of AAO containing PDMS seen in Fig. 4.5(b) display a single doublet (***3***) irrespective of the porosity. But at comparable wave vectors, it appeared at much lower frequencies than the doublet (***1***) belonging to the "*in-plane*" phonon propagation (Fig. 4.5(a)); doublet (***3***) was absent in air-filled AAO. Based on the dispersion $\omega(\mathbf{q}_\parallel)$ displayed in Fig. 4.6 (light grey area), branch (***3***) in PDMS-infiltrated AAO is acoustic with a phase velocity (980 m/s) being slightly slower than in bulk PDMS. The "*out-of-plane*" dispersion included an additional longitudinal acoustic phonon (***5***) appearing at much higher frequencies than branch (***1***) for the "*in-plane*" phonon propagation (Fig. 4.6).

The dispersion $\omega(\mathbf{q}_\perp)$ for the "*in-plane*" propagation of phonons with longitudinal polarization in air-filled AAO (solid lines) and AAO containing PDMS (symbols) with three different

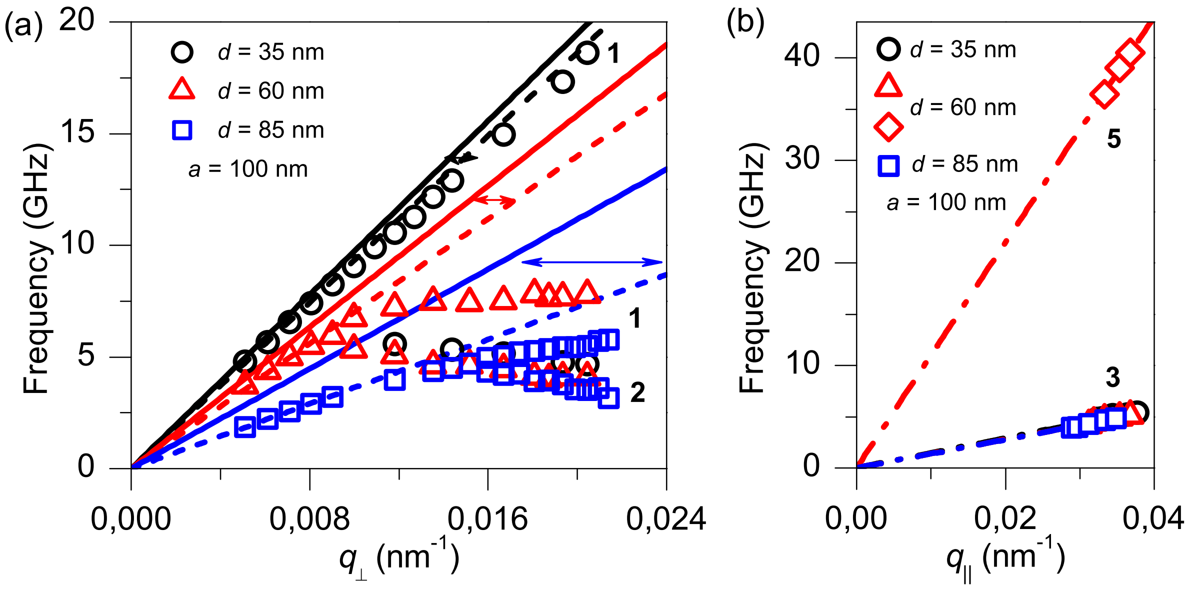

Figure 4.7.: Dispersion relations of both (a) "*in-plane*" ($\mathbf{q}_\perp$) and (b) "*out-of-plane*" ($\mathbf{q}_\parallel$) longitudinal phononic modes (***1-3,5***) in AAO containing PDMS. The black, red and blue solid lines in e represent the dispersion relations for native AAO with p = 11%, p = 32% and p = 65%, while the corresponding dashed lines represent the effective sound velocities in corresponding AAO scaffolds containing PDMS. The branch (***5***) is shown only for AAO with p = 32%.

porosities is shown in Fig. 4.7. In AAO containing PDMS, one longitudinal acoustic phonon branch (***1***) was observed at low frequencies. The corresponding dispersion was linear (dashed lines) and thus describes phonon propagation in a homogeneous effective medium for long wavelengths $\Lambda(=2\pi/\mathbf{q}_\perp)$ exceeding the lattice constant a. The slope of the dashed lines yields c_l = 5830 m/s, 4520 m/s and 2720 m/s for porosities 11%, 32% and 65%, respectively, which are systematically lower than the sound velocity in the corresponding air-filled AAO (4.2). In addition, the disparity (horizontal arrows in Fig. 4.7(a) increased with porosity, reaching about 800 m/s for p = 65%. Finally, the additional "*in-plane*" branch (***2***) was observed in AAO containing PDMS for any d value between 35 and 85 nm.

Table 4.2.: Experimental effective medium velocities in PDMS-filled AAO.

	in-plane (m/s)	*out-of-plane* (m/s)	
PDMS-filled AAO	Mode ***1***	Mode ***3***	Mode ***5***
$p = 11\%$	5830	920	
$p = 32\%$	4520	870	6910
$p = 65\%$	2720	860	

4.5. FDTD modeling

The elastic wave propagation in AAO along high symmetry directions of the two-dimensional lattice constituted by the nanopores and the influence of liquids located in the nanopores was simulated by means of numerical band structure calculations using the Finite Difference Time Domain (FDTD) method.[55]

The band structure curves were calculated using a three dimensional unit cell with dimensions ($a \times a\sqrt{3} \times 0.1a$), which was repeated in the three directions of space according to the periodic Bloch equations. Thus, the structure was infinite along the *z* direction and periodic in the (*x*, *y*) plane. The space was discretized in using a mesh interval equal to $\Delta x = \Delta y = \Delta z = a/30$. The equations of elasticity were solved with a time integration step $\Delta t = \Delta x/4$ and a number of time step equal to 2^{19} which was necessary tested time for good convergence of the numerical calculation. An initial randomly amplitude of the displacement was applied inside the unit cell. At the end of the time calculation, the displacement was recorded and transferred into Fourier series, for various wave vector *k*. The band structures were rendered in terms of frequency and function of the modulus of the wave vector, and were plotted along the principal directions of propagation of the 2D irreducible Brillouin zone (BZ), ΓJ and ΓX of the phononic crystal and in the direction ΓZ, out-of-plane, parallel to the cylinders axis.

The displacement field calculation was similar to the dispersion curves computation except that the initial randomly excitation of the displacement was replaced by a periodic wave source during a determined time at two specific points of the unit cell. The source generated a quasi monochromatic wave at the same frequency as the eigenfrequency of the chosen wave vector. Because both the wave vector and the frequency were assigned, a specific eigenmode was excited and the displacement field was recorded and highlights the properties of the mode. In those 3D graph representations, the color and the size of the points symbolize the local displacement while the white color corresponds to a displacement equal to zero (Fig. 4.10 to Fig. 4.12).

The sound velocities c_{lAAO} = 7300 m/s, c_{tAAO} = 3750 m/s and c_{lPDMS} = 850 m/s were evaluated so as to obtain a good fit of the experimental values of the "*in-plane*" effective acoustic velocities deduced from BLS spectra, assuming mass densities of ρ_{AAO} = 3970 kg/m^3 and ρ_{PDMS} = 1045 kg/m^3. Note that AAO consists of amorphous alumina containing incorporated water and electrolyte anions. Hence, the sound velocities extrapolated for *p* = 0 (c_l = 6180 m/s, c_t = 3740 m/s in Fig. 4.8) are significantly lower than in crystalline alumina such as sapphire (c_l = 11320 m/s, c_t = 6870 m/s). Moreover, a higher c_{lAAO} for the phonon propagation parallel (7830 m/s) and perpendicular (7300 m/s) to the pores was required to achieve good agreement with the sound velocity of branch (**5**) (Fig. 4.6 and Fig. 4.7). The verified nanomechanical anisotropy in the AAO membranes is in line with the internal structure of the pore walls of AAO, as revealed by SEM, and the anisotropic stress occurring during the anodization[135].

Figure 4.9(a), (b) shows the band structure of air-filled AAO (*p* = 32%; solid black symbols) and AAO (*p* = 32%) infiltrated with low molecular mass poly(dimethylsiloxane) (PDMS)

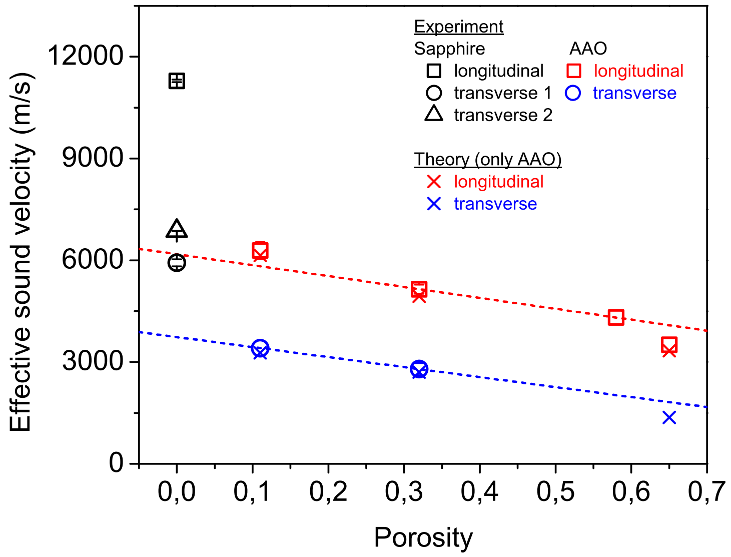

Figure 4.8.: Effective sound velocity c in AAO as a function of porosity .The experimental and computed longitudinal sound velocity for empty (open squares) and filled with PDMS holes (open circles) is indicated in black and red symbols respectively. The experimental shear sound velocity in empty (blue triangles) and filled (inverse triangles) is compared to the theoretical values indicated by red triangles. All lines are to guide the eye.

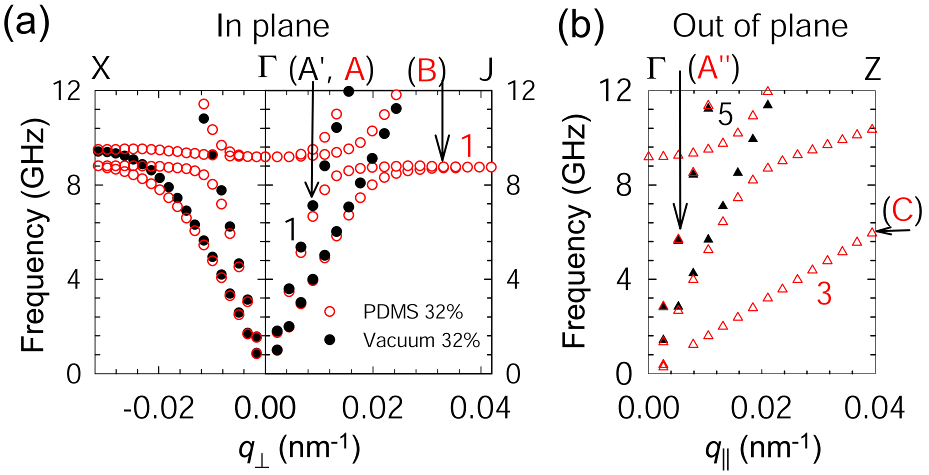

Figure 4.9.: Theoretical band structures of “*in-plane*” (a) and “*out-of-plane*” (b) phononic dispersion curves in AAO (a = 100 nm; d = 60 nm; p = 32%) either with air-filled nanopores (black solid symbols) or containing fluid PDMS (red open symbols).

(a) A' ($q_{\perp}$ = 0.01 nm^{-1}, f = 7.681 GHz)

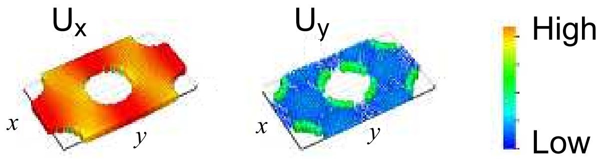

(b) A ($q_{\perp}$ = 0.01 nm^{-1}, f = 7.331 GHz)

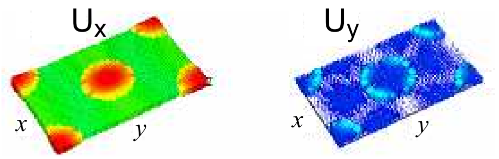

(c) B ($q_{\perp}$ = 0.04 nm^{-1}, f = 10.09 GHz)

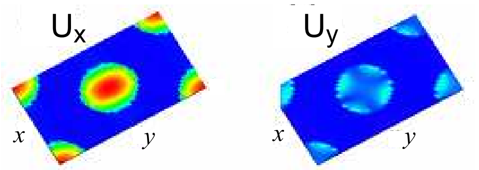

Figure 4.10.: Map of the distributions of the displacement U of the eigenmodes inside an AAO unit cell belonging to modes **A′**, **A** and **B** located on the branch (***1***) shown in Fig. 4.9(a).

(open red symbols) for wave propagation perpendicular to the nanopores (Fig. 4.9(a)), denoted by "*in-plane*" wavevectors ($\mathbf{q}_{\perp}$ in Fig. 4.2(a)) and wave propagation parallel to the nanopores (Fig. 4.9(b)), denoted by "*out-of-plane*" wavevectors ($\mathbf{q}_{\parallel}$ in Fig. 4.2(b)). The two lowest "*in-plane*" branches starting at the Γ point are longitudinal and transverse acoustic. Infiltrating AAO with PDMS leads to a significant decrease of the longitudinal sound velocity, $c_l = 2\pi f/q_{\perp}$, from 4940 m/s to 4730 m/s, whereas both acoustic branches bend due to their interaction with a flat band at around 8.5 GHz corresponding to a confined mode inside the PDMS cylinders. Increasing p to 65% (Fig. A.5) results in a strong decrease of c_l and an enhancement of the bending at a lower frequency. Mode **A′** is a longitudinal mode in air-filled AAO that propagates only through the AAO scaffold but not through the empty nanopores (Fig. 4.10(a)), whereas, in PDMS-infiltrated AAO, mode **A** with the same vector $q_{\perp}$ (= 0.004 nm^{-1}) is spread over both AAO scaffold and the PDMS located in the nanopores (Fig. 4.10(b)). Since the latter mode senses the PDMS, it propagates slower than mode **A′** in native AAO. Remarkably, mode **B** with $q_{\perp}$ = 0.03 nm^{-1}, which is characteristic of the flat band interacting with the propagating acoustic branches, is well confined inside the PDMS cylinders (Fig. 4.10(c)).

For the "*out-of-plane*" propagation, air-filled AAO (Fig. 4.9(b), black symbols) exhibits two

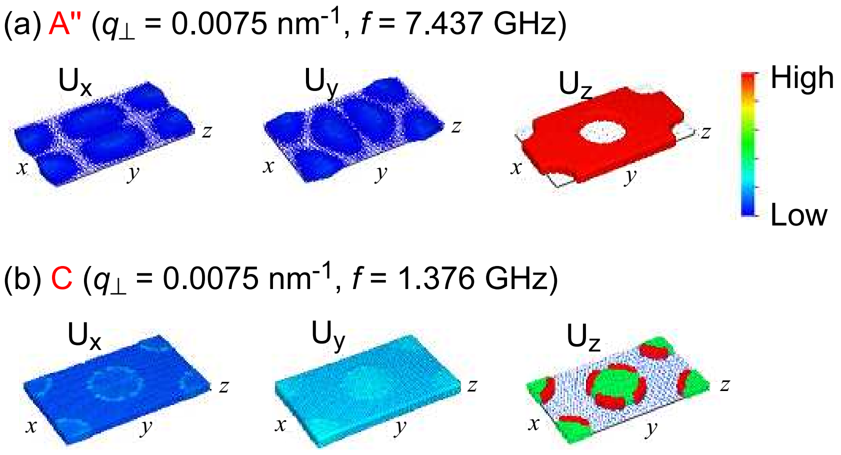
(a) A" ($q_\perp$ = 0.0075 nm^{-1}, f = 7.437 GHz)
U$_x$
U$_y$
U$_z$
x
y
z
High
Low
(b) C ($q_\perp$ = 0.0075 nm^{-1}, f = 1.376 GHz)
U$_x$
U$_y$
U$_z$

Figure 4.11.: Map of the distributions of the displacement U of the eigenmodes inside an AAO unit cell belonging to modes **A″** and **C** located on branches (***3***) and (***5***) shown in Fig. 4.9(b).

Table 4.3.: Comparison between the experimental and theoretical effective medium velocities c_{eff} for the "*in-plane*" phonon propagation.

		Longitudinal velocities (m/s)		Transverse velocities (m/s)	
		Experiment	Theory	Experiment	Theory
air-filled AAO	$p = 11\%$	6120	6140	3410	3270
	$p = 32\%$	5040	4940	2770	2695
	$p = 65\%$	3510	3325		1370
PDMS-filled AAO	$p = 11\%$	5830	6160		
	$p = 32\%$	4520	4730		
	$p = 65\%$	2720	2940		

acoustic branches with mainly longitudinal and transverse polarizations, whose velocities are lower than but close to those of bulk alumina. However, the dispersion behavior drastically changes when the nanopores contain PDMS. The lowest acoustic branch (***3***) (Fig. 4.9(b)), which is essentially longitudinal, penetrates only slightly into the AAO scaffold and is largely confined to the PDMS cylinders (see Fig. 4.11(b) for the mode denoted by **C** in Fig. 4.9(b)). Its velocity (about 900 m/s) is close to but slower than the sound velocity in bulk PDMS. Strikingly, branch (***3***) is absent in native AAO. The highest acoustic branch (***5***) (c_l = 6550 m/s) is polarized parallel (along *z*-direction) to the nanopores. Moreover, branch (***5***) is essentially confined to the AAO, as indicated by the biased distribution of the elastic field (**A″**) in Fig. 4.11(a). The spatial distribution of the elastic field belonging to mode **A** on branch (***1***) in Fig. 4.9(a) and to **A″** on branch (***5***) in Fig. 4.9(b) are distinctly different, thus rationalizing the much slower slope (4730 m/s) of the "*in-plane*" longitudinal phonon (***1***) that propagates also through the liquid PDMS.

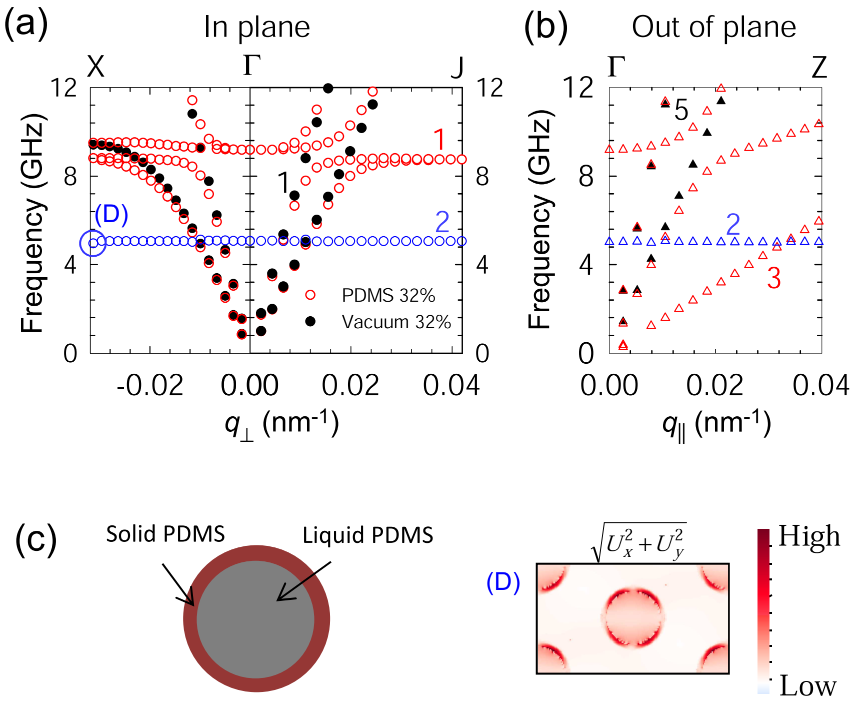

Figure 4.12.: Theoretical band structures of "*in-plane*" (a) and "*out-of-plane*" (b) phononic dispersion curves in AAO (*a* = 100 nm; *d* = 60 nm; *p* = 32%) either with air-filled nanopores (black solid symbols) or containing fluid PDMS (red open symbols). A new branch appears in the calculations only in the presence of a thin (5 nm) rigid PDMS interphase in the nanopores schematically shown in (c).

Low molecular mass PDMS (M_w = 980 g/mol) in the proximity of solid surfaces is prone to surface-induced ordering, resulting in the formation of a layered PDMS interphase with reduced mobility.[136] Thus, FDTD calculations were performed using a refined model in which the presence of a 5 nm thick solid PDMS interphase in the proximity of the pore walls with a finite transverse sound velocity c_t = 100 m/s was assumed. As seen Fig. 4.12(a) for the dispersion along ΓJ (blue points), this result in the appearances of a new flat branch (***2***) at 5.1 GHz, whereas branch (***1***) and its bending retain essentially the same characteristics as for the fully liquid PDMS cylinders. As shown for mode **D**, the displacement field $U_x^2 + U_y^2$ of branch (***2***) with mixed polarization is essentially confined to the PDMS interphase. The frequency of this branch depends on the thickness and the transverse sound velocity of the PDMS interphse (Fig. 4.12(c)). A strong evidence of the presence of a PDMS interphase at the pore walls is the additional "*in-plane*" branch (***2***) with clearly non-acoustic behavior observed in PDMS-filled AAO for any *d* value between 35 and 85 nm (Fig. 4.6 and Fig. 4.7). The almost flat branch (***2***) shown in Fig. 4.7 appears in the computed band diagrams of Fig. 4.12 only if the presence of a thin solid PDMS interphase is used, whereas this branch is absent if the simulations are based on models assuming the presence of homogeneous liquid PDMS cylinders in the nanopores (Fig. 4.9). An obvious consequence is the support of shear waves by the solidlike PDMS interphase[136], which was included in the calculations through an adjusted c_t and fixed interphase thickness[137]. As seen in Fig 4.12, the theory predicts the presence of a flat branch (***2***) (Fig. 4.6) and captures its frequency which increases with c_t and decreases with thickness. The assingment of the new branch (***2***) suggests that GHz phononics could serve as a generic method for the investigation of interphases in the nanocomposites.

4.6. Summary

We have applied high-resolution Brillouin spectroscopy on AAO-based nanocomposites containing hexagonal arrays of cylindrical nanopores filled with PDMS to demonstrate directional flow of elastic energy parallel and perpendicular to the pore axes and phonon localization. AAO has great potential as a platform for the design of tunable hypersonic phononic systems with engineered high-frequency phononic properties outside the band gap regions. Increasing the pore diameter *d* results in an enhancement of bending of the propagation band due to a confined mode inside PDMS cylinders. The proper adjustment of the lattice constants of self-ordered AAO and the possibility to deposit a plethora of materials covering a broad range of elastic properties in the nanopores enables tailoring the propagation of the elastic or acoustic waves perpendicular and parallel to the pores. Moreover, the sensitivity of GHz phononics to the interphase may pave the way for probing interfacial interactions in hybrid systems for which conventional techniques cannot be applied.

5. Tuning and switching hypersonic phononic properties of impedance-contrast nanocomposites

5.1. Introduction

Nanocomposites are a class of materials, the importance of which for a broad variety of industrial applications cannot be overestimated. Commonly, they are characterized by irregular structure, and clustering of dispersed filler particles may significantly deteriorate their properties. Up to now, their physics is not satisfactorily understood, and their design on the mesoscopic or even molecular scale is still challenging. However, it would be an intriguing perspective to create designer nanocomposites that exhibit specific functions related to rationally generated structural anisotropy or to likewise tailored, well-defined periodicity. Ultimately, such advanced nanocomposites would show smart behavior or stimuli-responsive properties.

Whereas the tailoring of mechanical properties and electric conductivity of nanocomposites has received much attention, the lack of control over their morphology has prevented the systematic tuning of their phononic properties. The phononic band diagram of periodic composite media can be engineered by the solid or liquid nature of the components, the contrast between their densities and elastic constants, their volume fractions, as well as by the symmetry and morphology of the lattice they constitute. Significant interactions between sound waves and composite media through which they propagate can occur if the frequency of the former and the periodic variations in elastic contrast of the latter are commensurate. Nanocomposites characterized by periodic elastic contrast variations on nanoscopic length scales could enable highly efficient phonon management in the hypersonic frequency range. Whereas only few attempts to adapt concepts for functional phononic bandgap structures to the GHz frequency range have been reported,[42, 43, 45, 126] predictive understanding of hypersonic systems and their rational engineering is still immature, despite the potential of such systems for a plethora of applications,[128].

Only a limited effort has been made to explore self-ordered AAO as a rigid, inorganic scaffold in well-defined model nanocomposites.[131, 138, 139] This is surprising since, in contrast to disordered filler/matrix systems, organic/inorganic hybrid systems based on AAO combine well-defined morphology and well-defined anisotropy. AAO-based membrane configurations are ideal model systems for the investigation of hypersound propagation, because their periodicity in elastic contrast imposed by the morphology of the AAO matches the length scales required to manipulate sound in the GHz frequency range. Moreover, directed sound propagation can be investigated because of the intrinsic anisotropy of AAO. Finally, AAO is transparent to UV light and visible light so that Brillouin light scattering (BLS),[7, 42] a well-established technique in the characterization of phononic systems, can be applied to probe the hypersonic behavior of AAO-based elastic-contrast nanocomposites.

Poly(dimethylsiloxane) (PDMS) has been widely investigated as a soft model component in the investigation of nanocomposites. Nuclear magnetic resonance (NMR) spectroscopy,[140, 141] dielectric relaxation spectroscopy[142] and dynamic mechanical analyses[143] revealed that in nanocomposites consisting of PDMS matrices filled with silica nanoparticles the filler particles are surrounded by two or more PDMS layers with restricted segmental mobility and a glass transitions at higher temperature or lower frequency than in the bulk. Direct evidence for modified dynamics in the GHz and THz range characterized by reduced segmental mobility was evidenced by quasielastic neutron scattering.[144] The overall thickness of the PDMS interphase, as determined by a broad range of methods for a likewise broad range of molecular weights, was reported to range from 1 to 5 nm.[140, 143–145] Molten PDMS with a molecular weight of $\approx$3700 g/mol ($\approx$50 repeat units) located between two molecularly smooth mica surfaces formed layered structures near the solid interfaces.[146] In extremely thin films ($\leq$5 nm), entropic repulsion resulted in conformational restrictions of the PDMS molecules was an oscillatory function of thickness with a repeat spacing corresponding to the width of the polymer molecule. The oscillatory force ranged 7-8 chain widths (about 5 nm), whereas dynamic force measurements revealed a hydrodynamic thickness of the immobilized layer of 2-3 nm.[146] Evmenenko et al. evidenced molecular layering for films thinner than 9 nm consisting of low molecular weight PDMS ($M \leq 1000$ g/mol) deposited onto a smooth Si wafer by X-ray reflectivity.[136] In thick films of PDMS with molecular weights of 3780 g/mol and above, no layer structure was found to be stable for entropic reasons, but interphases with a thickness of about a few nm appeared.[145]

In chapter 4, we have shown that probing the hypersonic properties of PDMS/AAO nanocomposites, which can be considered as a model system for nanocomposite materials characterized by pronounced elastic contrast between its components by BLS, reveals peculiar features in the GHz frequency range that are not accessible by other characterization methods, including directional flow of elastic energy parallel and perpendicular to the nanopores as well as phonon localization.[131] NMR investigations revealed that thin films of PDMS with molecular weights of the order of 10000 g/mol deposited from diluted solutions onto the pore walls of AAO are arranged in discrete layers characterized by step-wise increase in motional freedom.[147, 148] Strikingly, in the phononic dispersion diagrams of PDMS/AAO, elastic contrast nanocomposites branches apparently related to the presence of a PDMS interphase at the pore walls with enhanced elasticity showed up even though the pore volume was completely filled with PDMS.[131]

Here we present an in-depth study of the phononic properties of AAO-based elastic-contrast nanocomposites. Liquid poly(dimethyl siloxane) (PDMS), liquid polyethylene glycol (PEG),

Table 5.1.: Sound velocities and densities of materials

Material	c_l (m/s)	c_t (m/s)	ρ (kg/m^3)	ΔZ
AAO	7300[a]	3750[a]	3970[d]	
PDMS	1050 ± 20[b]		974[e]	27.5
PEG	1900[b]		1140[f]	12.4
liquid PVDF	1220[c]		1490[g]	14.9
α-PVDF	2480[b]	775[h]	1900[e]	6.8

[a] Ref. [127].
[b] Measured by BLS at room temperature (20 °C).
[c] Measured by BLS at 180 °C.
[d] Ref. [103].
[e] Value of PDMS with a viscosity-average molecular weight of 10^5 was determined using two pycnomieters at 20 °C.[149]
[f] Value of PEG with a molecular weight of 300 and methylated-ended was determined at 30 °C.[150]
[g] Value of PVDF with a molecular weight of 197000 g/mol was determined by the measurement of pressure, volume and temperature at 180 °C.[151]
[h] Value was determined for α-pahse of PVDF at room temperature.[152]
[i] Value of transverse velocity was determined by ultrasonic measurement at room temperature.[153]

liquid poly(vinylidene difluoride) (PVDF) and solid PVDF were selected as soft model components, the bulk densities and bulk longitudinal sound velocities of which cover a broad range (Table 5.1). In Table 5.1, the elastic impedance (Z = ρc) contrast ΔZ is defined as ΔZ = $\rho_{AAO} c_{lAAO} / \rho_i c_i - 1$ where ρ_{AAO} and ρ_i are densities of AAO and infiltrate material, whereas c_{lAAO} and c_i are velocities of AAO and infiltrate material, respectively. On the other hand, liquid PEG has a significantly higher longitudinal bulk velocity than liquid PDMS, whereas the bulk densities are similar. Therefore, it is obvious that PDMS/AAO nanocomposites have a significantly higher elastic contrast than PEG/AAO nanocomposites. On the other hand, liquid PVDF has a significantly higher bulk density than liquid PDMS, whereas bulk longitudinal sound velocities are comparable. Finally, semicrystalline PVDF has a significantly higher bulk sound velocity and a significantly higher bulk density than liquid PDMS. Hence, by comparing PDMS$_{(l)}$/AAO, PEG$_{(l)}$/AAO, PVDF$_{(l)}$/AAO and PVDF$_{(s)}$/AAO the influence of the longitudinal sound velocities and the densities of the soft components infiltrated in AAO can be systematically elucidated.

Moreover, up to now, AAO-based elastic contrast nanocomposites have been considered as static phononic systems. Using PVDF as a semicrystalline model polymer, we finally demonstrate that the exploitation of first order phase transitions such as melting and crystallization allows reversibly modifying the elastic properties and densities of materials residing in the

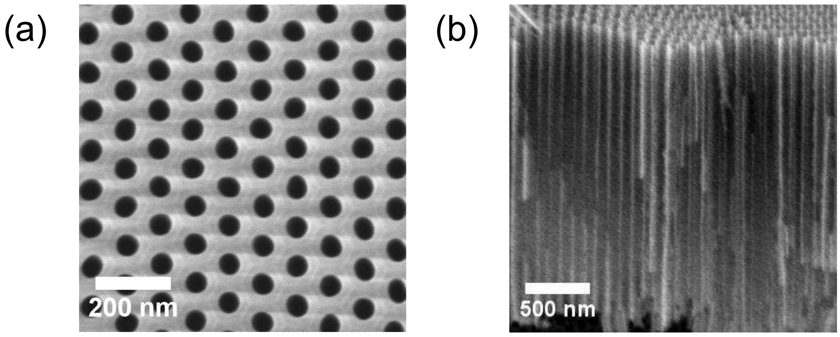

Figure 5.1.: Scanning electron microscopy (SEM) images of AAO. (a) top view and (b) cross sectional image.

nanopores. In turn, the phononic band structure, the density of states and ultimately the hypersonic properties of AAO-based elastic-contrast nanocomposites can be switched.

5.2. Sample preparation

As described in Chapter 3, self-ordered AAO was prepared following Masuda's two-step anodization process[73, 74]. Ultrapure aluminum substrates (99.999%, *d* = 20 mm, thickness = 500 μm, Goodfellow GmbH) were anodized in 0.3 M oxalic acid at 40 V. Anodization in oxalic acid yielded AAO with a lattice constant of about 100 nm. To increase the porosities, the nanopores were widened by isotropic etching in 0.3 M oxalic acid at 30°C, resulting in a diameter of 60 nm (Fig. 5.1(a)). Then, the AAO was infiltrated with poly(dimethyl siloxane) (PDMS, M_w = 1350 g/mol, M_n = 980 g/mol) or poly(ethylene glycol) (PEG, M_w = 400 g/mol) at room temperature. The PDMS had trimethylsilane (-Si(CH_3)$_3$) end groups and The PEG had hydroxyl (-HO) end groups. Also, two different kinds of samples were prepared for AAO infiltrated with poly(vinylidene fluoride) (PVDF, Aldrich, M_w = 180000 g/mol, M_n = 71000 g/mol): i) PVDF was infiltrated into the AAO by melting on AAO, wetting time 10 min. Then, it was cooled down to room temperature at a rate of 1 K/min. This sample showed preferred $\langle 020 \rangle$ texture, i.e. the $\langle 020 \rangle$ lattice planes are parallel to the AAO surface (Fig. 5.7(a)); ii) THe sample was initially prepared in the same way as in the first method. However, the excess PVDF surface film on top of AAO was removed and again the sample was cooled at a rate of 1 K/min. This sample did not show any preferred texture (Fig. 5.7(a)). Finally, tetracosane ($C_{24}H_{50}$, Aldrich-Europe, M_w = 338.66, T_m = 49 - 52 °C) was prepared by melting at 80 °C, wetting time 12 h. It was then cooled down to room temperature for BLS measurements.

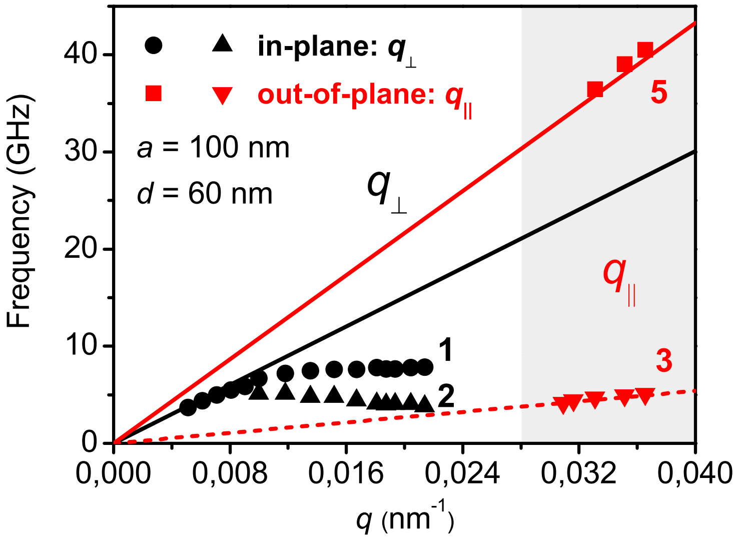

Figure 5.2.: "*In-plane*" ($q_\perp$) and "*out-of-plane*" ($q_\parallel$) longitudinal phononic branches (***1-3***, ***5***) in PDMS-filled AAO scaffolds (d = 60 nm; *a* = 100 nm). The black and red solid lines represent the effective sound velocities along the "*in-plane*" (data points in the unshaded area) and "*out-of-plane*" (data points in the light grey area) directions.

5.3. PDMS/AAO as a model system with high elastic contrast

In the previous chapter, we studied AAO with a lattice constant a of 100 nm, a pore depth of 20 μm and pore diameters *d* ranging from 35 to 85 nm infiltrated with trimethylsilane-terminated oligomeric PDMS with a molecular weight of 1350 g/mol. Figure 5.2 shows exemplary dispersion relations $\omega(\mathbf{q})$ in PDMS-filled AAO with *d* = 60 nm, *a* = 100 nm and a porosity $p = \pi d^2/(2\sqrt{3}a^2)$ = 32% for "*in-plane*" phonon propagation perpendicular to the pore axis (denoted by wavevector $\mathbf{q}_\perp$) and for "*out-of-plane*" phonon propagation parallel to the pore axis (denoted by wavevector $\mathbf{q}_\parallel$). The characteristic features of the dispersion relations $\omega(\mathbf{q})$ relevant to the discussion in this chapter can be summarized as follows.

(i) The acoustic ($\omega\sim\mathbf{q}$) phonons represented by branch ***5*** ("*out-of-plane*"), and by branch ***1*** ("*in-plane*") correspond to PDMS-filled AAO as an effective medium. However, the PDMS/AAO nanocomposites exhibit different effective medium sound velocities parallel (branch ***5***) and perpendicular (branch ***1***) to the nanopores.

(ii) The group velocity belonging to branch (***1***) becomes almost zero, as is obvious from its bending at high **q** values. This finding indicates localization of branch (***1***) through the interaction with a flat mode at a frequency $f_l\sim$7.8 GHz.

> (iii) Phonon guiding (branch ***3***) is realized when the nanopores are filled with PDMS, thus opening a new channel for the flow of the elastic energy. This channel of phonon propagation becomes inactive in AAO with air pores.
>
> (iv) In PDMS-filled AAO, a flat mode (***2***) with frequency f_i~5.1 GHz is observed, which can be attributed to the formation of a PDMS interphase with reduced mobility on the nanopore walls, as commonly observed in the proximity of smooth solid surfaces[136, 137]. The interphase-sensitive mode (***2***) could be reproduced in simulations only by using models involving a solid-like PDMS interphase.

Furthermore, the theoretical band structure calculations discussed in chapter 3[131] that provided detailed insight into the nature of the above-mentioned modes, by identifying their biased propagation through the polymer-filled AAO, are summarized below:

> (i) The acoustic "*out-of-plane*" branch (***5***) propagates mainly through the AAO scaffold with a sound velocity of 6930 m/s, whereas its counterpart "*in-plane*" branch (***1***) propagates through both the AAO scaffold and the polymer located in the nanopores with a slower sound velocity of 4520 m/s, as expected. Hence, the longitudinal moduli along the two directions differ by 230%.
>
> (ii) The bending of the acoustic branch (***1***) is due to the interaction with a flat band f_l~8.5 GHz corresponding to a confined mode inside the PDMS cylinders. The frequency f_l depends on the pore diameter and the nature of the material in the nanopores.
>
> (iii) The acoustic branch (***3***) propagates in the nanopores containing PDMS with a sound velocity of 980 m/s, which is slower than the sound velocity in bulk PDMS (1050±20 m/s).
>
> (iv) The new branch (***2***) is first and foremost sensitive to the transverse velocity of sound c_t and to the thickness of the PDMS interphase at the pore walls; f_i increases either by increasing c_t or by decreasing the thickness. The displacement of the elastic field is essentially confined to the PDMS interphase and polarized parallel to the nanopores.

5.4. PEG/AAO as a model system with low elastic contrast

Like PDMS, low-molecular-weight PEG is an isotropic liquid at room temperature. However, in contrast to PDMS, PEG is characterized by higher longitudinal sound velocity c_l and hence lower elastic contrast to AAO. Therefore, the comparison of PEG-filled AAO and PDMS-filled AAO allows the elucidation whether high elastic contrast is required to realize mode localization as well as directional flow of elastic energy, and whether high elastic contrast is a prerequisite for the occurrence of interphase-sensitive branches. It is reasonable to assume that lower elastic contrast between AAO and a soft component residing in its nanopores would affect the extent of phonon localization, which is represented by the bending of the acoustic branch (***1***) in Fig. 5.2.

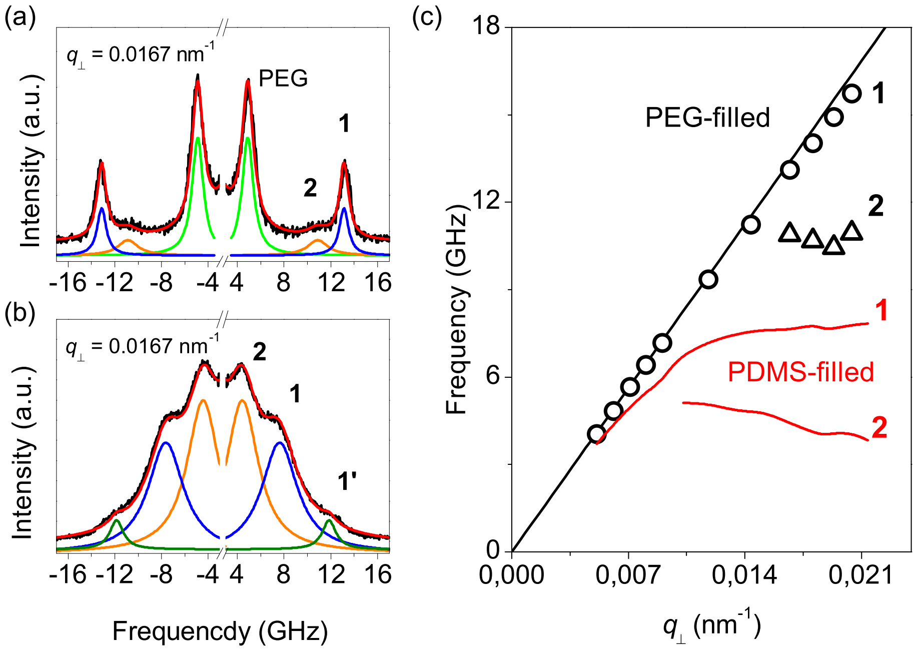

Figure 5.3.: "*In-plane*" BLS spectrum of (a) PEG- and (b) PDMS-filled AAO (d = 60 nm; a = 100 nm) at $\mathbf{q}_\perp$ = 0.0167 nm^{-1}. The red solid line shows the representation of the spectra by a sum of up to three lorentzian lines. (c) The dispersion relations for the two longitudinal acoustic (***1***) and the flat (***2***) branches. The black solid line represents the effective sound velocities for "*in-plane*" propagation in the PEG-filled AAO nanohybrids.

To verify these predictions, we studied the "*in-plane*" ($\mathbf{q}_\perp$) phonon propagation in AAO ($d \approx 60$ nm and $a \approx 100$ nm) filled with hydroxyl-terminated liquid PEG (Fig 5.3(a). Three modes are resolved in the exemplary BLS spectrum seen in Fig. 5.3(a), as indicated by the Lorentzian contributions. The peak denoted "PEG" with a frequency $f_{PEG} \approx 5$ GHz (at $q_\perp$ = 0.0167 nm^{-1}) is attributed to the bulk PEG layer remaining on the AAO surface exploited as an internal reference since f_{PEG} shows homogeneous acoustic behavior with a sound velocity c_{lPEG} ($= 2\pi f_{PEG}/q_\perp$) = 1850±30 m/s which is, within experimental error, the longitudinal sound velocity of bulk PEG. This corroborates the notion that interactions between PEG and AAO surface are hardly discernible. The acoustic branch (***1***) and the very weak flat branch (***2***) in the "*in-plane*" directions characterize the phononic properties of PEG-filled AAO nanohybrids. On the other hand, the bending of the acoustic branch (***1***) and the strong flat branch (***2***) in the "*in-plane*" dispersion diagram are charateristic of the phononic properties of PDMS-filled AAO (d = 60 nm, a = 100 nm) as represented in the BLS spectrum shown in Figure

5.3(b) recorded at $q_\perp$ = 0.0167 nm^{-1} as comparison to PEG-filled AAO.

The experimental dispersion relations for "*in-plane*" phonon propagation in PEG-filled AAO and, for comparison, PDMS-filled AAO are depicted in Fig. 5.3(c). The acoustic branch (***1***) and the very weak flat branch (***2***) are characteristic of the phononic properties of PEG-filled AAO. On the other hand, the bending of the acoustic branch (***1***) and the strong flat branch (***2***) are characteristic of the phononic properties of PDMS/AAO nanocomposites.

The linear dispersion of branch (***1***) indicated by the straight solid line in Fig. 5.3(c) represents longitudinal phonon propagation at long wavelengths probing a homogeneous medium and its slope yields the corresponding longitudinal sound velocity. In the PEG-filled AAO, the effective medium velocity c_l = 5040 m/s is higher than that in PDMS-filled AAO of c_l = 4520 m/s. Moreover, the bending of branch (***1***) at high $q_\perp$ (red line in Fig. 5.3(c)) is essentially missing in the PEG-filled AAO (Fig. 5.3(c)). Since the densities of PDMS and PEG are similar, the reduction of the elastic contrast ΔZ between AAO and PEG by a factor more than two compared to the PDMS/AAO system (c_{lPDMS} = 1050±20 m/s, c_{lPEG} = 1900 m/s already given above) remains as the origin of the significantly weakened phonon localization and renders the bending of mode (***1***) weak. The flat branch (***2***) can be interpreted as a layered interphase mode as mentioned above. It appears at higher frequency compared to ones observed in the AAO containing PDMS (5 GHz) and becomes very weak as seen in the amplitude of peak 2 relatively to peak 1 in the BLS spectra of PEG- and PDMS-filled AAO in Fig. 5.3(a) and 5.3(b). In fact, the formation of a PEG interphase in the direct vicinity of the pore wall is to be expected since the hydroxyl end groups of the PEG can form hydrogen bonds with alumina surfaces.

5.5. Tailoring the degree of dissipation of elastic energy by the soft component

In order to gain insight into thermal transport processes, we consider the linewidth (Γ) of the BLS spectra. The spectral linewidth of BLS is related to energy dissipation of phonon. Considering that the linewidth Γ is a function of q^2[154, 155], Γ can be expressed as $\Gamma = \xi q^2$ where ξ is a dissipation coefficient (or thermal diffusivity for solid) and can be expressed as follows:

$$\Gamma = \xi q^2 = \left[\frac{(\gamma - 1)\lambda}{m\rho_0 c_P} + \frac{\eta_v + \frac{4}{3}\eta_s}{m\rho_0}\right] q^2 \tag{5.1}$$

where γ is the specific heat ratio, η_v is the bulk viscosity, η_s is the shear viscosity, ρ is the density, *m* is the mass of a constituent, c_P is the specific heat at constant pressure, the longitudinal kinematic viscosity $D_v = \left(\eta_v + \frac{4}{3}\eta_s\right)/m\rho_0$ and the thermal diffusivity $D_T = \lambda/m\rho_0 c_P$. Since we treat the AAO-polymer nanocomposite as an effective medium here, it is very difficult to determine the properties of the polymeric components. However, the dissipation coefficient, in other words, the phonon lifetime, provides the relevant information to the phonon localization.

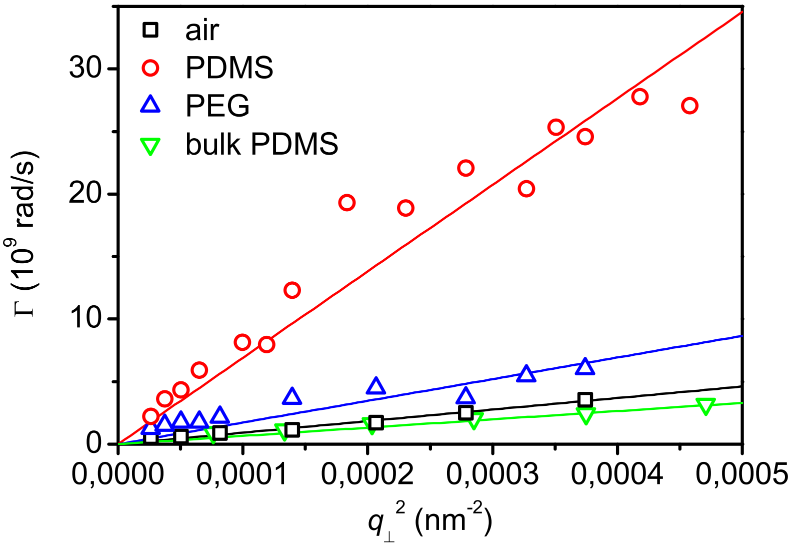

Figure 5.4.: Full width at half maximum (Γ) of BLS spectra plotted as a function of q^2 for branch (***1***). The solid lines are best fits to the data.

Table 5.2.: Comparison of dissipation coefficients

Sample	Bulk PDMS	air/AAO	PDMS/AAO	PEG/AAO
ξ[rad·m^2·s^{-1}]	6.6×10^{-6}	9.23×10^{-6}	6.91×10^{-5}	1.73×10^{-5}

The spectral linewidths of branch (***1***) were plotted as a function of q^2 for PDMS/AAO and PEG/AAO systems as shown in Fig. 5.4. As a reference, the linewidths of air-filled AAO and bulk PDMS are also plotted. Each dissipation coefficient, which was derived from the slope of the best fit, is summarized in Table 5.2. Apparently, the energy dissipation is dependent on the infiltrate material. In fact, air-filled AAO, bulk PDMS and PEG/AAO nanohybrids have similar dissipation coefficient, whereas the dissipation coefficient of the PDMS/AAO hybrid shows one order of magnitude bigger than other polymer/AAO nanohybrids. Consequently, it is conceivable that these observations could be associated with phonon localization and bending of branch (***1***). Namely, phonons are localized in the pores infiltrated with PDMS, resulting in a shorter phonon lifetime, while phonons are less localized in the pores infiltrated with PEG and travel through the polymer/AAO matrix, resulting in a longer phonon lifetime.

5.6. Reversible switching of phononic properties by crystallization and melting

External stimuli such as temperature changes may induce transitions such as crystallization, gelation, formation of mesophases in the component residing in nanopores of the AAO scaffold. Correspondingly, its phononic properties and, in turn, band structures and acousto-optical interactions of the nanocomposites are reversibly modified. It is thus an intriguing perspective to exploit sound propagation modes predominantly confined to materials located in the nanopores to monitor phase transitions. From a fundamental point of view, different infiltrated materials adopting fluid or solid phases can further verify the origin of the observed phononic modes in the band diagrams. For a simple proof of concept, we investigated the modification of the dispersion for both "*in-plane*" and "*out-of-plane*" sound propagations in AAO with *a* = 100 nm and *p* = 30% infiltrated with both poly(vinylidene fluoride) (PVDF) and tetracosane ($\mathrm{C}_{24}\mathrm{H}_{50}$). PVDF was not only selected as a model component because of the bulk densities and sound velocities of its liquid and semicrystalline forms (Table 5.1), but also because crystallization of PVDF inside the nanopores of AAO, which yields the monoclinic α polymorph[156] was intensively studied by wide angle X-ray scattering and differential scanning calorimetry.[127, 157] On the other hand, PVDF is representative of the important class of vinylidene-based fluoropolymers, which may exhibit, depending on the crystal modification, ferroelectric properties.[158]

First of all, the dispersion relations of PVDF-filled AAO, which shows preferred $\langle 020\rangle$ texture, were examined. To verify both the melting and the crystallization temperatures of PVDF inside nanopores, differential scanning calorimetry (DSC) measurements were performed. Figure 5.5 shows DSC results of PVDF-filled AAO (*d* = 60 nm; Fig. 5.5(a)) and bulk PVDF (Fig. 5.5(b)). The heating and cooling rates were 10 K/min. The DSC result of bulk PVDF shown as a reference exhibits a sharp crystallization peak at T_c = 135 °C in the cooling scan and a melting peak at T_m = 164 °C in the heating scan. Compared with bulk PVDF, the crystallization of PVDF inside nanopores occurs at 105 °C (T_{onset} = 120 °C), while the melting occurs at T_m = 168 °C. Therefore, the BLS measurements in liquid phase were performed at 180 °C, while in solid phase at room temperature.

To analyze the crystal texture of macroscopic ensembles of PVDF located inside AAO, WAXS measurements in reflection mode using a Philips X'oert MRD diffractmeter with cradle and secondary monochrometer for Cu K_α was performed. The setup used for WAXS measurements are schematically shown in Fig. 5.6. In this $\Theta/2\Theta$ geometry, Θ denotes the incident angle defined as the angle between the incident beam and the surface of the sample, while 2Θ is defined as the angle between the incident and the diffracted beams. In this geometry, only crystal lattice planes oriented parallel to the surface contribute to the intensity of a Bragg reflection. The scans were performed in the range of 15° to 30°. Figure 5.7(a) shows the XRD pattern of PVDF located inside AAO, which were prepared without a thick PVDF film on the surface of AAO. The Θ-2Θ XRD pattern shows three prominent peaks at 2Θ angles of 18.3° ($\langle 020\rangle$), 19.8° ($\langle 110\rangle$) and 25.4° ($\langle 021\rangle$). Figure 5.7(b) shows the XRD pattern

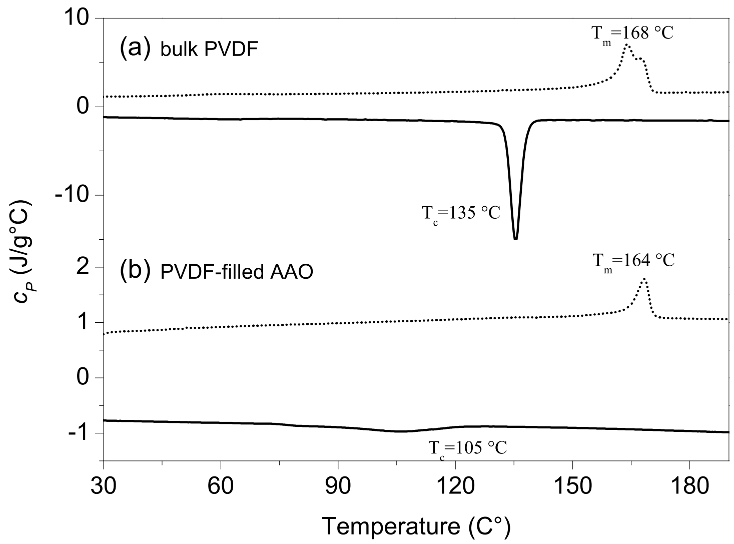

Figure 5.5.: DSC scans of (a) PVDF nanostructures in AAO and (b) bulk PVDF. Dotted curves are heating runs, while solid curves are cooling runs. Heating and cooling rates are 10 K/min.

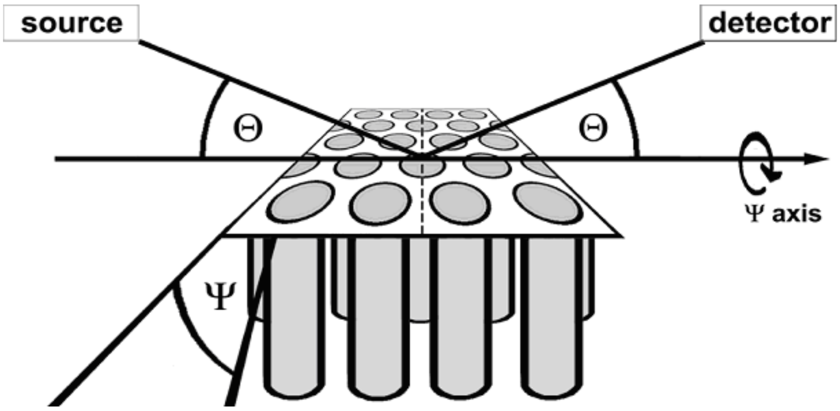

Figure 5.6.: Schematic of the WAXS setup. The AAO was mounted in such a way that the long axse of pores were oriented parpendicular to the plane defined by incident beam and detector.

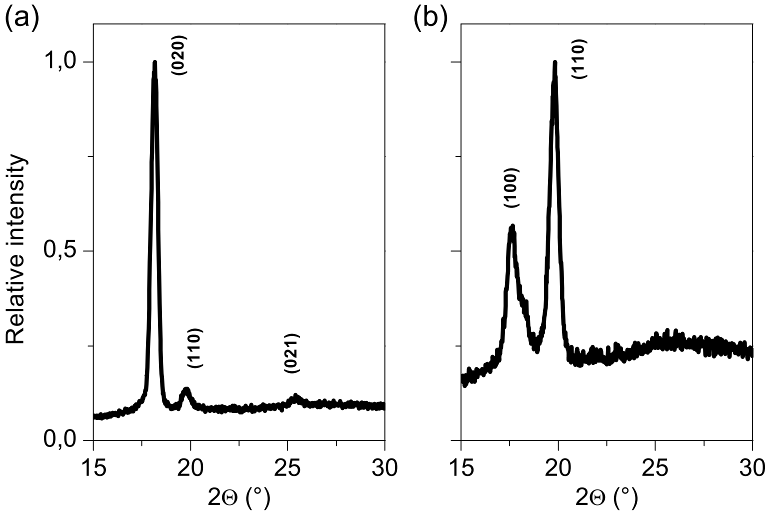

Figure 5.7.: XRD analysis of PVDF inside AAO. PDVF-filled AAO prepared (a) without a thick PDVF film on the surface of AAO and (b) with a thick PDVF film on the surface of AAO.

of PVDF located inside AAO, which were prepared with a thick PVDF film on the surface of AAO. The Θ-2Θ XRD pattern shows two prominent peaks at 2Θ angles of 17.7° ($\langle 100 \rangle$) and 19.8° ($\langle 110 \rangle$).

BLS measurements were performed at 293 K (PVDF in AAO is semicrystalline, Fig. 5.5(b)) and at 453 K (PVDF in AAO is liquid, Fig. 5.5(b)). Figure 5.8(a) shows corresponding BLS spectra recorded at $q_{\perp}$ = 0.0167 nm^{-1}. For AAO containing semicrystalline PVDF, the BLS spectrum displays only a single doublet associated to the longitudinal phonon (***1***) that shows linear dispersion but no bending up to $q_{\perp}\sim$0.02 nm^{-1} in the "*in-plane*" experimental band diagram shown in Fig. 5.9(a). On the other hand, although the BLS spectrum of AAO containing liquid PVDF also displays a single doublet at almost the same frequency, the peak became broader and slightly shifted to the lower frequency. Even though the sound velocities of liquid PDMS (ΔZ = 28) and liquid PVDF (ΔZ = 15) are of the same order of magnitude, the bending of branch (***1***) at high $q_{\perp}$ is missing in AAO containing liquid PVDF (Fig. 5.9(a)), such as in the case of PEG-filled AAO. Hence, we assume that the reduction in density contrast between AAO and PVDF related to the relatively high density of liquid PVDF (Table 5.1) could be the origin of the significantly weakened phonon localization and render the bending of mode (***1***) weak. It is conceivable that a large contrast of both sound velocity and density between AAO and infiltrate materials could be crucial factors for the phonon localization.

The BLS spectra representing the "*out-of-plane*" phonon propagation change drastically upon melting of PVDF (Fig. 5.8(b),(c)). Mode (***3***) at about 6 GHz disappears and a new mode (***4***) appears at much higher frequency ($\sim$20 GHz). The experimental dispersion relations for those two modes (***3***, ***4***) appearing in the BLS spectra seen in Fig. 5.9(b) therefore display

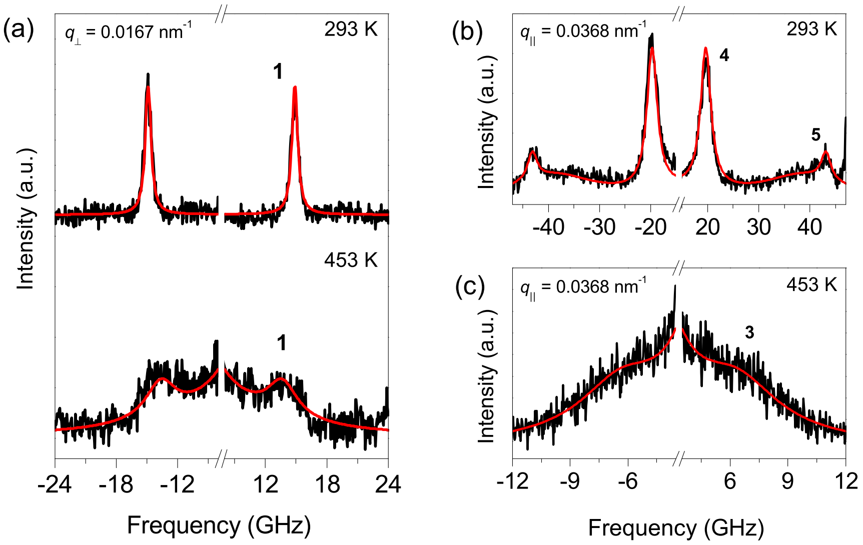

Figure 5.8.: BLS spectra of PVDF-filled AAO (d = 60 nm; a = 100 nm) measured at 293 K (PVDF is crystalline) and at 493 K (PVDF is liquid) (a) for $q_\perp = 0.0167\ \mathrm{nm}^{-1}$ perpendicular to the nanopores and (b) for $q_{||} = 0.0368\ \mathrm{nm}^{-1}$ parallel to the nanopores.

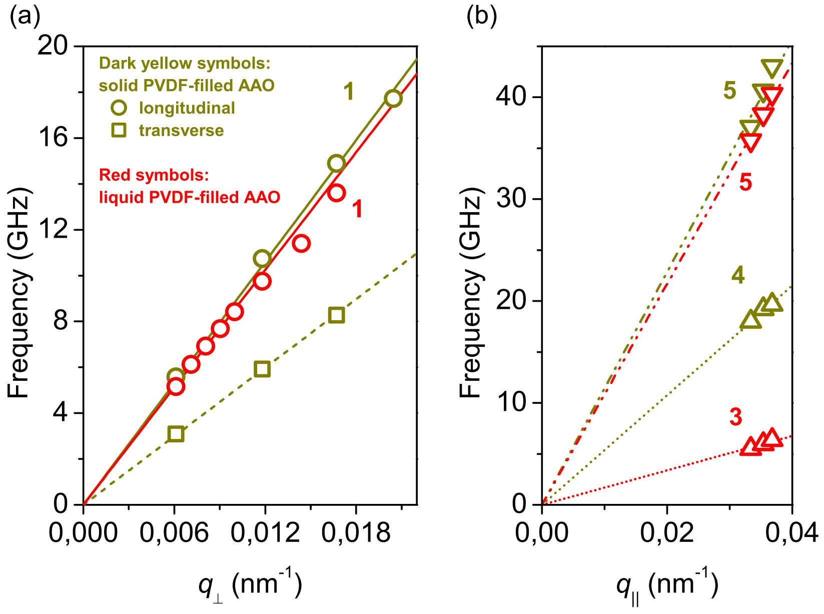

Figure 5.9.: Dispersion relations for “*in-plane*” ($q_\perp$) and “*out-of-plane*” ($q_{||}$) longitudinal acoustic modes in crystalline PVDF-filled AAO at 293 K and liquid PVDF-filled AAO at 453 K.

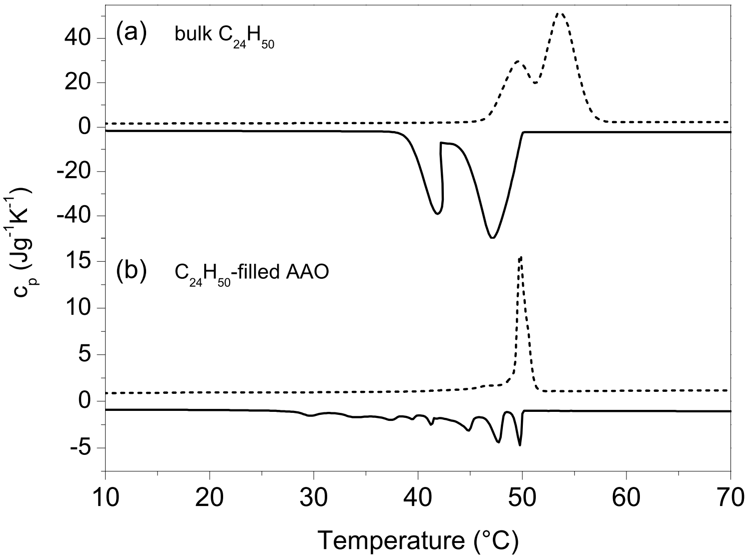

Figure 5.10.: DSC scans of (a) bulk $C_{24}H_{50}$ and (b) $C_{24}H_{50}$ nanostructures in AAO. Dotted curves are heating runs, while solid curves are cooling runs. Heating and cooling rates are 10 K/min.

very different slopes corresponding to velocities of 3380 m/s and 1060 m/s in the case of the solid (***4***) and liquid (***3***) PVDF, respectively. At the same time, the sound velocity of the longitudinal effective medium mode (***5***) does not change significantly when PVDF residing in the nanopores transforms from solid (7170 m/s) to liquid (6810 m/s).

After the completion of BLS measurements for liquid PVDF-filled AAO, PVDF were crystallized by cooling to room temperature. The resulting crystal orientation of PVDF after this cooling treatment does not show any preferred texture. However, the dispersion relations of this semicrystalline PVDF-filled AAO of both the "*in-plane*" and "*out-of-plane*" phonon propagation show the same behavior as textured PVDF-filled AAO. This indicates that phonon propagation is insensitive to the crystal orientation of PVDF.

Next, the dispersion relations of $C_{24}H_{50}$-filled AAO were examined. $C_{24}H_{50}$ is a linear paraffin which forms a triclinic crystalline phase[159, 160] below $\approx$ 45 °C and rotator phases below $\approx$ 51 °C.[161–164] Above 51 °C, tetracosane is liquid. Figure 5.10 shows DSC results of bulk $C_{24}H_{50}$ and $C_{24}H_{50}$-filled AAO. The heating and cooling rates were 10 K/min. In the DSC scan of bulk $C_{24}H_{50}$ as shown in Fig. 5.10(a), both DSC heating and cooling scans show two phase transition temperatures. The first transition occurs at 49.6 °C and the second at 53.3 °C during the heating scan, while the first transition occurs at 47.2 °C and the second at 41.8 °C during the cooling scan. In comparison, the phase transition process of $C_{24}H_{50}$-filled AAO is more complex. As shown in Fig. 5.10(b), the heating scan shows only one phase transition temperature at around 46.7 °C, while the cooling scan shows multiple peaks.

Bulk $C_{24}H_{50}$ shows only one phase transition during heating[165, 166], while two transitions during heating occur for odd alkanes (C_nH_{2n+2}) with n = 23 and n = 25[167]. The structure

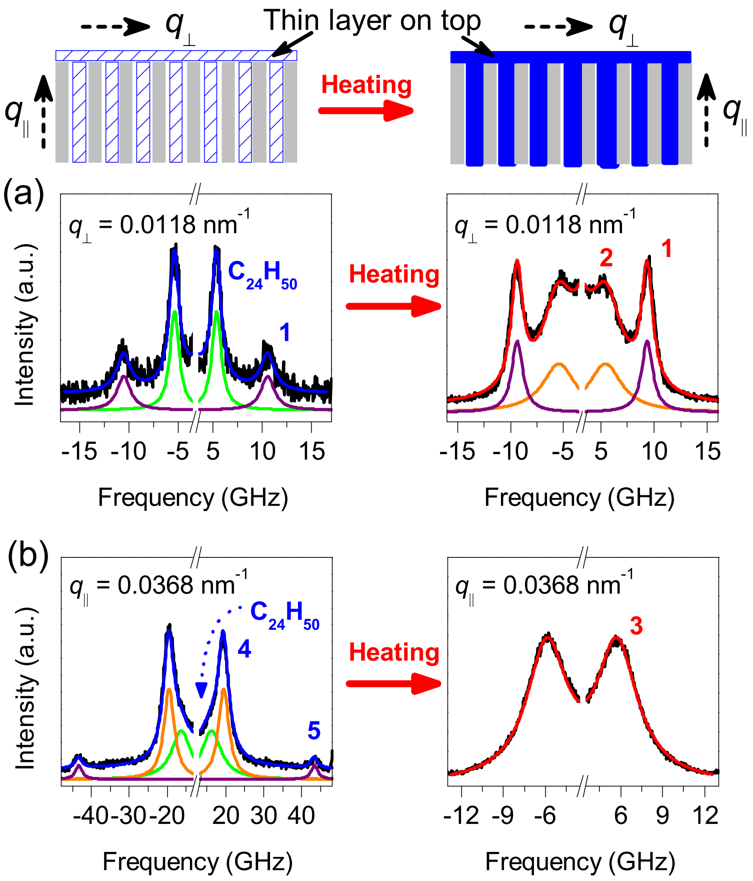

Figure 5.11.: BLS spectra of $C_{24}H_{50}$-filled AAO (d = 60 nm; a = 100 nm) measured at 20 °C ($C_{24}H_{50}$ is crystalline) and at 90 °C ($C_{24}H_{50}$ is liquid) (a) for $q_\perp = 0.0118\ \mathrm{nm}^{-1}$ perpendicular to the nanopores and (b) for $q_\parallel = 0.0368\ \mathrm{nm}^{-1}$ parallel to the nanopores.

changes from crystalline to rotator phase I with pseudo hexagonal packing and then to rotator phase II with hexagonal packing of the molecules. It could be possible that the confined $C_{24}H_{50}$ shows the additional rotator phase I. Furthermore, three phases are known to exist during cooling for $C_{24}H_{50}$. It is known that rotator transitions are inaccessible during heating but are visible during cooling due to a very large hysterisis on heating and cooling.[163, 166]

Similar to PDMS, the structure and dynamics of linear alkanes in the chain length range of tetracosane have been found to be altered in the presence of surfaces and interfaces. For example, surface freezing, i.e., the formation of a monolayer of molecules forming a rotator phase on the surface of the bulk liquid, was reported for temperatures up to 3 K above the freezing point,[168, 169] and surface freezing was also found to modify the wetting behavior of tetracosane on silicon oxide surfaces.[170] Moreover, medium-length n-alkanes show modified phase behavior when confined to nanopores with a diameter of about 10 nm[171, 172], or discrete

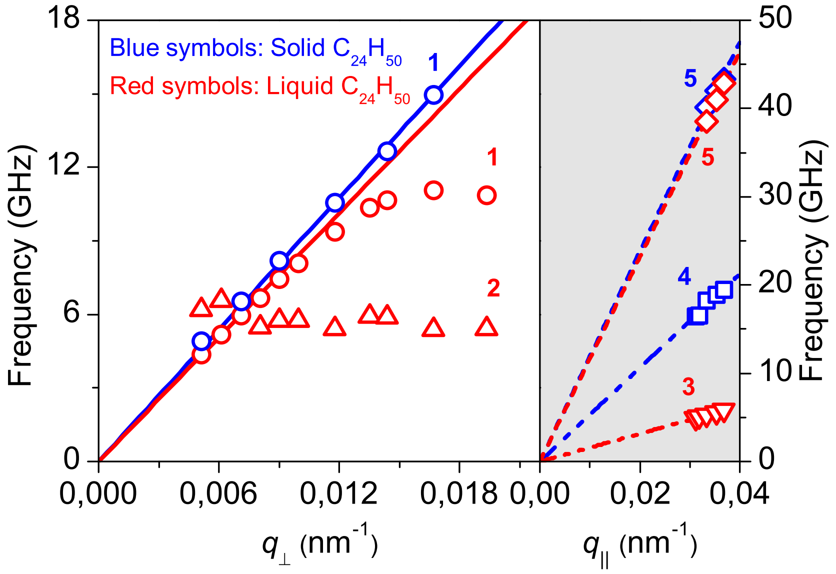

Figure 5.12.: Dispersion relations for "*in-plane*" ($q_\perp$) and "*out-of-plane*" ($q_{||}$) longitudinal acoustic modes in crystalline $C_{24}H_{50}$-filled AAO at 20 °C and liquid $C_{24}H_{50}$-filled AAO at 90 °C.

nanodroplets, with diameters in the 100 nm range.[173]

Figure 5.11 shows BLS spectra of AAO filled with the triclinic crystalline phase of tetracosane, which were measured at 293 K and 343 K, respectively. The peak appearing at a frequency $fC_{24}H_{50}{\sim}5$ GHz (at $q_\perp = 0.0118$ nm^{-1}) is attributed to a bulk $C_{24}H_{50}$ layer located on the surface of the AAO. On the one hand, the presence of such a layer connecting the tetracosane nanorods residing in the pores of the AAO the ensures complete crystallization of the latter. The bulk tetracosane layer was utilized as an internal reference showing homogeneous acoustic behavior with a sound velocity $c_{lC_{24}H_{50}}$ $(= 2\pi f/q_\perp) = 2850$ m/s.

The BLS spectra representing the "*out-of-plane*" phonon propagation change drastically upon melting of $C_{24}H_{50}$ (Fig. 5.11(b)) as in PVDF-filled AAO. Mode (***3***) at about 5 GHz disappears and a new mode (***4***) appears at much higher frequency (∼19 GHz). The experimental dispersion relations for those two modes (***3***, ***4***) in Fig. 5.12 therefore display very different slopes corresponding to velocities of 3310 m/s and 990 m/s in the case of the solid (***4***) and liquid (***3***) $C_{24}H_{50}$, respectively. Consequently, there are three same main effects in the band diagrams associated with the crystallization of $C_{24}H_{50}$ and PVDF inside the nanopores: (i) the "*in-plane*" dispersion becomes simpler with the single acoustic mode (***1***) being marginal faster compared to its counterpart in solid $C_{24}H_{50}$ filled-AAO and PVDF (cf. Fig. 5.9, blue and red solid lines in Fig. 5.12), (ii) the "*out-of-plane*" dispersion is distinguished by the presence of a new acoustic mode (***4***) in place of mode (***3***) and (iii) the sound velocity of the longitudinal effective medium mode (***5***) does not change significantly when the $C_{24}H_{50}$ and PVDF residing in the nanopores transforms from solid to liquid, for which the changes are 7400 m/s to 7300 m/s and 7170 m/s to 6810 m/s for $C_{24}H_{50}$- and PVDF-filled AAO, respectively.

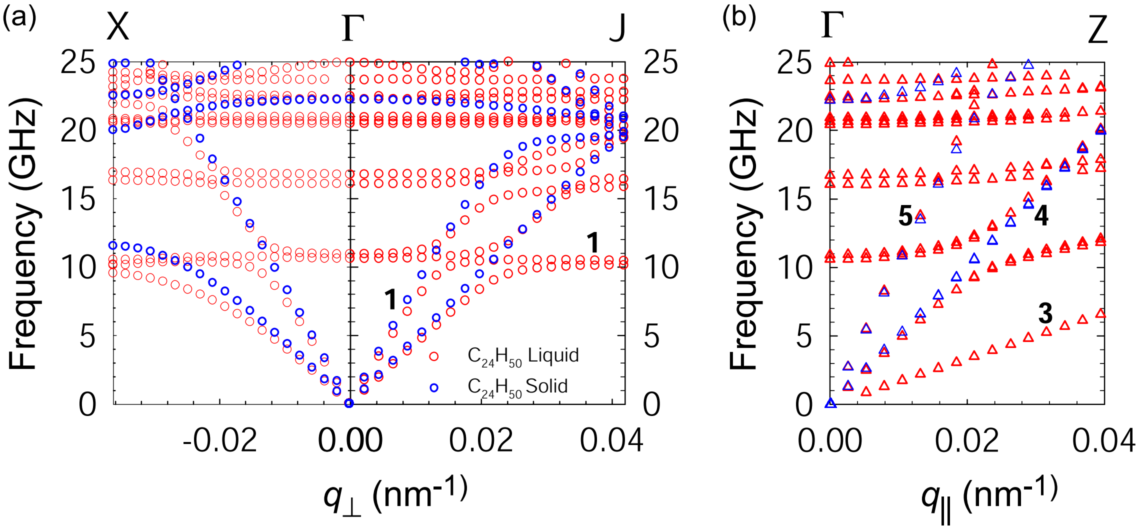

Figure 5.13.: Theoretical band structure of both "*in-plane*" (a) and "*out-of-plane*" (b) phononic modes for AAO with 30% porosity containing liquid $C_{24}H_{50}$ (red points) or a solid tetracosane (blue points).

We have calculated the dispersion curves of AAO containing either liquid tetracosane with a velocity of sound c_l = 1000 m/s or crystalline tetracosane (c_l = 3200 m/s and c_t = 1600 m/s). For "*in-plane*" sound propagation, the effective acoustic velocities in both types of samples are similar (5414 m/s for crystalline tetracosane; 4864 m/s for liquid tetracosane) and in agreement with the experimental sound velocity of mode (***1***) (5630 m/s, blue and 5200 m/s, red dashed lines) in Fig. 5.12(a). Based on the elastic field distribution, the effective sound velocity is predominantly determined by the speed of sound in the AAO and does not appear to be the simple average of the sound velocities in the pure components. Further, bending of branch (***1***) occurs at around 10.5 GHz for liquid tetracosane and at about 20 GHz for crystalline tetracosane (Fig. 5.13) due to the interactions with a flat band, in close analogy to the band diagram of AAO containing PDMS (Fig. 4.9(a)). For frequencies below 20 GHz both the absence of the flat band in the case of crystalline tetracosane and its appearance (at lower $q_\perp$) upon melting is in agreement with the experimental findings (Fig. 5.12). Moreover, the higher frequency of this flat band as compared to that of AAO containing PDMS at ≈8.5 GHz (Fig. 4.6) reflects the nature of this mode, which is confined to the material residing inside the nanopores of the AAO scaffold and is therefore modified as the elastic constant of the infiltrated material changes.

For "*out-of-plane*" propagation (Fig. 5.13(b)), the trends for liquid tetracosane are very similar to those for PDMS. In particular, the lowest acoustic branch is essentially a longitudinal mode confined to the tetracosane located in the nanopores with a velocity close to that of bulk tetracosane. However, when the tetracosane crystallizes, this low velocity acoustic branch (***3***) does not exist anymore and we find two branches with velocities higher by about 10% than those for "*in-plane*" propagation. The polarization of the lowest branch is mainly transverse with a sound velocity of 3150 m/s whereas the polarization of the highest branch is mainly longitudinal with a sound velocity of 6500 m/s. Based on these characteristics, the modes (***4***, ***5***) found experimentally are identified with the two acoustic branches in Fig. 5.12 (blue symbols in grey area) for AAO containing crystalline tetracosane. In qualitative agreement with the experiment (Fig. 5.12 gray area), the sound velocity of mode (***5***) remains essentially unchanged (6600 m/s) when the tetracosane becomes liquid. Therefore, crystallization of tetracosane is accompanied by a qualitative modification of the dispersion curves as well as the BLS spectra. In view of the good quantitative agreement between theory and experiment found for the "*in-plane*" propagation of mode (***1***), the deviation between the computed and experimental values of the sound velocity for the "*out-of-plane*" propagation of mode (***5***) implies nanomechanical anisotropy in the AAO membranes. In fact, a higher c_{lAAO} value for the direction parallel to the pores is required to achieve a good agreement. And this is another important experimental finding of this work. Since the volume expansion per aluminum atom upon anodization of aluminium causes considerable anisotropic stress in AAO[135] and recent reports even suggest that freshly formed alumina flows from the bases of the growing nanopores towards the cell walls, owing to growth stress and field-assisted plasticity[99] anisotropic elastic properties of the AAO scaffold are not unexpected but interesting to be verified, for the first time. Finally, the vastly different effect of the physical state of the infiltrated material on the "*in-*" and "*out-of-plane*" phonon propagation in the AAO is an intriguing new finding whose main features are captured theoretically.

5.7. Summary

Using BLS and model nanocomposites based on self-ordered AAO infiltrated with soft components, we have demonstrated that the hypersonic phononic properties of elastic-contrast nanocomposites can be tuned by adjusting the elastic contrast between AAO and soft or rigid components located in the nanopores. Peculiar features of the nanocomposites, including phonon localization and anisotropic propagation, depend on the elastic contrast between the AAO and the soft infiltrate components. Moreover, by taking advantage of the possible large or low elastic contrasts between the AAO scaffold and materials located in the nanopores, AAO has great potential as a platform for the design of tunable and switchable hypersonic phononic systems with engineered high-frequency acoustic properties. In contrast to sonic crystals with macroscopic feature sizes, nanostructured AAO-based hypersonic systems, which are not only mechanically and thermally stable but also transparent for UV-and visible light, allow the facile induction of phase transitions and other types of structural transformations with little energy consumption and in a well-controlled manner. Recent progress in the fabrication of three-dimensional AAO architectures[174] might pave the way for the design of phononic device configurations operated in the GHz range for mechanical filtering, advanced heat management, acousto-optical switching and for unconventional sensor configurations. The design of membrane-based phononic device components based on AAO is straightforward, and the application of lithographic top-down techniques might yield hierarchical hypersonic architectures, which could be used as hypersonic waveguides and mode coupling components.

6. Hypersonic Phononic Crystals based on Highly Ordered anodic Aluminium oxide

6.1. Introduction

In chapters 4 and 5, we have investigated how porosity and infiltrate material affect hypersonic phononic properties in nanocomposite media based on anodic aluminium oxide (AAO). AAO nanohybrid structures have been shown to have great potential as a platform for the design of tunable and switchable hypersonic phononic properties. However, since AAO films studied in previous two chapters have a polydomain arrangement of the pores as shown in Fig. 3.6(c), it is impossible to define the specific propagation directions in the Brillouin zone and investigate a complete phononic dispersion relation. It is desirable to verify the phonon dispersion relation $\omega(\mathbf{q})$ along any high symmetry directions in the reciprocal space since, in addition to determining the position of complete phononic bandgaps, it allows for studying the detailed features of the propagation bands.

The progress in phononic crystals, which has been supported by recent advances in nanofabrication techniques, has led to functional hypersonic phononic bandgap structures.[42, 43, 45, 175] The existence of a phononic bandgap in 3D hypersonic phononic crystals[42, 45] fabricated by self-assembling of polystyrene nanospheres, and a 2D hypersonic phononic crystal fabricated by multibeam interference lithography[43], has been demonstrated. These works, however, revealed only a partial bandgap. On the other hand, recently, Jang *et al*.[175] have demonstrated the shape-memory effect in a 2D phononic crystal on complete phonon dispersion relations. Although they demonstrated the formation of a complete bandgap after the transformation of the *p*6*mm* structure to the *p*2*gg*, it was very difficult to reveal it experimentally. However, these pioneering works have certainly opened the door for the concept of phonon management ranging from heat management to novel acousto-optical devices.

A brand new subject “phononics”, which is a new science and engineering of the properties of phonons in nanostructures, has drawn a great deal of attention.[128] In recent years, remarkable progress in controlling the flow of heat is being made toward the development of functional thermal devices including a thermal diode[176–179], thermal transistor[180, 181], phonon waveguide[182] and solid state thermal rectifier[183]. The realization of these functional thermal devices in nanoscale systems would have significant impact on society. Consequently, it is very important to control both nanoscale acoustic wave properties and nanoscale thermal transport properties. The elastic waves in the hypersonic frequency regime can be regarded as thermal vibration of atoms of a material. Therefore, hypersonic phononic crystals are promising building blocks which are capable of controlling the flow of heat.

Another promising application is acousto-optical devices. Wavelength-scale structured materials with periodical elastic modulus and refractive index distribution form simultaneous complete photonic and phononic bandgaps.[35] Therefore, photonic-phononic dual bandgap materials could lead to noticeable enhancement of acousto-optical interactions, thus resulting in the fabrication of novel acousto-optical devices[36–41].

The feasibility of AAO-based hypersonic phononic crystals to acousto-optical devices is high. AAO has been considered as a potential material platform for 2D photonic crystals and has been studied in the near-infrared and visible wavelength regions.[84–86] A proper selection of porosity and infiltrate material can lead to a phononic bandgap in AAO-based hypersonic crystals. Therefore, AAO can be thought of as a photonic-phononic dual bandgap material. Moreover, not only lattice constants but also the topology[112] of AAO is readily tunable.

In this chapter, complete phonon dispersion relations of highly ordered AAO are experimentally and theoretically demonstrated. Two types of samples have been investigated: (i) poly(ethylene oxide)-filled AAO with the lattice constant of a = 200 nm and porosity of p = 23% and p = 50%; and (ii) PDMS-filled AAO with the lattice constant of a = 200 nm and porosity of p = 23%. The tunability of complete phonon dispersion relations in response to changes in temperature was investigated for poly(ethylene oxide)-filled AAO. The phonon dispersion relations consisting of multiple propagation bands were observed along both high symmetry directions ΓX and ΓJ, while only the first propagation band was observed for PDMS-filled AAO. Theoretical band diagrams are in good agreement with experimental phonon dispersion relations.

6.2. Experimental

As described in Chapter 3, two sets of highly ordered AAO were prepared in accordance with the precedent[84, 85, 90]. Ultrapure aluminum substrates were anodized in 0.05 M oxalic acid at 80 V. Anodization in oxalic acid yielded AAO with a lattice constant of about 200 nm. To tailor the porosity, the initial diameters were widened by isotropic etching in 10wt% phosphoric acid at 30 °C. The resulting pore diameters were 100 and 150 nm, respectively, which were revealed with SEM images of the top view of the AAO as shown in Fig. 6.1. Representative SEM images of the top view of AAO with two different porosities $p = \pi d^2/(2\sqrt{3}a^2)$ reveal excellent uniformity, monodomain crystalline nature and very low defect in the samples over a large area. The well-ordered structure with hexagonal arrangement of cylindrical pores has a monodomain periodicity of 200 nm. The thickness of the anodic porous alumina was 40 μm.

Two different infiltration materials, poly(dimethyl siloxane) (PDMS, M_w = 1350 g/mol, M_n = 980 g/mol) and poly(ethylene oxide) (PEO, Fulka, M_w = 20000 g/mol, T_m = 63-66 °C), were used in this study. PDMS was infiltrated into AAO at room temperature, while PEO was infiltrated at 80 °C by melting on AAO, wetting time 12 h.

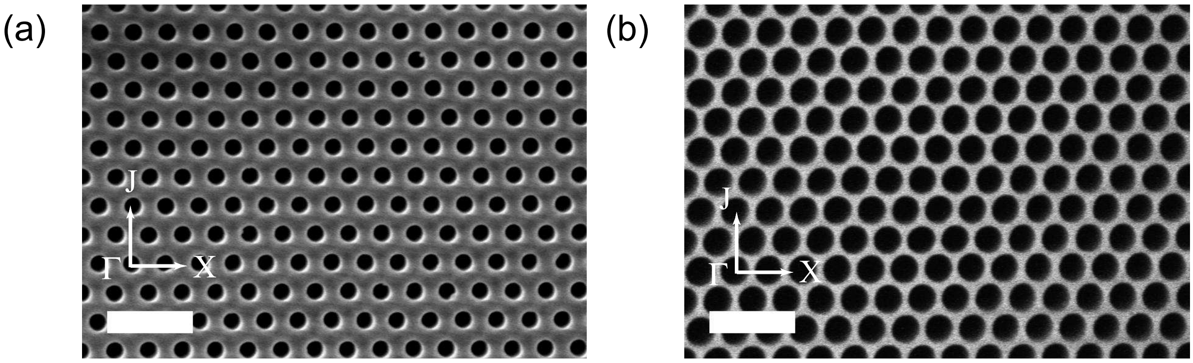

Figure 6.1.: Scanning electron microscope (SEM) images of native AAO. (a), (b), Top views. (a) porosity p = 23%, (b) p = 50% for lattice constant a = 200 nm. The scale bar in both images is 500 nm.

Two scattering geometries, which are transmission and reflection geometries, were the same as the ones used for chapter 4 and chapter 5 where the scattering wavevector $\mathbf{q}$ lies parallel or perpendicular to the pores. The schematic representation of the experimental geometry is shown in Fig. 6.2. The configuration of the transmission geometry (Fig. 6.2(a)) ensures that the scattering wavevector $\mathbf{q}_\perp$, which is defined by the wavevector of the incident light $\mathbf{k}_i$ and the scattered light $\mathbf{k}_s$ and the scattering angle θ, is always perpendicular to the pores, while the configuration of the reflection geometry ensures that $\mathbf{q}_{||}$ is parallel to the pores. In chapter 4 and chapter 5, AAO films have polydomain structures. Therefore, it was not possible to define the specific propagation direction. However, since the samples used here have a monodomain structure, any direction of $\mathbf{q}$ within the Brillouin zone can be experimentally accessed by simply rotating the sample. The direction of $\mathbf{q}_\perp$ in the Brillouin zone is here determined by 90° rotation of the sample.

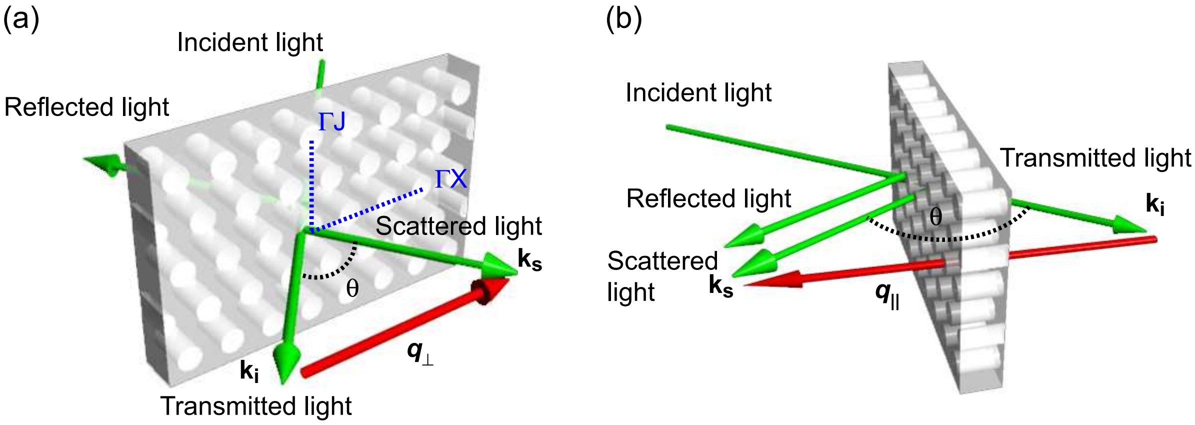
(a)
Incident light
Reflected light
ΓJ
ΓX
Scattered light
$\mathbf{k_s}$
θ
$\mathbf{k_i}$
$q_\perp$
Transmitted light
(b)
Incident light
Transmitted light
Reflected light
θ
$\mathbf{k_i}$
Scattered light
$\mathbf{k_s}$
$q_{||}$

Figure 6.2.: Schematics of scattering geometry: (a) transmission geometry and (b) reflection geometry.

6.3. Direct observation of complete phononic dispersion relations

The phononic band structures are essentially based on several parameters including the volume fractions of the constituent materials (porosity), the lattice topology and the density and sound speed ratios of the constituent materials. Here phase transitions of PEO were utilized to cause changes in the phononic properties. Figure 6.3 compares the BLS spectra of single crystal sapphire and AAO recorded along the two principal directions ΓX and ΓJ to illustrate the difference in phonon dispersion relations with the introduction of porosity. Sapphire refers to

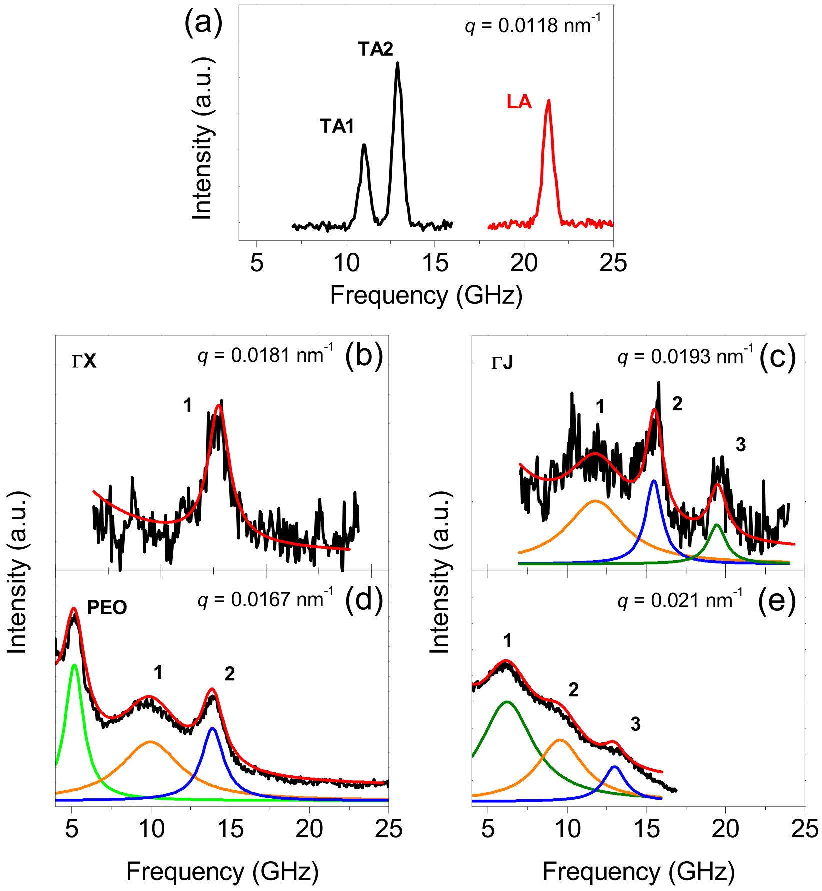

Figure 6.3.: BLS spectrum of (a) sapphire recorded at $q_\perp = 0.0118$ nm^{-1}, (b) AAO with a lattice constant of 200 nm and a diameter of 100 nm at $q_\perp = 0.0181$ nm^{-1} and solid PEO-filled AAO at $q_\perp = 0.0167$ nm^{-1} in ΓX direction, and (c) AAO with a lattice constant of 200 nm and a diameter of 150 nm at $q_\perp = 0.0193$ nm^{-1} and solid PEO-filled AAO at $q_\perp = 0.0167$ nm^{-1} in ΓJ direction (c). Here only anti-stokes sides are represented.

a α-Al$_2$O$_3$ which has the corundum structure. Although AAO has an amorphous structure, we compare the spectrum of monodoamin AAO with that of sapphire in order to understand the effects of nanostructured periodicity on elastic wave propagation. Figure 6.3(a) shows both the polarized (VV) and the depolarized (VH) BLS spectra of sapphire recorded at $q_\perp$ = 0.0118 nm^{-1}. The BLS spectrum in the VV geometry displays one peak at 21.3 GHz, which corresponds to the longitudinal mode (LA) with a sound velocity of 11320 m/s, while the BLS spectra in the VH geometry display two peaks at 11.0 GHz and 12.9 GHz, which correspond to the transverse modes (TA1 and TA2) with sound velocities of 5850 m/s and 6870 m/s.

The spectra of AAO differ from that of sapphire. Figure 6.3(b) and (c) show the VV spectra of air-filled AAO with a porosity of 23% and 50%, respectively, which were recorded at $q_\perp$ = 0.018 nm^{-1} and $q_\perp$ = 0.193 nm^{-1} along ΓX and ΓJ. The position of the longitudinal mode (***1***) for both spectra is shifted to a lower frequency due to the decrease of the effective medium velocity in porous structure. For 50% porosity AAO, in addition to mode (***1***), two new modes (***2***) and (***3***) corresponding to the higher order propagation bands of the phononic crystal were observed. Moreover, Figure 6.3(d) and (e) show the VV spectra of solid PEO-filled AAO with porosities of 23% and 50%, respectively, which were recorded at $q_\perp$ = 0.0167 nm^{-1} and $q_\perp$ = 0.21 nm^{-1} along ΓX and ΓJ. There are three modes present in the spectra. The peak appearing at a frequency of 5 GHz in Fig. 6.3(d) is attributed to a bulk PEO layer located on the surface of the AAO. A small additional shift of the longitudinal mode (***1***) to a lower frequency was observed for both samples, while the high propagation bands (***2***) and (***3***) were also observed. All spectra in Fig. 6.3 were fitted with either a single or a multiple Lorentzian model. The individual colored line shows the spectral components and red lines show the superposition of different spectral components, showing the change in the phononic properties as the nature of the infiltrate material is changed.

The experimentally measured phonon dispersion relations superposed onto the theoretical phonon dispersion diagrams of air- and both solid and liquid PEO-filled AAO are shown in Fig. 6.4. We plot the experimental data according to the actual scattering angle and superpose onto the theoretical dispersion relations that are plotted in the reduced Brillouin zone. The theoretical phonon dispersion relations are in good agreement with the experimentally measured phonon dispersion relations. All phonon dispersion relations were measured in the VV geometry, except the lowest propagation bands, which indicate the transverse modes measured in the VH geometry. The phononc dispersion relations shown in Fig. 6.4 represent different behaviors of elastic wave propagations in hypersonic crystals based on AAO. The bending of the first propagation band occurs at the same frequency for AAO infiltrated with both liquid- and solid-phase PEO, which approaches asymptotically to 7 GHz and 10 GHz for liquid and solid PEO-filled AAO with a porosity of 23%. For a porosity of 50%, three propagation bands occur at 5 GHz and 6.5 GHz for liquid and solid PEO-filled AAO, regardless of the propagation direction. This is attributed to the fact that the elastic wave is localized in the nanopores. Figure 6.5 shows the same theoretical band structure of in-plane phononic dispersion relations as Fig. 4.9, and the map of the distributions of the displacement field belonging to mode **E**. Figure 6.5s(b) and (c) indicate that the elastic wave of the second propagation band is essentially localized inside the pores. This is the general propertiy of the elastic waves of multiple

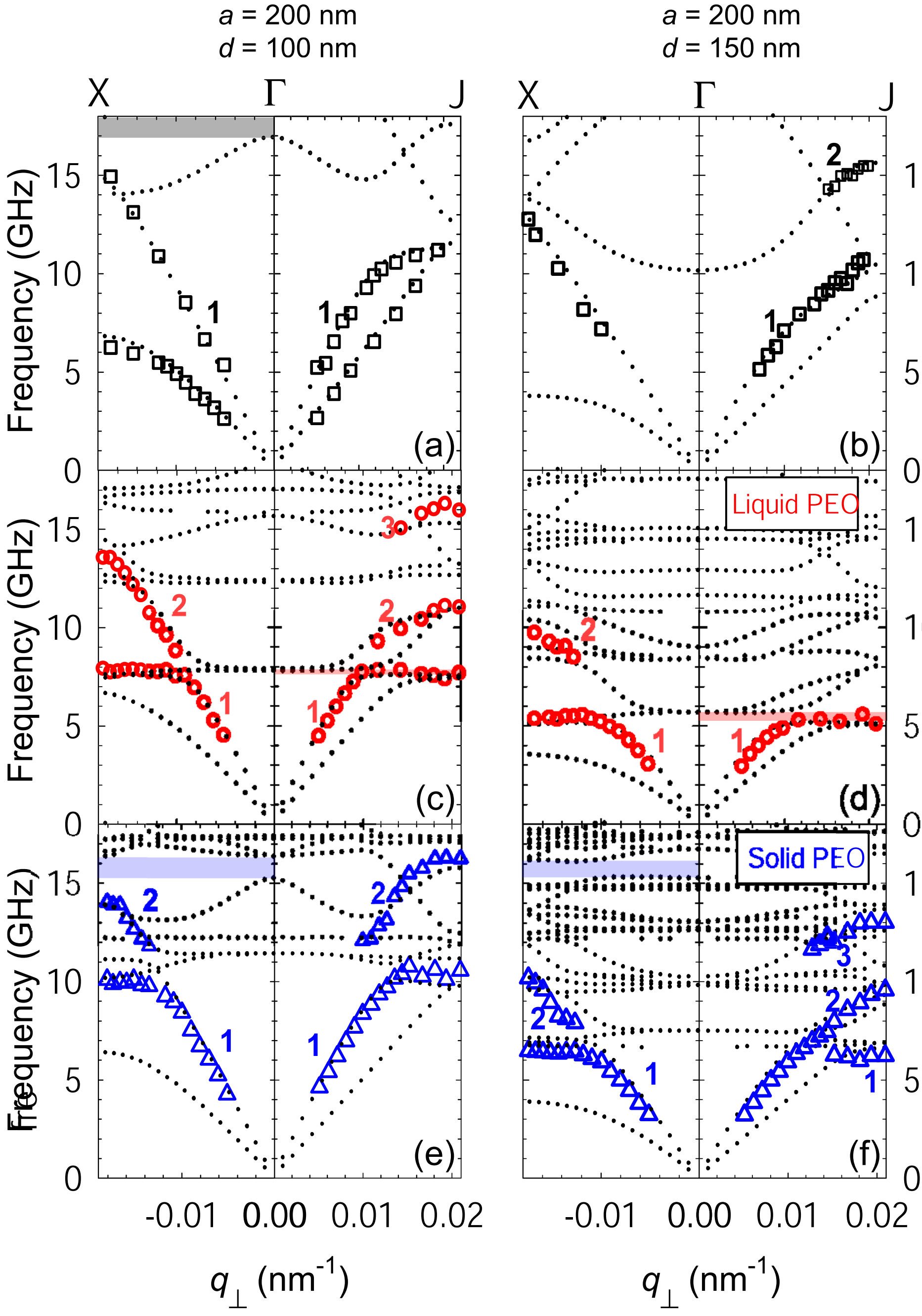

Figure 6.4.: Phonon dispersion relations. Superposed experimental and theoretical phonon dispersion relations along ΓX and ΓJ directions, respectively, for air-filled AAO with (a) 23% and (b) 50% porosity, liquid-filled AAO with (c) 23% and (b) 50% porosity and solid PEO-filled AAO with (e) 23% and (f) 50% porosity. Black dots represent theoretical dispersion relations in all cases, while open black squares, red circles and blue triangles represent experimental dispersion relations.

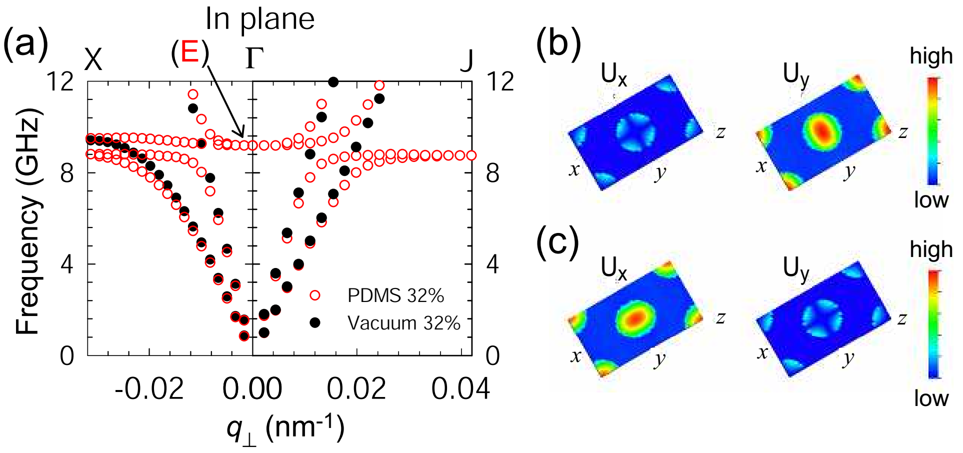

Figure 6.5.: (a) Theoretical band structures of in-plane phonon dispersion curves in AAO (a = 100 nm; d = 60 nm). (b), (c) Map of the distributions of the displacement U of the eigenmodes inside an AAO unit cell belonging to mode **E** located on the second propagation band in (a).

Table 6.1.: Experimental effective medium velocities c_{eff} for the "*in-plane*" longitudinal phonon propagation along both ΓX and ΓJ.

sample	infiltrate	ΓX c_{eff} (m/s)	ΓJ c_{eff} (m/s)
p = 23%	air	5840	5880
	liquid PEO	5330	5300
	solid PEO	5320	5550
p = 50%	air	4540	4470
	liquid PEO	3715	3570
	solid PEO	3930	3930

higher order propagation bands when the pores are filled with polymers.

In air- and PEO-filled AAO hypersonic crystals, one effective longitudinal mode was calculated from the linear dispersion at low q values along both ΓX and ΓJ directions. Each effective medium velocity is summarized in Table 6.1. It was found that infiltrating AAO with PEO leads to a decrease in the effective medium velocity, which is associated with the decrease of the elastic modulus due to a phase transition. As discussed in chapter 5, when AAO is infiltrated with solid materials, the effective medium velocity slightly increases compared to that of air-filled AAO. However, the solid PEO-filled AAO system shows a decrease in the effective medium velocity. This indicates that PEO is not completely crystallized from the melt. Surface and confinement effects of crystallization of PEO have been widely investigated. Differential scanning calorimetry (DSC)[184, 185] revealed that nanoparticles fillers such as silica and alumina suppress the crystallization of PEO. This effect is attributed to the high surface area of the nanoparticles and to the Lewis acid nature of the fillers that prevents PEO chain reorganization. The interaction between PEO and silica nanoparticles in the melt phase leads to less crystallization or the adsorption of amorphous PEO on the silica surface. Moreover, the larger surface area per unit volume increases the interaction between polymer chain and alumina nanoparticles, thus resulting in the restriction of the segmental chain motion of PEO.[184] In addition, lower crystallinity of PEO in the nanopores has been observed.[186] Consequently, the suppression of PEO crystallization in nanopores of AAO contributes to a decrease of the effective medium velocity of solid PEO-filled AAO.

6.4. Formation of complete hypersonic phononic bandgap

The complete phonon dispersion relations of air- and PEO-filled AAO were experimentally and theoretically examined in order to demonstrate qualitatively the complete phonon dispersion relations tuned by the nature of the infiltrate materials. Although partial bandgaps were observed along either ΓX or ΓJ for both air- and PEO-filled AAO, a complete bandgap was not formed. These results indicate that the elastic contrast between AAO (c_l = 7300 m/s) and PEO (c_l = 2050 m/s and c_l = 1500 m/s for solid and liquid phase, respectively) is still high. According to the theoretical dispersion relations of PDMS-filled AAO as shown in Fig. 4.9, a complete band gap is formed. Therefore, PDMS is considered to be the most appropriate infiltrate material for forming the phononic bandgap in hypersonic phononic crystals based on AAO.

Figure 6.6 shows the BLS spectra recorded at $q_\perp$ = 0.0181 nm^{-1} and $q_\perp$ = 0.021 nm^{-1} along ΓX and ΓJ directions, which correspond to the magnitude of the wavevector at the edge of the first Brillouin zone. There is only a single peak present in both spectra. The red solid line represents the overall fit using a single Lorentzian fit. If bandgap formation occurs, the split of a single peak into double peaks is observed in the BLS spectrum. In practice, all spectra recorded at the whole measured q range from 0.0051 nm^{-1} to 0.021 nm^{-1} showed only a single peak.

Figure 6.7 shows the experimentally measured phonon dispersion relations of PDMS-filled AAO (a = 200 nm; d = 100 nm; p = 23%) superposed onto the theoretical phonon dispersion relations along both ΓX and ΓJ directions. Black dots indicate the theoretical dispersion relations, while open red circles indicate the experimental dispersion relations. The effective medium velocity c_{eff} at long wavelengths is 5620 m/s and 5630 m/s along ΓX and ΓJ direction, respectively. The theoretical phonon dispersion relations shows the formation of narrow bandgap with flat lower bands, which indicates the existence of localized modes (Fig. 4.10(c)). This complete phononic bandgap occurs at around 5 GHz with a width about 0.1 GHz, which is indicated by red region. In addition, the bandgap is the same essentially at any q inside the Brillouin zone. The theoretical phonon dispersion relations are in good agreement with the experimentally measured phonon dispersion relations. However, the bandgap width is so narrow that it is difficult to resolve the split characteristic of BLS spectrum and a few measurement

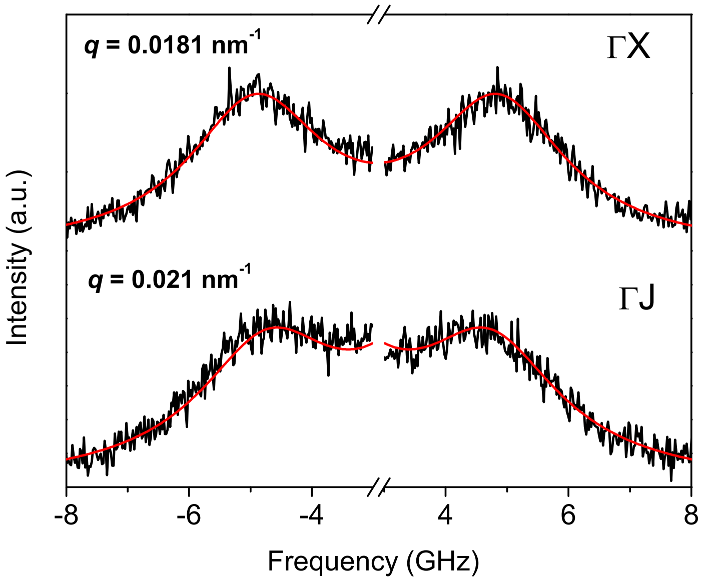

Figure 6.6.: BLS spectra recorded at $q_\perp = 0.0181$ nm^{-1} and $q_\perp = 0.021$ nm^{-1} along ΓX and ΓJ directions correspond to the edge of the first Brillouin zone.

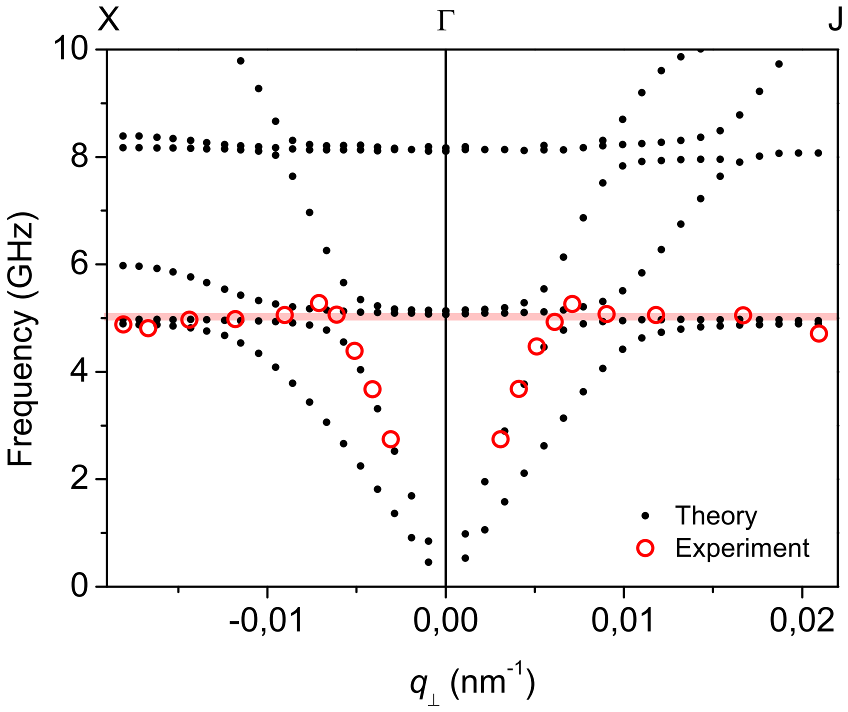

Figure 6.7.: Dispersion relations of PDMS-filled AAO with a lattice constant of 200 nm and pore diameter of 100 nm along both ΓX and ΓJ directions.

points are superposed onto the second propagation band.

6.5. Summary

The hypersonic phononic properties of two-dimensional phononic crystals based on highly ordered AAO with a lattice constant of 200 nm were investigated. Ideally ordered AAO fabricated by pre-molding anodization is a monodomain structure allowing for the direction dependent measurement of its phononic dispersion relations. The phononic dispersion relations exhibit the presence of multiple propagation bands, in good agreement with FDTD theoretical dispersion relation calculations. Despite the fact that the elastic contrast between AAO and air is very large, only a partial gap along ΓX direction is expected for hypersonic phononic crystals with a porosity higher than 0.23. Moreover, although a partial gap along either ΓX or ΓJ direction was predicted in both air- and PEO-filled AAO phononic crystals, these partial gaps were not observed experimentally. In contrast to PEO-filled AAO phononic crystals, the phononic dispersion relations of PDMS-filled AAO exhibit the existence of a narrow complete bandgap at around 5 GHz due to the larger elastic contrast between PDMS and AAO, which leads to localized modes in the nanopores. There are some experimental difficulties in observing both hypersonic complete and partial bandgap along high symmetry directions in ideally ordered periodic structure. Nevertheless, the present results indicate the possibility of engineering experimental phonon dispersion relations at GHz frequencies and could suggest applications in tunable optical and acoustic devices.

7. Thesis Conclusion

High frequency mechanical properties and elastic wave propagation behavior in various hypersonic phononic crystals have been investigated using high-resolution Brillouin light scattering (BLS), which is a powerful tool to probe the dispersion relation $\omega(\mathbf{q})$ at submicron scale. Since BLS is based on inelastic scattering of the incident laser beam thermally excited phonons propagating through a medium, Brillouin spectroscopic characterization of the phonon dispersion relation at hypersonic frequency and elastic properties in confined geometries has a number of features. At least besides BLS, pump-probe technique has been used as a tool to probe the phonon dispersion relation in nanostructures. Of course, this is not to say that everything can be revealed by BLS. Therefore, it is necessary to examine from various angles.

The field of *phononics* is just emerging, and it is important to identify the fundamental concept and rules that govern the behavior of these materials, as well as to hypothesize about their potential applications. There are several works that BLS has been employed to reveal the presence of a hypersonic phononic bandgap and the propagation behavior of elastic waves. However, as identified in this thesis, there have been no previous cases in which anodic aluminium oxide (AAO) is systematically shown to have a crucial role as rigid hypersonic phononic crystals in engineering the phononic properties at hypersonic frequencies. For instance, the investigation of reversible switching of phononic properties in the response to temperature investigated in Chapter 5 would be hardly performed in polymer based hypersonic phononoic crystals due to limited thermal stability. Moreover, the study of the effect of large elastic contrast on the dispersion relations characteristics can be best realized in AAO structures due to the very high intrinsic elastic contrasts of the AAO scaffold.

In Chapter 1, the research background of this thesis was described. Basic research to seek complete phononic bandgaps in sonic and ultrasonic regime and the background of hypersonic phononic crystals were described. Although the fabrication of phononic structure should be, in view of the available knowledge, a straightforward procedure, it is, nevertheless, still missing. This is due to the requirement imposed on a number of materials physical quantities including the density ratio ρ_h/ρ_i, the velocities ratio c_{lh}/c_{li} and c_{th}/c_{ti}, and the ratio of the transverse to the longitudinal velocity ratio c_{th}/c_{lh} and c_{ti}/c_{li}.[1] Moreover, for hypersonic phononic crystals, one must consider the possibility that the values of these quantities in nanostructured composites might differ from their bulk values. I hope this thesis will become part of research on hypersonic phononic crystals from the view point of experimental science.

In Chapter 2, the analytical method of finite difference time domain (FDTD) and the measurement technique of BLS were described.

---

[1] h denotes the host material, while i denotes the inclusion material.

In Chapter 3, the formation mechanism, properties and fabrication methods of AAO as a building block for hypersonic phononic crystals were described. It was shown that porous structures and the geometrical regularity of the pore arrangement critically depends on parameters such as applied voltage, type of acid electrolyte and pre-treatment.

In Chapter 4, phononic properties of hypersonic phononic crystals based on poly(dimethyl siloxane) (PDMS)-filled AAO were investigated as a function of nanopore diameter d. Increasing d results in an enhancement of bending of the propagation band due to the presence of a confined mode inside PDMS cylinders, which leads to the interaction of longitudinal and transverse modes for the "*in-plane*" phonon propagation. On the other hand, separate elastic waves propagating in AAO and PDMS cylinders with different sound velocities were observed for the "*out-of-plane*" phonon propagation. Moreover, PDMS forms a thin solid layer in the proximity of the pore walls, which causes a localized phononic mode in the so-called PDMS interphase layer. These phenomena are attributed to the surface confinement effects of PDMS, structural anisotropy and are rationalized by FDTD calculations with the spatial distribution of the elastic field within the PDMS/AAO composite.

In Chapter 5, tuning and switching of hypersonic phononic properties by varying the elastic contrast between AAO and infiltrate materials were investigated. For the "*in-plane*" phonon propagation, particular features of elastic-contrast nanocomposites, including phonon localization and anisotropy, were shown to depend on the varying elastic contrast between the rigid and the soft components. Namely, the bending of the longitudinal mode (***1***) was observed as the elastic contrast between AAO and infiltrate materials became larger, thus leading to a significant degree of phonon localization in the infiltrate material located in the pores. In contrast, for the "*out-of-plane*" phonon propagation, the phonon dispersion relations associated with the crystallization of infiltrate materials indicate the presence of the transverse mode (***4***) and the longitudinal mode (***5***), which do not change significantly when the infiltrate material residing in the nanopores transforms from solid to liquid.

In Chapter 6, complete phonon dispersion relations in hypersonic phononic crystals based on highly ordered AAO were investigated. Ideally ordered AAO phononic crystals fabricated by pre-molding anodization allowed for the direction dependent measurements of their phononic dispersion relations. We observed experimentally the presence of multiple propagation bands and demonstrated the tunability of complete phononic dispersion relations in response to changes in temperature in PEO-filled AAO. The FDTD calculations are in good agreement with the experimental phonon dispersion relations. In addition, the FDTD calculations indicated that a mid-contrast PDMS/AAO phononic crystal shows a narrow complete bandgap. However, regardless of the contrast between AAO and infiltrate material, phononic crystals based on AAO show a partial gap along either the ΓX or the ΓJ direction in the first Brillouin zone. As such, PDMS/AAO hypersonic phononic crystals with different pore geometries may be possibly suitable as complete hypersonic phononic bandgap materials.

8. Future research

The main result of this thesis is the understanding of elastic wave propagation behavior in nanocomposite media based on a rigid matrix, i.e. self-ordered anodic aluminium oxide (AAO) in the hypersonic (GHz) frequency regime. This thesis develops solid foundations of engineering hypersonic phononic properties in periodic nanocomposites.

AAO has great potential for the development of hypersonic phononic crystals since it takes advantage of the large elastic contrast possible between the AAO scaffold and the infiltrate materials located in the nanopores. However, from a theoretical point of view, we still need to recognize the ideal AAO-based phononic structures, which have the large phononic bandgap for a given contrast in mechanical properties of materials. Although air/AAO hypersonic phononic crystals have a huge contrast, only partial bandgaps were predicted along the ΓX direction. On the other hand, PDMS/AAO hypersonic phononic crystals reveal the presence of complete bandgaps but the width of phononic bandgaps are extremely narrow. Other fluid infiltration materials with sound velocities is faster than 1200 m/s, e.g. poly(ethylene glycol), tetracosane, poly(ethylene oxide) and so on, are shown to be unable form no complete phononic bandgaps. A possible step towards forming a complete phononic bandgap in AAO-based hypersonic phononic crystals is using AAO with a larger lattice constant or with different pore shapes, such as triangular, square or hexagonal shapes.

There is also a variety of interesting subjects for the experimental study of hypersonic phononic crystals. Demonstration and monitoring of the change in the properties of an interphase layer would be a methodological extension of the study described in this thesis. A number of methods such as NMR, dielectric relaxation spectroscopy, quasielastic neutron scattering and X-ray reflectivity, have been used to investigate the effect of local properties on both polymer conformation and dynamics.

In chapters 4 and 5 We have demonstrated the surface-induced interphase mode for PDMS-, PEG- and $C_{24}H_{50}$-filled AAO. The properties of this interphase mode can be tuned by the modulation of local elastic properties associated with the interaction between polymers and pore walls. For example, it was found that the property of interphase polyisoprene (PI, M_w = 2500 g/mol) layer changes with time after infiltration of PI into the nanopores. Figure 8.1 shows the BLS spectra for both the "*in-plane*" and the "*out-of-plane*" phonon propagation right after infiltration of PI (black, PI-0) and 14 days after infiltration of PI (red, PI-14). The BLS spectra in Fig. 8.1(a) show two modes which are assigned to the effective medium branch (***1***) and the flat interfacial mode (***2***) at $q_\perp \leq 0.008$ nm^{-1}, while at higher $q_\perp$ an additional lower frequency mode PI is ascribed to the bulk PI layer remaining on the AAO surface. All resolved modes besides mode (***1***) display a blue shift after 14 days. The fact that the sound velocity of the PI modes increased from 2180 m/s to 2790 m/s over time, in contrast to the constant PEG

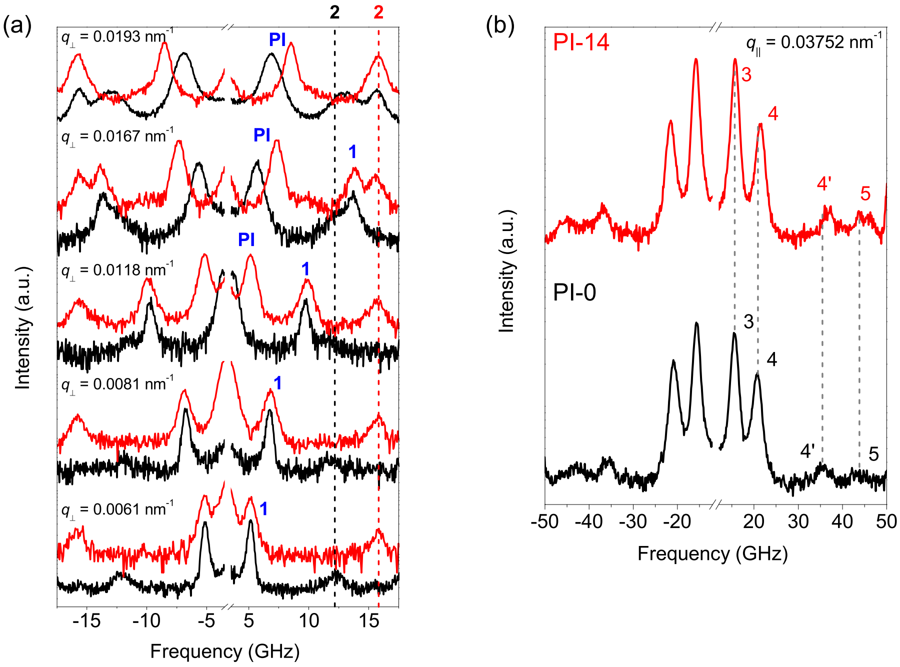

Figure 8.1.: (a) BLS spectra of AAO infiltrated with PI at five different "*in-plane*" $q_\perp$ values for both PI-0 (black) and PI-14 (red). Black and red dashed lines represent the corresponding frequency of the flat mode ***2***. (b) BLS spectra of AAO infiltrated with PI at the same "*out-of-plane*" $q_{||}$ value for both PI-0 (black) and PI-14 (red).

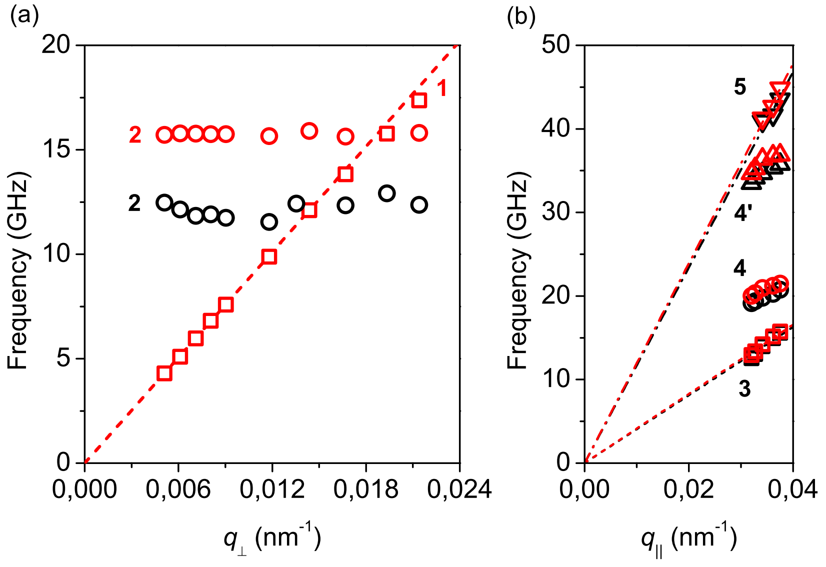

Figure 8.2.: Phonon dispersion relations of (a) "*in-plane*" ($q_\perp$) and (b) "*out-of-plane*" ($q_{||}$) phonon propagation. Black and red symbols represent dispersion relations for PI-0 and PI-14, respectively.

mode in Fig. 5.3(a), suggests the strong surface-induced hardening of the PI layer. Consistent with this finding is the increase of the frequency f_i of the flat mode (2) from 12 GHz to 16 GHz after 14 days (Fig. 8.2). Note also that this mode (***2***) is much stronger in PI-filled AAO than in PEG-filled AAO, since it has a comparable intensity with the effective medium mode (***1***) (cf. Fig. 5.3(a) and 8.1(a)). The sound velocity for the "*in-plane*" propagation obtained from the acoustic branch (***1***) is 5280 m/s, which is virtually independent of aging. In addition, the "*out-of-plane*" phononic properties were modified as shown in Fig. 8.1(b), indicating a small shift of all the resolved modes. The origin of this PI hardening is not yet understood. However, since the pore wall of the AAO scaffold is a highly reactive surface, PI might be cross-linked to the pore walls. This could induce a rigid layer in the proximity of the pore walls.

FDTD calculations can capture this flat mode using a model in which the presence of a thick solid interphase layer in the proximity of the pore walls, as demonstrated in chapter 4. These flat modes (***2***) are sensitive to the transverse velocity c_t and to the thickness of the interphase layer. Although there are some technical difficulties in obtaining both c_t and the thickness of the interphase layer, it is possible to assume a reasonable thickness of the monomer-scale films by a combination of BLS and the FDTD method. Moreover, the polymer end groups also affect the interaction between the polymer and the pore walls. Therefore, hypersound phononics has a potential for the characterization of interphase layers, which is complementary to NMR since nanocomposite systems are not suitable for NMR experiments, and since the amount of sample material required for BLS is significantly lower.

Another interesting subject for experimental studies of hypersonic phononic crystals is the enhancement of phononic properties of AAO nanocomposites. In chapter 5, the phononic properties of AAO infiltrated with solid materials tetracosane ($C_{24}H_{50}$) and poly(vinylidene fluoride) (PVDF) are studied. When AAO was infiltrated with both $C_{24}H_{50}$ and PVDF, the effective medium velocity increased up to ≈10∼12% compared to air-filled AAO. However, if AAO was infiltrated with poly(vinylidenefluoride-trifluorethylene) (P[VDF-TrFE]), there is a much larger increase in the effective medium velocity.

Figure 8.3 shows some preliminary results on P[VDF-TrFE]-filled AAO with a pore diameter of 60 nm and a lattice constant of 100 nm. Figure 8.3(a) shows both polarized (VV) and depolarized (VH) BLS spectra of P[VDF-TrFE]-filled AAO recorded at $q_\perp$ = 0.0167 nm^{-1}. Although the BLS intensity is very weak due to the low compressibility of the composite system, there is one mode observed for both VV and VH polarizations, corresponding to the longitudinal and the transverse mode. The phonon dispersion relations $\omega(\mathbf{q})$ for for the "*in-plane*" and the "*out-of-plane*" phonon propagation in P[VDF-TrFE]-filled AAO are shown in Fig. 8.3(b) and (c). The most intriguing finding is that the effective medium velocity of longitudinal and transverse mode increased from 5370 m/s to 6870 m/s and from 2950 m/s to 3810 m/s, respectively, which correspond to a ≈28% increase after infiltrating P[VDF-TrFE] into the nanopores (Table 8.1). Moreover, these values are very close to those of bulk AAO.

Ferroelectric polymers such as PVDF and P[VDF-TrFE] are promising materials for various ultrasonic transducer applications due to their strong piezoelectric and pyroelectric activities. In particular, recent improvement of crystallization techniques improves crystallinity of

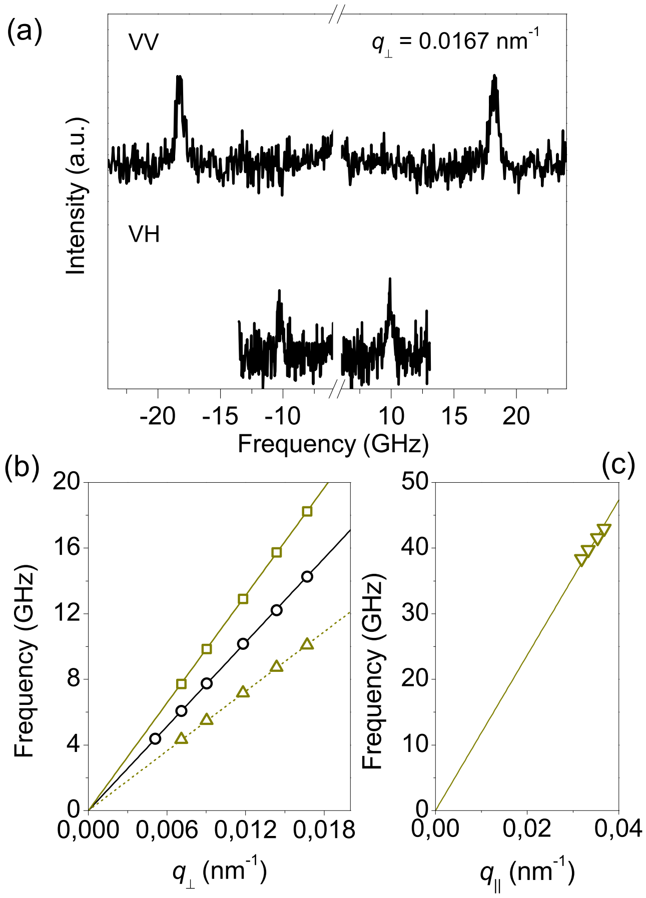

Figure 8.3.: (a) Polarized and depolarized Brillouin spectrum of P[VDF-TrFE] recorded at $q_\perp$ = 0.0167 nm^{-1}. The phonon dispersion relations of (a) the "*in-plane*" and the "*out-of-plane*" phonon propagation in P[VDF-TrFE]-filled AAO. The phonon dispersion relations (b) for the "*in-plane*" and (c) for the "*out-of-plane*" phonon propagation. The black and dark yellow lines represent the dispersion relations for longitudinal mode in air- and P[VDF-TrFE]-filled AAO, while corresponding dashed line represents the dispersion relation for transverse mode in P[VDF-TrFE]-filled AAO.

Table 8.1.: Effective medium velocities in air- and P[VDF-TrFE]-filled AAO.

Material	Longitudinal	Transverse	ΓZ
air	5370	2950	6910
P[VDF-TrFE]	6870	3810	7435

P[VDF-TrFE], thus resulting in a large piezoelectric response. The ferroelectric-paraelectric phase transition of P[VDF-TrFE] occurs at T_c = 127 °C during heating and T_c = 127 °C upon cooling, while P[VDF-TrFE] melts at T_c = 149 °. Therefore, polymer chain arrangements of P[VDF-TrFE] can be tuned by the phase transition. Moreover, polymer chain arrangements of P[VDF-TrFE] can also be changed by poling. Consequently, P[VDF-TrFE]/AAO hybrid system has a promising platform for the design of tunable and switchable hypersonic phononic structures.

A. Appendix

A.1. Scattering vector calculation

When the scattering wavevector **q** is calculated for both the transmission and the reflection geometries in the case of a film, **q** as a function of the scattering angle is essentially obtained from Snell's law at each boundary and the trigonometric operations. Figure A.1 shows both the transmission and the reflection geometries for the scattering wavevector calculation.

A.1.1. in-plane

Consider the scattering wavevector for the transmission geometry shown in Fig. A.1(a). Let the incident and the refraction at the air/film boundary be respectively α and β, while γ and δ at the film/air boundary, respectively. Geometrically, the real scattering angle Θ and the refraction angle γ at the second boundary can be expressed as

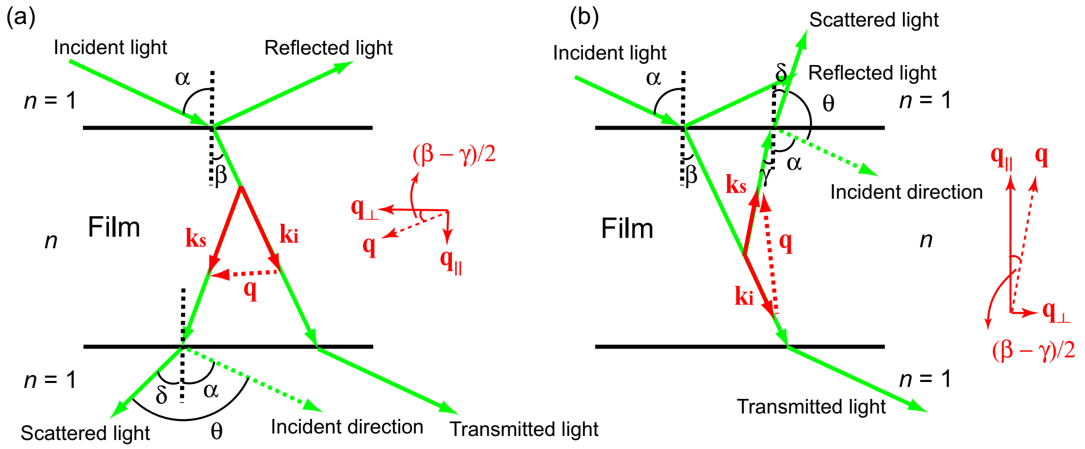
(a)
Incident light
Reflected light
α
n = 1
β
Film
n
ks
ki
q
(β – γ)/2
q⊥
q
q∥
n = 1
δ
α
θ
Scattered light
Incident direction
Transmitted light
(b)
Incident light
Scattered light
Reflected light
α
δ
θ
n = 1
β
γ
α
ks
Film
q
Incident direction
n
ki
q∥
q
q⊥
(β – γ)/2
Transmitted light
n = 1

Figure A.1.: Schematics of the scattering geometry: (a) transmission geometry and (b) reflection geometry.

$$\Theta = \beta + \gamma \tag{A.1}$$

$$\delta = \theta - \alpha \tag{A.2}$$

According to Snell's law, the refraction angle β and the incident angle γ can be expressed as

$$\beta = \sin^{-1}\left(\frac{1}{n}\sin\alpha\right) \tag{A.3}$$

$$\gamma = \sin^{-1}\left(\frac{1}{n}\sin\delta\right) = \sin^{-1}\left\{\frac{1}{n}\sin(\theta-\alpha)\right\} \tag{A.4}$$

The real scattering angle Θ is expressed from Equations A.1, A.3 and A.4 as

$$\Theta = \beta + \gamma = \sin^{-1}\left(\frac{1}{n}\sin\alpha\right) + \sin^{-1}\left\{\frac{1}{n}\sin\left(\theta-\alpha\right)\right\} \tag{A.5}$$

Consequently, the scattering wavevector *q* becomes

$$q = \frac{4\pi n}{\lambda}\sin\left(\frac{\Theta}{2}\right) = \frac{4\pi n}{\lambda}\sin\left[\frac{1}{2}\left\{\sin^{-1}\left(\frac{1}{n}\sin\alpha\right) - \sin^{-1}\left\{\frac{1}{n}\sin(\theta-\alpha)\right\}\right\}\right] \tag{A.6}$$

The perpendicular component of the scattering wavevector $q_\perp$ is then expressed as

$$q_\perp = q\cdot\cos\left(\frac{\beta-\gamma}{2}\right) = q\cos\left[\frac{1}{2}\left\{\sin^{-1}\left(\frac{1}{n}\sin\alpha\right) - \sin^{-1}\left\{\frac{1}{n}\sin(\theta-\alpha)\right\}\right\}\right] \tag{A.7}$$

Therefore, the final form of the scattering wavevector $q_\perp$ for the "*in-plane*" is expressed from Equations A.6 and A.7 as

$$\begin{aligned} q_\perp = \frac{4\pi n}{\lambda}&\sin\left[\frac{1}{2}\left\{\sin^{-1}\left(\frac{1}{n}\sin\alpha\right) + \sin^{-1}\left\{\frac{1}{n}\sin(\theta-\alpha)\right\}\right\}\right] \\ &\times\cos\left[\frac{1}{2}\left\{\sin^{-1}\left(\frac{1}{n}\sin\alpha\right) - \sin^{-1}\left\{\frac{1}{n}\sin(\theta-\alpha)\right\}\right\}\right] \end{aligned} \tag{A.8}$$

For the transmission geometry, when $\alpha = \theta/2$, namely the incident angle is half of the scattering angle,

$$q_\perp = \frac{4\pi n}{\lambda}\sin\left[\sin^{-1}\left(\frac{1}{n}\sin\frac{\theta}{2}\right)\right] \tag{A.9}$$

A.1.2. out-of-plane

Consider the scattering wavevector for the reflection geometry as shown in Fig. A.1(b). Unlike the transmission geometry, light incident on the upper boundary is only considered. As is the case with the transmission geometry, let the incident and the refraction at the air/film boundary be respectively α and β, while γ and δ at the film/air boundary, respectively. Geometrically, the real scattering angle Θ and the refraction angle γ at the second boundary can be expressed as

$$\Theta = \pi - \beta + \gamma \tag{A.10}$$

$$\delta = \pi - \theta - \alpha \tag{A.11}$$

According to Snell's law, the refraction angle β and the incident angle γ can be expressed as

$$\beta = \sin^{-1}\left(\frac{1}{n}\sin\alpha\right) \tag{A.12}$$

$$\gamma = \sin^{-1}\left(\frac{1}{n}\sin\delta\right) = \sin^{-1}\left\{\frac{1}{n}\sin(\theta+\alpha)\right\} \tag{A.13}$$

Consequently, the scattering wavevector *q* becomes

$$q = \frac{4\pi n}{\lambda}\sin\left(\frac{\Theta}{2}\right) = \frac{4\pi n}{\lambda}\cos\left[\frac{1}{2}\sin^{-1}\left(\frac{1}{n}\sin\alpha\right) + \frac{1}{2}\sin^{-1}\left\{\frac{1}{n}\sin(\theta+\alpha)\right\}\right] \tag{A.14}$$

The parallel component of the scattering wavevector $q_{\|}$ is then expressed as

$$q_{\|} = q\cdot\cos\left(\frac{\beta-\gamma}{2}\right) = q\cdot\cos\left[\frac{1}{2}\sin^{-1}\left(\frac{1}{n}\sin\alpha\right) - \frac{1}{2}\sin^{-1}\left\{\frac{1}{n}\sin(\theta+\alpha)\right\}\right] \tag{A.15}$$

Therefore, the final form of the scattering wavevector $q_{\|}$ for the "*out-of-plane*" is expressed from Equations A.14 and A.15 as

$$\begin{aligned} q_{\|} = \frac{4\pi n}{\lambda}&\cos\left[\frac{1}{2}\sin^{-1}\left(\frac{1}{n}\sin\alpha\right) + \frac{1}{2}\sin^{-1}\left\{\frac{1}{n}\sin(\theta+\alpha)\right\}\right] \\ \times&\cos\left[\frac{1}{2}\sin^{-1}\left(\frac{1}{n}\sin\alpha\right) - \frac{1}{2}\sin^{-1}\left\{\frac{1}{n}\sin(\theta+\alpha)\right\}\right] \end{aligned} \tag{A.16}$$

A.2. Relation between the dispersion relations and lattice constants

Theoretically, the bending of the acoustic branch (***1***) occurs at the intersection with the flat band confined to the PDMS cylinders (**B** in Fig. 4.9(a) and 4.10(c)) and hence its frequency should depend only on the pore diameter *d* and on the porosity of the AAO scaffold. In fact, the frequency at which mode (***1***) bends should increase from 5.9 GHz to 14.5 GHz when the pore diameter decreases from 85 nm to 35 nm. As already mentioned, the bending is not observed for the narrowest nanopores. Alternatively, the theory(**C** in Fig. 4.9(b) and Fig. A.5) correctly predicts the insensitivity of the frequency of mode (***3***) to the pore diameter (Fig. 4.7(b)) for AAO containing PDMS. In order to verify the effect of the lattice constant on the phononic behavior and to elucidate the origin of the bending of the acoustic mode (***1***) and the flat branch

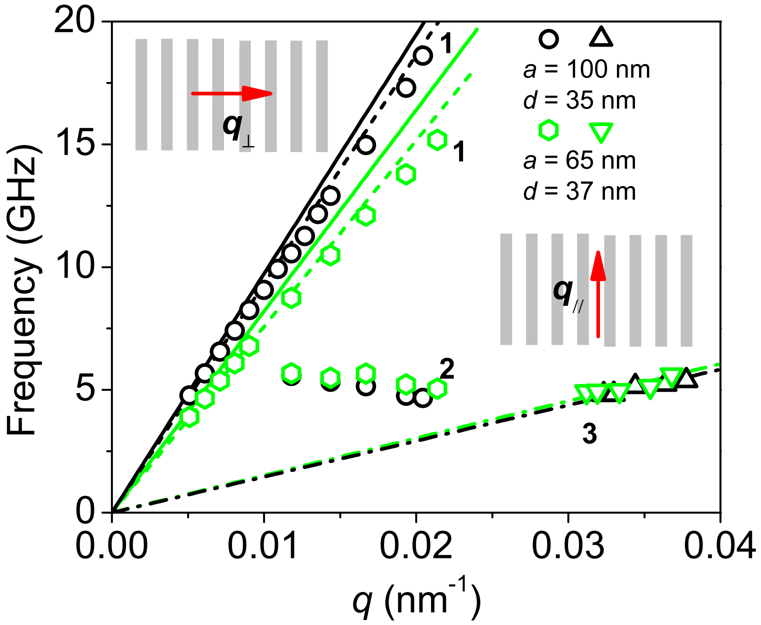

Figure A.2.: Dispersion relations for "*in-plane*" ($\mathbf{q}_\perp$) and "*out-of-plane*" ($\mathbf{q}_\parallel$) longitudinal phononic modes (***1* - *3***) in AAO containing PDMS with a = 65 nm and p = 30% (green symbols) as well as a = 100 nm and p = 11% (black symbols). The solid lines represent the dispersion relations for the corresponding air-filled AAO.

(***2***), we compared the dispersion relations in two AAO membranes with very similar pore diameter ($d \approx$ 35nm) but two different lattice constants and porosities (a = 65 nm, p = 30% and a = 100 nm, p = 11%) in Fig. A.2.

Mode (***1***) displays only a weak deviation from the pure acoustic slope in both AAO architectures (dashed lines in Fig. A.2), i.e. the lack of a clear bending does not depend on lattice constant and porosity; the latter affects only the effective medium sound velocity (Table 4.3). This finding corroborates the notion that the apparent discrepancy with the theory might arise from the modified elastic properties of PDMS cylinders residing in sufficiently narrow nanopores (≈35 nm) with a high surface-to-volume ratio, within which the impact of the PDMS/pore wall interface on the mode (***1***) should be significant. On the other hand, the acoustic branch (***3***) for the "*out-of-plane*" propagation is found to be insensitive to the lattice constants and pore diameters over the examined range in agreement with the theoretical predictions, suggesting that the longitudinal sound velocity of the PDMS residing in the nanopores remains roughly constant. This is consistent with the fact that mode (***3***) is essentially confined to the PDMS cylinders and does not extend into the AAO scaffold. The flat branch (***2***) is present in all examined AAO irrespectively of the pore size and lattice constant over the examined range.

A.3. Dispersion relations of sapphire

We had discussions on the sound velocities which were evaluated for the theoretical phononic band diagram calculations in chapter 4. Since AAO is described as an amorphous structure, it is necessary to know a sound velocity of an amorphous AAO to fit the experimental data. In fact, it is very difficult to obtain its value due to the difficulty of the preparation of barrier type AAO. Therefore, the extrapolated values from the data shown in Fig. 4.8 was first used for the calculation as the amorphous AAO (p = 0%), which are 6180 m/s and 3740 m/s for the longitudinal and the transverse mode, respectively. However, these values result in a decrease of the "*in-plane*" effective sound velocities in the theoretical phononic band diagram. Consequently, we focused attention on sapphire, which also refers to an aluminium oxide (Al_2O_3), as a reference.

Figure A.3 shows both polarized (VV) and depolarized (VH) BLS spectrum of sapphire recorded at q = 0.0118 nm^{-1}. Since sapphire is a highly single crystal, a distinct single or double doublet were observed. As shown in Fig. A.3, one longitudinal mode was observed, while two transverse modes were observed. Two transverse modes are degenerate along the ΓX direction.

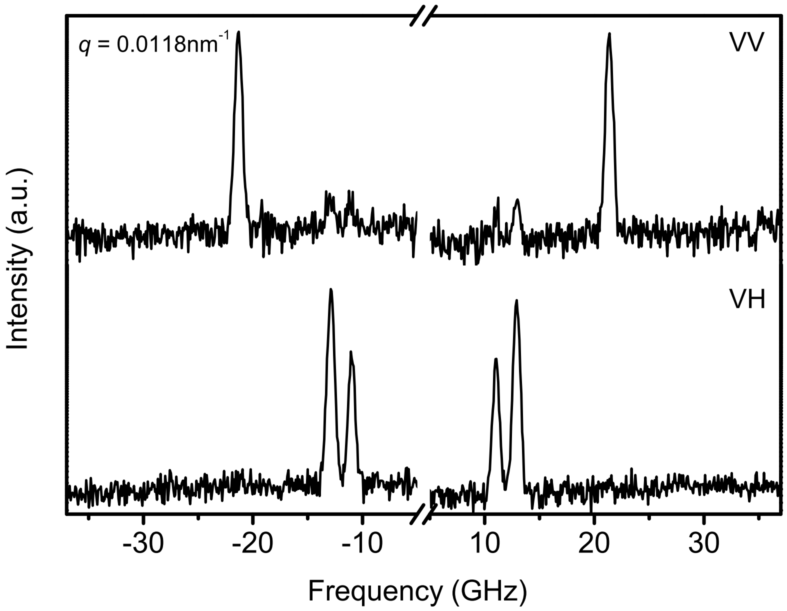

Figure A.3.: Polarized (VV) and depolarized (VH) BLS spectrum of sapphire recorded at q = 0.0118 nm^{-1}.

A more complete knowledge of the phonon propagation can be obtained by referring to the measured dispersion relation $\omega(\mathbf{q})$ as shown in Fig. A.4 in the case of the "*in-plane*" phonon propagation with longitudinal and transverse polarization. Figure A.4 shows the phonon dis-

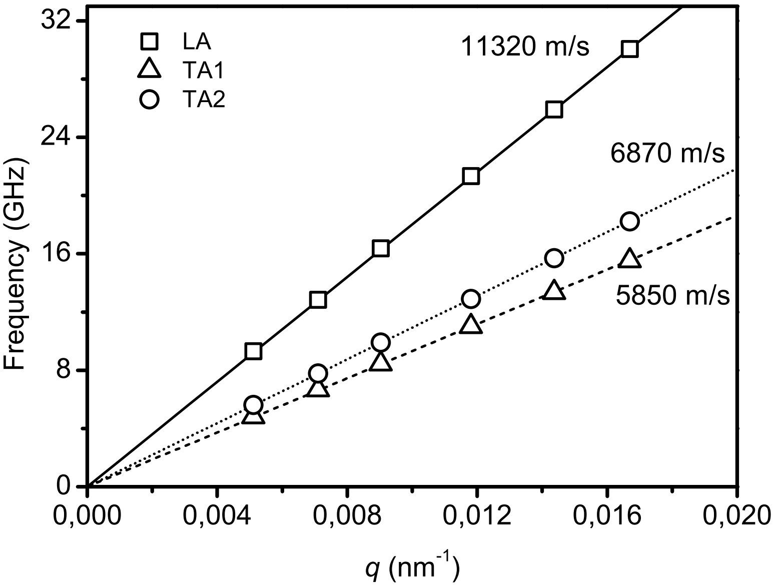

Figure A.4.: Dispersion relations of both longitudinal and transverse modes in sapphire. The black squires, circles and triangles represent the longitudinal and two transverse dispersion relations, respectively, while the corresponding solid, short dotted and short dashed lines represent effective sound velocities.

persion relations of sapphire. The solid line indicates the longitudinal acoustic phonon propagation, while both the dotted and the dashed line indicate the transverse acoustic phonon propagation. The slope of the solid line yields the longitudinal sound velocity c_l of 11320 m/s and the slope of the dotted and the dashed line yields 6870 m/s and 5850 m/s for c_{t1} and c_{t2}, respectively. These values are in good agreement the data obtained from time of flight measurements[187]. However, contrary to extrapolated values, the sound velocities of the longitudinal and two transverse modes are too high to obtain a good fit of the experimental values.

A.4. Theoretical band diagram

In section 4.5, the theoretical band structure only for AAO with the porosity p = 32% was discussed. Here, we also show the theoretical band structure of AAO (p = 65%) infiltrated with PDMS in Fig. A.5.

The calculation was performed in the same way as AAO with p = 32%. When the interphase is introduced in the calculations (with the parameters indicated below) there is no significant changes in the other dispersion curves. Introducing an interphase with totally arbitrary parameters (density, velocities of sound, thickness) will probably change all the results. Nevertheless it appeared that the new mode (***2***) associated with the interphase is mostly sen-

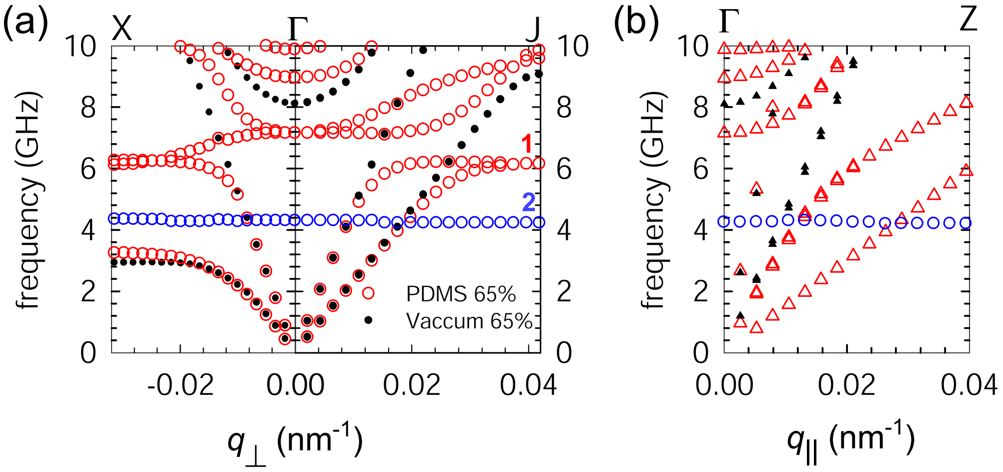

Figure A.5.: Theoretical band structures of both "*in-plane*" (a) and "*out-of-plane*" (b) phononic modes for AAO with porosity 65 %.

sitive to the transverse velocity of sound c_t and to the thickness: the frequency of mode (***2***) increases either by increasing c_t or by decreasing the thickness. Therefore, the thickness was chosen arbitrarily, but in a reasonable physical range, to be a 5 nm and the calculations were performed for different c_t to find the frequency of mode (***2***) in agreement with experiment. The main conclusion is the fact that the frequency of mode (***2***) is mostly sensitive to the thickness and to c_t and these two parameters act in two opposite directions. The frequency of mode (***2***) does not scale with the diameter of the holes although the porosity can slightly affect the result.

A.5. Structural studies on macroscopic ensembles of tetracosane

In order to gain insights into hypersonic phononic properties of tetracosane ($C_{24}H_{50}$), wide-angle X-ray scattering (WAXS) experiments were conducted on $C_{24}H_{50}$-filled AAO samples. As described in chapter 5, $C_{24}H_{50}$ was infiltrated into AAO with a diameter of 60 nm, a lattice constant of 100 nm and 100 μm thick. The wetting of AAO with $C_{24}H_{50}$ was done at 80 °C for 12 hours. For WAXS measurements, surface film of $C_{24}H_{50}$ was removed from the samples.

To analyze the crystal texture of macroscopic ensembles of $C_{24}H_{50}$ nanostructure located inside AAO, WAXS measurements in reflection mode using a Philips X'oert MRD diffractmeter with cradle and secondary monochrometer for Cu K_α was performed. The setup used for WAXS measurements are schematically shown in Fig. 5.6. In this $\Theta/2\Theta$ geometry, Θ denotes the incident angle defined as the angle between the incident beam and the surface of the sample, while 2Θ is defined as the angle between the incident and the diffracted beams.

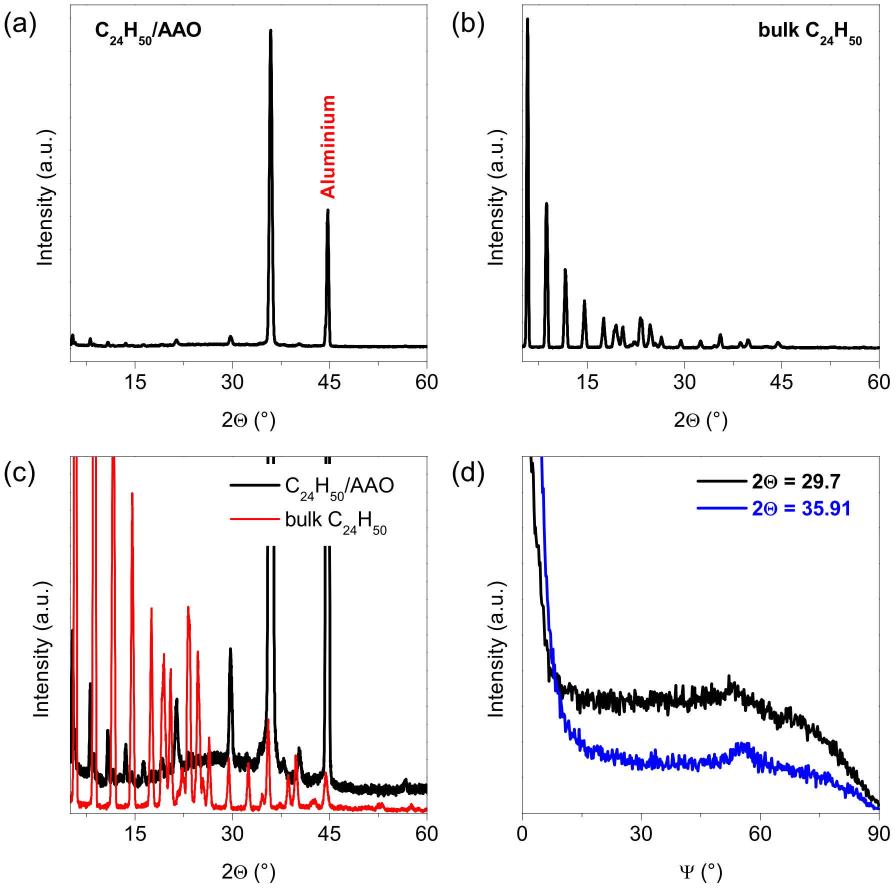

Figure A.6.: XRD analysis of $C_{24}H_{50}$ nanostructure inside AAO. (a) $\Theta/2\Theta$ scan. (b) $\Theta/2\Theta$ scan of bulk $C_{24}H_{50}$. (c) $\Theta/2\Theta$ scan of both bulk $C_{24}H_{50}$ and $C_{24}H_{50}$ nanostructure inside AAO. (d) Ψ scan representing orientation distributions with respect to the AAO surface recorded at $2\Theta = 29.7°$ and 35.9°.

In this geometry, only crystal lattice planes oriented parallel to the surface contribute to the intensity of a Bragg reflection.

The scans were performed in the range of 5° to 60°. Figure A.6(a) shows the XRD pattern of $C_{24}H_{50}$-filled AAO. The Θ-2Θ XRD pattern shows two prominent peaks at 2Θ angles of 35.9° and 44.7°. The 2Θ peak at 44.7° corresponds to aluminium, which is attached to the pore bottoms. However, the origin of the peak observed at 35.9° is still unclear. Furthermore, at lower 2Θ angles, from 5 to 15°, there are many reflections from layered structure of tetracosane (solid black line seen in Fig. A.6(c)). This phenomenon is observed when the *c*-axis is parallel to the pore axis. Figure A.6(b) shows the XRD pattern of bulk $C_{24}H_{50}$. Bulk tetracosane is a complex system where it shows a number of rotator phases. Figure A.6(d) shows Ψ scans measured at the fixed angle of 29.7° and 35.9° shown in Fig. A.6(a). For both systems, the orientation distributions show strong intensity at Ψ = 0°, indicating a preferred orientation of the corresponding lattice planes parallel to the surface of the sample.

$C_{24}H_{50}$ is a rather complex system. A tentative look into these results suggests that we have, in the 60 nm pores, a mixture consisting of orthorhombic C_{24} as major component and of triclinic C_{24} as minor component. The orthorhombic phase does not form in the bulk and was, up to now, only reported by Landfester *et al.*[173]. We can assume that $C_{24}H_{50}$ was actually solid under the conditions applied during the BLS measurements. However, it is expected that we have a pronounced texture, as also reported by Huber *et al.* for similar systems. It is reasonable to assume that phononic band structures are coupled with crystal orientation. Moreover, knowledge of the relevant crystal modification is rather limited so that the overall interpretation of the data is certainly far from being trivial.

A.6. Phonon dispersion relations of highly ordered AAO

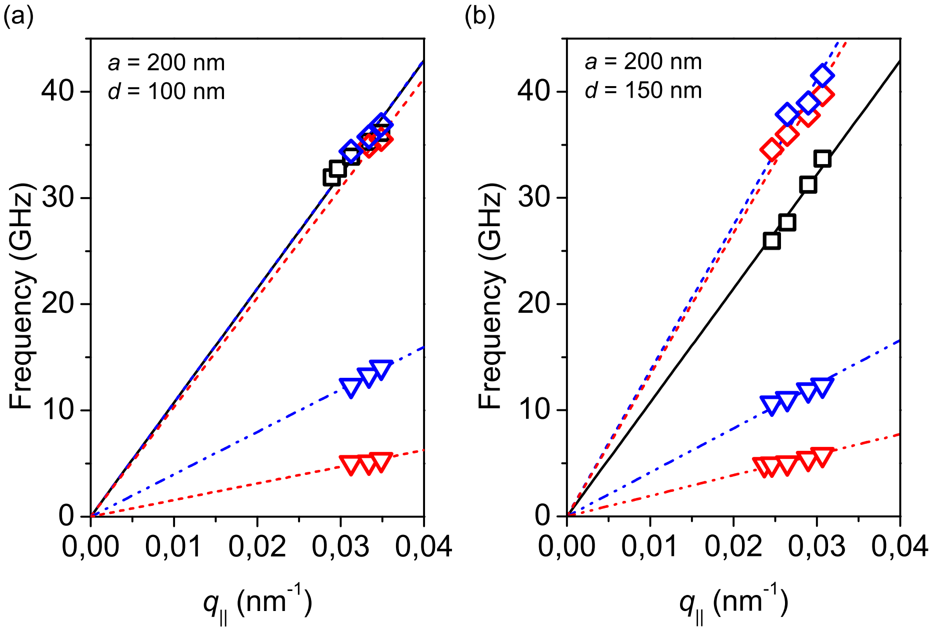

Figure A.7.: (a) Dispersion relations in air- and PEO-filled anodic porous alumina in both ΓX and ΓJ directions for p = 23% porosity. (b) Dispersion relations in air- and PEO-filled anodic porous alumina in both ΓX and ΓJ directions for p = 50% porosity.

References

[1] Bardeen, J. and Brattain, W. H. *Physical Review* **74**(2), 230–231 (1948).

[2] Yablonovitch, E. and Gmitter, T. J. *Physical Review Letters* **63**(18), 1950–1953 (1989).

[3] Yablonovitch, E., Gmitter, T. J., and Leung, K. M. *Physical Review Letters* **67**(17), 2295–2298 (1991).

[4] Sigalas, M. M. and Economou, E. N. *Journal of Sound and Vibration* **158**(2), 377–382 (1992).

[5] Sigalas, M. and Economou, E. N. *Solid State Communications* **86**(3), 141–143 (1993).

[6] Kushwaha, M. S., Halevi, P., Dobrzynski, L., and Djafari-Rouhani, B. *Physical Review Letters* **71**(13), 2022–2025 (1993).

[7] Penciu, R. S., Kriegs, H., Petekidis, G., Fytas, G., and Economou, E. N. *Journal of Chemical Physics* **118**(11), 5224–5240 (2003).

[8] Dhar, L. and Rogers, J. A. *Applied Physics Letters* **77**(9), 1402–1404 (2000).

[9] Martinezsala, R., Sancho, J., Sanchez, J. V., Gomez, V., Llinares, J., and Meseguer, F. *Nature* **378**(6554), 241–241 (1995).

[10] Sanchez-Perez, J. V., Caballero, D., Martinez-Sala, R., Rubio, C., Sanchez-Dehesa, J., Meseguer, F., Llinares, J., and Galvez, F. *Physical Review Letters* **80**(24), 5325–5328 (1998).

[11] Robertson, W. M. and Rudy, J. F. *Journal of the Acoustical Society of America* **104**(2), 694–699 (1998).

[12] Vasseur, J. O., Deymier, P. A., Khelif, A., Lambin, P., Djafari-Rouhani, B., Akjouj, A., Dobrzynski, L., Fettouhi, N., and Zemmouri, J. *Physical Review E* **65**(5), 056608 (2002).

[13] Rubio, C., Caballero, D., Sanchez-Perez, V., Martinez-Sala, R., Sanchez-Dehesa, J., Meseguer, F., and Cervera, F. *Journal of Lightwave Technology* **17**(11), 2202–2207 (1999).

[14] Lambin, P., Khelif, A., Vasseur, J. O., Dobrzynski, L., and Djafari-Rouhani, B. *Physical Review E* **6306**(6), 066605 (2001).

[15] Liu, Z. Y., Zhang, X. X., Mao, Y. W., Zhu, Y. Y., Yang, Z. Y., Chan, C. T., and Sheng, P. *Science* **289**(5485), 1734–1736 (2000).

[16] Cubukcu, E., Aydin, K., Ozbay, E., Foteinopoulou, S., and Soukoulis, C. M. *Nature* **423**(6940), 604–605 (2003).

[17] Parimi, P. V., Lu, W. T. T., Vodo, P., and Sridhar, S. *Nature* **426**(6965), 404–404 (2003).

[18] Parimi, P. V., Lu, W. T., Vodo, P., Sokoloff, J., Derov, J. S., and Sridhar, S. *Physical Review Letters* **92**(12), 127401 (2004).

[19] Berrier, A., Mulot, M., Swillo, M., Qiu, M., Thylen, L., Talneau, A., and Anand, S. *Physical Review Letters* **93**(7), 073902 (2004).

[20] Martinez, A., Miguez, H., Griol, A., and Marti, J. *Physical Review B* **69**(16), – (2004).

[21] Hu, X. H., Shen, Y. F., Liu, X. H., Fu, R. T., and Zi, J. *Physical Review E* **69**(3), 030201 (2004).

[22] Lu, M. H., Zhang, C., Feng, L., Zhao, J., Chen, Y. F., Mao, Y. W., Zi, J., Zhu, Y. Y., Zhu, S. N., and Ming, N. B. *Nature Materials* **6**(10), 744–748 (2007).

[23] Feng, L., Liu, X. P., Lu, M. H., Chen, Y. B., Chen, Y. F., Mao, Y. W., Zi, J., Zhu, Y. Y., Zhu, S. N., and Ming, N. B. *Physical Review Letters* **96**(1), 014301 (2006).

[24] de Espinosa, F. R. M., Jimenez, E., and Torres, M. *Physical Review Letters* **80**(6), 1208–1211 (1998).

[25] Vasseur, J. O., Deymier, P. A., Chenni, B., Djafari-Rouhani, B., Dobrzynski, L., and Prevost, D. *Physical Review Letters* **86**(14), 3012–3015 (2001).

[26] Sanchis-Alepuz, H., Kosevich, Y. A., and Sanchez-Dehesa, J. *Physical Review Letters* **98**(13), 134301 (2007).

[27] Yang, S. X., Page, J. H., Liu, Z. Y., Cowan, M. L., Chan, C. T., and Sheng, P. *Physical Review Letters* **88**(10), 104301 (2002).

[28] Yang, S. X., Page, J. H., Liu, Z. Y., Cowan, M. L., Chan, C. T., and Sheng, P. *Physical Review Letters* **93**(2), 024301 (2004).

[29] Ke, M. Z., Liu, Z. Y., Qiu, C. Y., Wang, W. G., Shi, J., Wen, W. J., and Sheng, P. *Physical Review B* **72**(6), 064306 (2005).

[30] Sukhovich, A., Jing, L., and Page, J. H. *Physical Review B* **77**(1), 014301 (2008).

[31] Sugawara, Y., Wright, O. B., Matsuda, O., Takigahira, M., Tanaka, Y., Tamura, S., and Gusev, V. E. *Physical Review Letters* **88**(18), 185504 (2002).

[32] Profunser, D. M., Muramoto, E., Matsuda, O., Wright, O. B., and Lang, U. *Physical Review B* **80**(1), 014301 (2009).

[33] Maldovan, M. and Thomas, E. L. *Applied Physics B-Lasers and Optics* **83**(4), 595–600 (2006).

[34] Noda, S., Chutinan, A., and Imada, M. *Nature* **407**(6804), 608–610 (2000).

[35] Maldovan, M. and Thomas, E. L. *Applied Physics Letters* **88**(25), 251907 (2006).

[36] Dainese, P., Russell, P. S. J., Wiederhecker, G. S., Joly, N., Fragnito, H. L., Laude, V., and Khelif, A. *Optics Express* **14**(9), 4141–4150 (2006).

[37] Dainese, P., Russell, P. S. J., Joly, N., Knight, J. C., Wiederhecker, G. S., Fragnito, H. L., Laude, V., and Khelif, A. *Nature Physics* **2**(6), 388–392 (2006).

[38] Birks, T. A., Russell, P. S. J., and Culverhouse, D. O. *Journal of Lightwave Technology* **14**(11), 2519–2529 (1996).

[39] Okawachi, Y., Bigelow, M. S., Sharping, J. E., Zhu, Z. M., Schweinsberg, A., Gauthier, D. J., Boyd, R. W., and Gaeta, A. L. *Physical Review Letters* **94**(15), 153902 (2005).

[40] Cloutier, S. G., Hsu, C. H., Kossyrev, P. A., and Xu, J. *Advanced Materials* **18**(7), 841–844 (2006).

[41] Ahn, K. J., Milde, F., and Knorr, A. *Physical Review Letters* **98**(2), 027401 (2007).

[42] Cheng, W., Wang, J. J., Jonas, U., Fytas, G., and Stefanou, N. *Nature Materials* **5**(10), 830–836 (2006).

[43] Gorishnyy, T., Jang, J. H., Koh, C., and Thomas, E. L. *Applied Physics Letters* **91**(12), 121915 (2007).

[44] Gorishnyy, T., Ullal, C. K., Maldovan, M., Fytas, G., and Thomas, E. L. *Physical Review Letters* **94**(11), 115501 (2005).

[45] Still, T., Cheng, W., Retsch, M., Sainidou, R., Wang, J., Jonas, U., Stefanou, N., and Fytas, G. *Physical Review Letters* **100**(19), 194301 (2008).

[46] Fang, N., Xi, D. J., Xu, J. Y., Ambati, M., Srituravanich, W., Sun, C., and Zhang, X. *Nature Materials* **5**(6), 452–456 (2006).

[47] Ding, Y. Q., Liu, Z. Y., Qiu, C. Y., and Shi, J. *Physical Review Letters* **99**(9), 093904 (2007).

[48] Ambati, M., Fang, N., Sun, C., and Zhang, X. *Physical Review B* **75**(19), 195447 (2007).

[49] Ao, X. Y. and Chan, C. T. *Physical Review E* **77**(2), 025601 (2008).

[50] Chen, H. Y. and Chan, C. T. *Applied Physics Letters* **91**(18), 183518 (2007).

[51] Cummer, S. A., Popa, B. I., Schurig, D., Smith, D. R., Pendry, J., Rahm, M., and Starr, A. *Physical Review Letters* **1**(2), 024301 (2008).

[52] Hepplestone, S. P. and Srivastava, G. P. *Physical Review Letters* **101**(10), 105502 (2008).

[53] Gillet, J. N., Chalopin, Y., and Volz, S. *Journal of Heat Transfer-Transactions of the Asme* **131**(4), 043206 (2009).

[54] Landau, L. D. and Lifshitz, E. M. *Theory of Elasticity*. Butterworth Heinemann, (1986).

[55] Tanaka, Y., Tomoyasu, Y., and Tamura, S. *Physical Review B* **62**(11), 7387–7392 (2000).

[56] Vasseur, J. O., Hladky-Hennion, A. C., Djafari-Rouhani, B., Duval, F., Dubus, B., Pennec, Y., and Deymier, P. A. *Journal of Applied Physics* **101**(11), 114904 (2007).

[57] Pennec, Y., Djafari-Rouhani, B., Larabi, H., Vasseur, J. O., and Hladky-Hennion, A. C. *Physical Review B* **78**(10), 104105 (2008).

[58] Berne, B. J. and Pecora, R. *Dynamic Light Scattering: With Applications to Chemistry, Biolpgy, and Physics*. Dover Publications; Unabridged edition, New York, (1976).

[59] Landau, L. D. and Lifshitz, E. M. *Electrodynamics of Continuous Media, 2nd Edition*. Butterworth-Heinemann, (1984).

[60] Sandercock, J. R. *Tnadem Fabry-Perot Interferometer TFP-1 Operator Manual*. JRS Scientific Instruments, (2001).

[61] Houston, W. V. *Physical Review* **29**(3), 0478–0484 (1927).

[62] Bradley, L. C. and Kuhn, H. *Nature* **162**(4115), 412–413 (1948).

[63] Kuhn, H. *Journal De Physique Et Le Radium* **11**(7), 425–426 (1950).

[64] Hariharan, P. and Sen, D. *Journal of the Optical Society of America* **51**(4), 398–399 (1961).

[65] Lindsay, S. M., Anderson, M. W., and Sandercock, J. R. *Review of Scientific Instruments* **52**(10), 1478–1486 (1981).

[66] Cheng, W., Sainidou, R., Burgardt, P., Stefanou, N., Kiyanova, A., Efremov, M., Fytas, G., and Nealey, P. F. *Macromolecules* **40**(20), 7283–7290 (2007).

[67] Edwards, J. D. and Keller, F. *Transactions of the Electrochemical Society* **79**, 135–144 (1941).

[68] Keller, F., Hunter, M. S., and Robinson, D. L. *Journal of the Electrochemical Society* **100**(9), 411–419 (1953).

[69] Wood, G. C., Osulliva.Jp, and Vaszko, B. *Journal of the Electrochemical Society* **115**(6), 618–620 (1968).

[70] Osulliva.Jp and Wood, G. C. *Proceedings of the Royal Society of London Series a-Mathematical and Physical Sciences* **317**(1531), 511–543 (1970).

[71] Thompson, G. E., Furneaux, R. C., Wood, G. C., Richardson, J. A., and Goode, J. S. *Nature* **272**(5652), 433–435 (1978).

[72] Farnan, I., Dupree, R., Jeong, Y., Thompson, G. E., Wood, G. C., and Forty, A. J. *Thin Solid Films* **173**(2), 209–215 (1989).

[73] Masuda, H. and Fukuda, K. *Science* **268**(5216), 1466–1468 (1995).

[74] Masuda, H., Hasegwa, F., and Ono, S. *Journal of the Electrochemical Society* **144**(5), L127–L130 (1997).

[75] Masuda, H., Yamada, H., Satoh, M., Asoh, H., Nakao, M., and Tamamura, T. *Applied Physics Letters* **71**(19), 2770–2772 (1997).

[76] Asoh, H., Nishio, K., Nakao, M., Tamamura, T., and Masuda, H. *Journal of the Electrochemical Society* **148**(4), B152–B156 (2001).

[77] Martin, C. R. *Science* **266**(5193), 1961–1966 (1994).

[78] Steinhart, M., Wendorff, J. H., Greiner, A., Wehrspohn, R. B., Nielsch, K., Schilling, J., Choi, J., and Gosele, U. *Science* **296**(5575), 1997–1997 (2002).

[79] Zhang, M. F., Dobriyal, P., Chen, J. T., Russell, T. P., Olmo, J., and Merry, A. *Nano Letters* **6**(5), 1075–1079 (2006).

[80] Liang, J. Y., Chik, H., and Xu, J. *Ieee Journal of Selected Topics in Quantum Electronics* **8**(5), 998–1008 (2002).

[81] Matsumoto, F., Nishio, K., Miyasaka, T., and Masuda, H. *Japanese Journal of Applied Physics Part 2-Letters and Express Letters* **43**(5A), L640–L643 (2004).

[82] Matsumoto, F., Kamiyama, M., Nishio, K., and Masuda, H. *Japanese Journal of Applied Physics Part 2-Letters and Express Letters* **44**(8-11), L355–L358 (2005).

[83] Matsumoto, F., Nishio, K., and Masuda, H. *Advanced Materials* **16**(23-24), 2105–2108 (2004).

[84] Masuda, H., Ohya, M., Asoh, H., Nakao, M., Nohtomi, M., and Tamamura, T. *Japanese Journal of Applied Physics Part 2-Letters* **38**(12A), L1403–L1405 (1999).

[85] Masuda, H., Ohya, M., Nishio, K., Asoh, H., Nakao, M., Nohtomi, M., Yokoo, A., and Tamamura, T. *Japanese Journal of Applied Physics Part 2-Letters* **39**(10B), L1039–L1041 (2000).

[86] Masuda, H., Ohya, M., Asoh, H., and Nishio, K. *Japanese Journal of Applied Physics Part 2-Letters* **40**(11B), L1217–L1219 (2001).

[87] Mikulskas, I., Juodkazis, S., Tomasiunas, R., and Dumas, J. G. *Advanced Materials* **13**(20), 1574–1577 (2001).

[88] Choi, J., Luo, Y., Wehrspohn, R. B., Hillebrand, R., Schilling, J., and Gosele, U. *Journal of Applied Physics* **94**(8), 4757–4762 (2003).

[89] Yokoyama, S., Nakahama, T., Mashiko, S., Nakao, M., Yamada, M., Nishio, K., and Masuda, H. *Applied Physics Letters* **87**(19), 191101 (2005).

[90] Masuda, H., Yamada, M., Matsumoto, F., Yokoyama, S., Mashiko, S., Nakao, M., and Nishio, K. *Advanced Materials* **18**(2), 213–216 (2006).

[91] Diggle, J. W., Downie, T. C., and Goulding, C. W. *Chemical Reviews* **69**(3), 365–405 (1969).

[92] Thompson, G. E. and Wood, G. C. *Nature* **290**(5803), 230–232 (1981).

[93] Li, F. Y., Zhang, L., and Metzger, R. M. *Chemistry of Materials* **10**(9), 2470–2480 (1998).

[94] Siejka, J. and Ortega, C. *Journal of the Electrochemical Society* **124**(6), 883–891 (1977).

[95] Parkhutik, V. P. and Shershulsky, V. I. *Journal of Physics D-Applied Physics* **25**(8), 1258–1263 (1992).

[96] Jessensky, O., Muller, F., and Gosele, U. *Applied Physics Letters* **72**(10), 1173–1175 (1998).

[97] Li, A. P., Muller, F., Birner, A., Nielsch, K., and Gosele, U. *Journal of Applied Physics* **84**(11), 6023–6026 (1998).

[98] Skeldon, P., Thompson, G. E., Garcia-Vergara, S. J., Iglesias-Rubianes, L., and Blanco-Pinzon, C. E. *Electrochemical and Solid State Letters* **9**(11), B47–B51 (2006).

[99] Garcia-Vergara, S. J., Skeldon, P., Thompson, G. E., and Habazaki, H. *Electrochimica Acta* **52**(2), 681–687 (2006).

[100] Garcia-Vergara, S. J., Skeldon, P., Thompson, G. E., and Habazaki, H. *Corrosion Science* **49**(10), 3772–3782 (2007).

[101] Houser, J. E. and Hebert, K. R. *Journal of the Electrochemical Society* **153**(12), B566–B573 (2006).

[102] Houser, J. E. and Hebert, K. R. *Nature Materials* **8**(5), 415–420 (2009).

[103] Lide, D. R., editor. *CRC Handbook of Chemistry and Physics, 87th Edition*. TF-CRC, (2006).

[104] Shingubara, S., Murakami, Y., Morimoto, K., and Takahagi, T. *Surface Science* **532**, 317–323 (2003).

[105] Liu, C. Y., Datta, A., and Wang, Y. L. *Applied Physics Letters* **78**(1), 120–122 (2001).

[106] Liu, N. W., Datta, A., Liu, C. Y., and Wang, Y. L. *Applied Physics Letters* **82**(8), 1281–1283 (2003).

[107] Peng, C. Y., Liu, C. Y., Liu, N. W., Wang, H. H., Datta, A., and Wang, Y. L. *Journal of Vacuum Science and Technology B* **23**(2), 559–562 (2005).

[108] Sun, Z. J. and Kim, H. K. *Applied Physics Letters* **81**(18), 3458–3460 (2002).

[109] Asoh, H., Nishio, K., Nakao, M., Yokoo, A., Tamamura, T., and Masuda, H. *Journal of Vacuum Science and Technology B* **19**(2), 569–572 (2001).

[110] Masuda, H., Yotsuya, M., Asano, M., Nishio, K., Nakao, M., Yokoo, A., and Tamamura, T. *Applied Physics Letters* **78**(6), 826–828 (2001).

[111] Asoh, H., Ono, S., Hirose, T., Nakao, M., and Masuda, H. *Electrochimica Acta* **48**(20-22), 3171–3174 (2003).

[112] Masuda, H., Asoh, H., Watanabe, M., Nishio, K., Nakao, M., and Tamamura, T. *Advanced Materials* **13**(3), 189–192 (2001).

[113] Masuda, H., Abe, A., Nakao, M., Yokoo, A., Tamamura, T., and Nishio, K. *Advanced Materials* **15**(2), 161–164 (2003).

[114] Matsumoto, F., Harada, M., Nishio, K., and Masuda, H. *Advanced Materials* **17**(13), 1609–1612 (2005).

[115] Choi, J., Nielsch, K., Reiche, M., Wehrspohn, R. B., and Gosele, U. *Journal of Vacuum Science and Technology B* **21**(2), 763–766 (2003).

[116] Choi, J. S., Wehrspohn, R. B., and Gosele, U. *Advanced Materials* **15**(18), 1531–1534 (2003).

[117] Choi, J., Wehrspohn, R. B., and Gosele, U. *Electrochimica Acta* **50**(13), 2591–2595 (2005).

[118] Lee, W., Ji, R., Ross, C. A., Gosele, U., and Nielsch, K. *Small* **2**(8-9), 978–982 (2006).

[119] Yasui, K., Nishio, K., Nunokawa, H., and Masuda, H. *Journal of Vacuum Science and Technology B* **23**(4), L9–L12 (2005).

[120] Nishio, K., Fukushima, T., and Masuda, H. *Electrochemical and Solid State Letters* **9**(9), B39–B41 (2006).

[121] Gorishnyy, T., Maldovan, M., Ullal, C., and Thomas, E. *Physics World* **18**(12), 24–29 (2005).

[122] Lu, M. H., Liu, X. K., Feng, L., Li, J., Huang, C. P., Chen, Y. F., Zhu, Y. Y., Zhu, S. N., and Ming, N. B. *Physical Review Letters* **99**(17), 174301 (2007).

[123] Kent, A. J., Kini, R. N., Stanton, N. M., Henini, M., Glavin, B. A., Kochelap, V. A., and Linnik, T. L. *Physical Review Letters* **96**(21), 215504 (2006).

[124] Lu, M. H., Zhang, C., Feng, L., Zhao, J., Chen, Y. F., Mao, Y. W., Zi, J., Zhu, Y. Y., Zhu, S. N., and Ming, N. B. *Nature Materials* **6**(10), 744–748 (2007).

[125] Christensen, J., Fernandez-Dominguez, A. I., De Leon-Perez, F., Martin-Moreno, L., and Garcia-Vidal, F. J. *Nature Physics* **3**(12), 851–852 (2007).

[126] Baumgartl, J., Zvyagolskaya, M., and Bechinger, C. *Physical Review Letters* **99**(20), 205503 (2007).

[127] Steinhart, M., Goring, P., Dernaika, H., Prabhukaran, M., Gosele, U., Hempel, E., and Thurn-Albrecht, T. *Physical Review Letters* **97**(2), 027801 (2006).

[128] Wang, L. and Li, B. *Physics World* **21**(3), 27–29 (2008).

[129] Khelif, A., Choujaa, A., Djafari-Rouhani, B., Wilm, M., Ballandras, S., and Laude, V. *Physical Review B* **68**(21), 214301 (2003).

[130] Pennec, Y., Djafari-Rouhani, B., Vasseur, J. O., Khelif, A., and Deymier, P. A. *Physical Review E* **69**(4), 046608 (2004).

[131] Sato, A., Knoll, W., Pennec, Y., Djafari-Rouhani, B., Fytas, G., and Steinhart, M. *Journal of Chemical Physics* **130**(11), 111102 (2009).

[132] Garnett, J. C. M. *Philosophical Transactions of the Royal Society of London Series a-Containing Papers of a Mathematical or Physical Character* **203**, 385–420 (1904).

[133] Huber, K. *Journal of Colloid Science* **3**(3), 197–206 (1948).

[134] Vezenov, D. V., Mayers, B. T., Wolfe, D. B., and Whitesides, G. M. *Applied Physics Letters* **86**(4), 041104 (2005).

[135] Eftekhari, A., editor. *Nanostructured Materials in Electrochemistry*. WILLEY-HVC verlag GmbH and Co. KGaA, Weinheim, (2008).

[136] Evmenenko, G., Dugan, S. W., Kmetko, J., and Dutta, P. *Langmuir* **17**(13), 4021–4024 (2001).

[137] Sun, G. X., Kappl, M., Pakula, T., Kremer, K., and Butt, H. J. *Langmuir* **20**(19), 8030–8034 (2004).

[138] Steinhart, M., Zimmermann, S., Goring, P., Schaper, A. K., Gosele, U., Weder, C., and Wendorff, J. H. *Nano Letters* **5**(3), 429–434 (2005).

[139] Steinhart, M. *Advances in Polymer Science* **220**, 123–187 (2008).

[140] Litvinov, V. M. and Spiess, H. W. *Makromolekulare Chemie-Macromolecular Chemistry and Physics* **192**(12), 3005–3019 (1991).

[141] Cosgrove, T., Turner, M. J., and Thomas, D. R. *Polymer* **38**(15), 3885–3892 (1997).

[142] Kirst, K. U., Kremer, F., and Litvinov, V. M. *Macromolecules* **26**(5), 975–980 (1993).

[143] Tsagaropoulos, G. and Eisenberg, A. *Macromolecules* **28**(18), 6067–6077 (1995).

[144] Arrighi, V., Higgins, J. S., Burgess, A. H., and Floudas, G. *Polymer* **39**(25), 6369–6376 (1998).

[145] Evmenenko, G., Mo, H. D., Kewalramani, S., and Dutta, P. *Polymer* **47**(3), 878–882 (2006).

[146] Horn, R. G. and Israelachvili, J. N. *Macromolecules* **21**(9), 2836–2841 (1988).

[147] Primak, S. V., Jin, T., Dagger, A. C., Finotello, D., and Mann, E. K. *Physical Review E* **65**(3), – (2002).

[148] Jagadeesh, B., Demco, D. E., and Blumich, B. *Chemical Physics Letters* **393**(4-6), 416–420 (2004).

[149] Shih, H. and Flory, P. J. *Macromolecules* **5**(6), 758–761 (1972).

[150] Mai, S. M., Booth, C., and Nace, V. M. *European Polymer Journal* **33**(7), 991–996 (1997).

[151] Mekhilef, N. *Journal of Applied Polymer Science* **80**(2), 230–241 (2001).

[152] Brandrup, J., I. E. H. G. E. A., editor. *Polymer Handbook, 4th Edition*. Wiley-Interscience, (1999).

[153] Hartmann, B. and Jarzynsk.J. *Journal of the Acoustical Society of America* **56**(5), 1469–1477 (1974).

[154] Landau, L. D. and Lifsitz, E. M. *Fluid Mechanics, 2nd Edition*. Butterworth-Heinemann, (1987).

[155] Riese, D. O. and Wegdam, G. H. *Physical Review Letters* **82**(8), 1676–1679 (1999).

[156] Hasegawa, R., Takahash.Y, Tadokoro, H., and Chatani, Y. *Polymer Journal* **3**(5), 600–610 (1972).

[157] Steinhart, M., Senz, S., Wehrspohn, R. B., Gosele, U., and Wendorff, J. H. *Macromolecules* **36**(10), 3646–3651 (2003).

[158] Lovinger, A. J. *Science* **220**(4602), 1115–1121 (1983).

[159] Nyburg, S. C. and Potworow.Ja. *Acta Crystallographica Section B-Structural Science* **B 29**(Feb15), 347–352 (1973).

[160] Craig, S. R., Hastie, G. P., Roberts, K. J., and Sherwood, J. N. *Journal of Materials Chemistry* **4**(6), 977–981 (1994).

[161] Ishikawa, S., Kurosu, H., and Ando, I. *Journal of Molecular Structure* **248**(3-4), 361–372 (1991).

[162] Domanska, U. and Wyrzykowskastankiewicz, D. *Thermochimica Acta* **179**, 265–271 (1991).

[163] Sirota, E. B., King, H. E., Singer, D. M., and Shao, H. H. *Journal of Chemical Physics* **98**(7), 5809–5824 (1993).

[164] Kurosu, H., Takahashi, K., Inoue, D., and Ando, I. *Journal of Molecular Structure* **516**(2-3), 177–184 (2000).

[165] Denicolo, I., Doucet, J., and Craievich, A. F. *Journal of Chemical Physics* **78**(3), 1465–1469 (1983).

[166] Achourboudjema, Z., Bourdet, J. B., Petitjean, D., and Dirand, M. *Journal of Molecular Structure* **354**(3), 197–211 (1995).

[167] Doucet, J., Denicolo, I., Craievich, A., and Collet, A. *Journal of Chemical Physics* **75**(10), 5125–5127 (1981).

[168] Wu, X. Z., Ocko, B. M., Sirota, E. B., Sinha, S. K., Deutsch, M., Cao, B. H., and Kim, M. W. *Science* **261**(5124), 1018–1021 (1993).

[169] Ocko, B. M., Wu, X. Z., Sirota, E. B., Sinha, S. K., Gang, O., and Deutsch, M. *Physical Review E* **55**(3), 3164–3182 (1997).

[170] Merkl, C., Pfohl, T., and Riegler, H. *Physical Review Letters* **79**(23), 4625–4628 (1997).

[171] Huber, P., Soprunyuk, V. P., and Knorr, K. *Physical Review E* **74**(3), 031610 (2006).

[172] Henschel, A., Hofmann, T., Huber, P., and Knorr, K. *Physical Review E* **75**(2), 021607 (2007).

[173] Montenegro, R. and Landfester, K. *Langmuir* **19**(15), 5996–6003 (2003).

[174] Lee, W., Schwirn, K., Steinhart, M., Pippel, E., Scholz, R., and Gosele, U. *Nature Nanotechnology* **3**(4), 234–239 (2008).

[175] Jang, J. H., Koh, C. Y., Bertoldi, K., Boyce, M. C., and Thomas, E. L. *Nano Letters* **9**(5), 2113–2119 (2009).

[176] Terraneo, M., Peyrard, M., and Casati, G. *Physical Review Letters* **88**(9), 094302 (2002).

[177] Li, B. W., Wang, L., and Casati, G. *Physical Review Letters* **93**(18), 184301 (2004).

[178] Segal, D. and Nitzan, A. *Physical Review Letters* **94**(3), 034301 (2005).

[179] Segal, D. *Physical Review Letters* **100**(10), 105901 (2008).

[180] Li, B. W., Wang, L., and Casati, G. *Applied Physics Letters* **88**(14), 143501 (2006).

[181] Segal, D. *Physical Review E* **77**(2), 021103 (2008).

[182] Chang, C. W., Okawa, D., Garcia, H., Majumdar, A., and Zettl, A. *Physical Review Letters* **99**(4), 045901 (2007).

[183] Chang, C. W., Okawa, D., Majumdar, A., and Zettl, A. *Science* **314**(5802), 1121–1124 (2006).

[184] Kumar, B. and Rodrigues, S. J. *Journal of the Electrochemical Society* **148**(12), A1336–a1340 (2001).

[185] Ding, J., Maitra, P., and Wunder, S. L. *Journal of Polymer Science Part B-Polymer Physics* **41**(17), 1978–1993 (2003).

[186] Bishop, C. and Teeters, D. *Electrochimica Acta* **54**(16), 4084–4088 (2009).

[187] Stanton, N. M. and Kent, A. J. *Physical Review B* **73**(22), 220301 (2006).

Acknowledgments

First and foremost, I am grateful to my supervisor, who has supervised me for 5 years since I was assigned to his research group at the Max Planck Institute for Polymer Research as a master's student, for giving me the excellent opportunity, inspiration and freedom to do an intense research. For me, he is an exceptional scientist who has frank personality, enthusiastic attitude toward his research and deep knowledge and insight that are applicable in many areas.

Going back to the history of this research, completing my Ph.D degree was an eye-opening journey of wonder and excitement into new discovery, frustration but most importantly learning a lot about myself and both the scientific world and world in general around me. I have met many people along the way, and they gave me a lot of helpful advice and a great deal of cooperation. I am deeply indebted to each of them.

I would like to express my sincere appreciation to my co-supervisor for his excellent supervision during the last two years. I have greatly benefited from his knowledge and expertise in Brillouin light scattering, phononics and polymer physics. I am most grateful to my collaborators from the Institut d'Electronique de Microélectoronique et de Nanotechnologie, UMR CNRS 8024, Université de Lille 1 in Villeneuve d'Ascq, France, for calculating the theoretical phononic band diagrams and elastic displacement fields. Their careful and professional comments were vital part of this thesis to gain full understanding of elastic wave propagating behaviors observed in nanoporous alumina based hypersonic phononic crystals.

I would like to thank my collaborator from Universität Osnabrück. I have greatly benefited from his knowledge and expertise in anodic aluminium oxide and polymers in general. He provided me with a lot of knowledge about materials property in nanopores of anodic aluminium oxide.

I would like to thank my collaborators at the Max Planck Institute of Microstructure Physics. They gave me precise instruction on the fabrication of anodic porous alumina templates and supported me during my time at Max Planck Institute of Microstructure Physics. They provided me with a very fascinating ferroelectric copolymer sample, P[VDF-TrFE], and told me more about the properties of it. They also provided me with another ferroelectric homopolymer sample, PVDF, and performed differential scanning calorimetry (DSC) and wide angle X-ray scattering (WAXS) measurements of $C_{24}H_{50}$-filled AAO samples.

The samples used in chapter 6 were provided by my collaborators from the Metropolitan University in Tokyo, Japan. I want to express my thanks for them.

I would like to thank a technician for all kinds of computer support. Especially, his competence in programming is amazing. I couldn't have automatized the experimental apparatus for

the preparation of anodic aluminium oxide films without his sophisticated machine language programming. I would like to thank another technician for conducting SEM investigations of anodic aluminium oxide films. He provided not only high quality and beautiful SEM images but also insight into structural analysis. I also enjoyed having a conversation with him about the older generation of Japanese who used to work at the MPI-P.

I acknowledge financial support from Marubun Research Promotion Foundation during the period from April 1st, 2007 to March 31st, 2008.

I thank my office mates for their help with operating Brillouin spectroscopy and related experiment apparatus and for being my work mates in argument. It was nice to go out drinking and have a barbecue party at the Volkspark together. Probably, we were the only ones sharing 60 bottles of water among three people in the MPI-P.

I had the good fortune to meet great friends, who made my life at MPI-P so much enjoyable and unforgettable. I will always remember many happy moments I enjoyed with them. Especially, a trip to Cameroon was an extremely valuable experience. I will also remember the Mensa crews.

Most of all, I am grateful to my family. When I felt running away from difficulties, they always guided and warmly watched over me. Their continuing support and encouragement have been instrumental in the progress I made in my Ph.D work to date. I dedicate this thesis to them.